



**UNIVERSIDADE FEDERAL DO RIO GRANDE DO NORTE  
CENTRO DE CIÊNCIAS EXATAS E DA TERRA**



**PROGRAMA DE PÓS-GRADUAÇÃO EM CIÊNCIA E  
ENGENHARIA DE MATERIAIS**

## **DOCTORAL THESIS**

**Extraction of lithium from beta-spodumene using routes  
with simultaneous acquisition of zeolitic structures**

**Leonardo Leandro dos Santos**

Advisor:

Dr. Eng. Sibebe Berenice Castellã Pergher

Co-advisor:

Dr. Eng. Rubens Maribondo do Nascimento

Thesis No 220 (PPGCEM)

July 2018  
Natal - RN

LEONARDO LEANDRO DOS SANTOS

EXTRACTION OF LITHIUM FROM BETA-SPODUMENE USING ROUTES WITH  
SIMULTANEOUS ACQUISITION OF ZEOLITIC STRUCTURES.

Doctoral thesis presented to the Postgraduate Program in Materials Science and Engineering (*“Programa de Pós-Graduação em Ciência e Engenharia de Materiais”*) of the Federal University of Rio Grande do Norte (*“Universidade Federal do Rio Grande do Norte”*) in partial fulfilling of the requirements for the obtention of the title Ph.D. in Materials Science and Engineering.

Advisor: Sibeles Berenice Castellã Pergher.

Co-advisor: Rubens Maribondo do Nascimento.

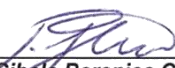
Financial support agency: CAPES - Finance code 001.

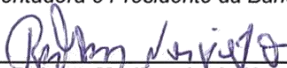
**Natal, RN**

**2018**

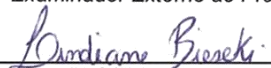
ATA Nº 220/2018 DE REALIZAÇÃO DA DEFESA DE TESE DE DOUTORADO DO ALUNO **LEONARDO LEANDRO DOS SANTOS** DO PROGRAMA DE PÓS-GRADUAÇÃO EM CIÊNCIA E ENGENHARIA DE MATERIAIS DA UNIVERSIDADE FEDERAL DO RIO GRANDE DO NORTE.

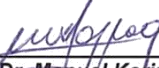
Aos vinte e cinco dias do mês de julho de dois mil e dezoito, às quatorze horas, no auditório do Núcleo de Processamento Primário e Reuso de Água Produzida e Resíduos (NUPPRAR) da Universidade Federal do Rio Grande do Norte (UFRN), realizou-se a Defesa de Tese de Doutorado intitulada “Extraction of lithium from beta-spodumene using routes with simultaneous acquisition of zeolitic structures.”, do Doutorando Leonardo Leandro dos Santos, do Programa de Pós-Graduação em Ciência e Engenharia de Materiais (PPGCEM), tendo como Orientadora a Prof.<sup>a</sup> Dr.<sup>a</sup> Sibebe Berenice Castellã Pergher. A Banca Examinadora foi composta por: Sibebe Berenice Castellã Pergher (Orientadora e Presidente da Banca) - UFRN; Rubens Maribondo do Nascimento (Coorientador) - UFRN; Tiago Pinheiro Braga (Examinador Externo ao Programa) – UFRN; Lindiane Bieseki (Examinadora Externa à Instituição) – UFRN; e Manuel Karim Sapag (Examinador Externo à Instituição) – UNSL/Argentina. Inicialmente, a Orientadora expôs aos presentes o roteiro formal da Defesa de Tese de Doutorado e, em seguida, deu início aos trabalhos da Banca, passando a palavra ao candidato para que desse início a apresentação de seu trabalho, marcando o tempo médio de cinquenta minutos para a devida explanação. Concluída a exposição do candidato, a Presidente passou a palavra aos Examinadores, que deram início ao exame oral. Terminada a arguição oral, solicitou aos presentes e ao Doutorando que se retirassem do recinto para que a Banca proferisse o julgamento. Posteriormente, solicitou o retorno do Candidato e, em seguida, foi comunicado que o aluno Leonardo Leandro dos Santos foi Aprovado na Defesa de Tese de Doutorado de acordo com as normas vigentes na UFRN. A versão final do trabalho deverá ser submetida, via SIGAA, para fins de homologação, no prazo de 30 dias, contendo as modificações sugeridas pela Banca Examinadora. Conforme o artigo 46 da Resolução nº 197/2013 - CONSEPE, o candidato não terá o título se não cumprir as exigências acima. Nada mais tendo sido tratado, a Ata da Sessão Pública de Defesa de Tese de Doutorado foi assinada pelos membros da Banca Examinadora e pelo candidato ao título.

  
 Prof.ª Dr.ª Sibebe Berenice Castellã Pergher  
 Orientadora e Presidente da Banca

  
 Prof. Dr. Rubens Maribondo do Nascimento  
 Coorientador

  
 Prof. Dr. Tiago Pinheiro Braga  
 Examinador Externo ao Programa

  
 Dr.ª Lindiane Bieseki  
 Examinadora Externa à Instituição

  
 Prof. Dr. Manuel Karim Sapag  
 Examinador Externo à Instituição

  
 Leonardo Leandro dos Santos  
 Candidato

Universidade Federal do Rio Grande do Norte - UFRN  
Sistema de Bibliotecas - SISBI  
Catalogação de Publicação na Fonte. UFRN - Biblioteca Central Zila Mamede

Santos, Leonardo Leandro Dos.

Extraction of lithium from beta-spodumene using routes with simultaneous acquisition of zeolitic structures / Leonardo Leandro Dos Santos. - 2018.

162f.: il.

Tese (Doutorado)-Universidade Federal do Rio Grande do Norte, Centro de Ciências Exatas e da Terra, Programa de Pós-Graduação em Ciência e Engenharia de Materiais, Natal, 2018.

Orientador: Dra. Sibeles Berenice Castellã Pergher.

Coorientador: Dr. Rubens Maribondo do Nascimento.

1. Beta-spodumene - Tese. 2. Lithium extraction - Tese. 3. High-throughput screening - Tese. 4.  $\text{Li}_2\text{CO}_3$  - Tese. 5. Zeolites - Tese. I. Pergher, Sibeles Berenice Castellã. II. Nascimento, Rubens Maribondo do. III. Título.

RN/UF/BCZM

CDU 66.017

I dedicate this doctoral thesis to my family,  
and my love, Stephanie.

## ACKNOWLEDGMENTS

*Examine everything carefully; hold fast to that which is good.*

1 Thessalonians 5:21, KJV.

As big a challenge as writing this thesis was to use only one page to thank the people who were part of my trajectory during the Ph.D.

Firstly, I would like to express my sincere gratitude to my Advisor, Dr. Sibebe Berenice Castellã Pergher, for the continuous support of my Ph.D. study and research, for his motivation, enthusiasm, and immense knowledge. His guidance helped me in all the time of research and writing of this thesis. I would like to thank you for encouraging my research and for allowing me to grow as a research scientist. I could not have imagined having a better advisor and mentor for my Ph.D. study.

My sincere thanks also goes to Dr. Rubens Maribondo do Nascimento, for their insightful comments and encouragement, but also for the wisdom and solicitude to assist me in all the steps necessary to the conclusion of this thesis. To Heloise Pastore (IQ/Unicamp), Lindiane Bieseki (IQ/UFRN), Luiz Bertolino (CETEM/UFRJ), Paloma Vinaches (LNLS/CNPEM), and Paulo Sérgio Vieira (UFPB) for your brilliant suggestions to this thesis.

To Dr. Antonio Chica Lara, for his availability, attention and the opportunity to study at ITQ, in Valencia/Spain.

I thank my fellow labmates in Labpemol (Brazil) and ITQ (Spain).

To the company “Companhia Brasileira de Lítio”, on behalf of Eng. Mitsuru Kataoka, for the raw material and information provided.

To CAPES for the financial support for the development of this research.

I extend my thanks to the assistants and employees of UFRN. Thanks to the readiness and teachings.

### **Special appreciation**

My heartfelt thanks could only be given to my family: my parents, who have always prioritized my education. Thank you Mr. Valdeban and Mrs. Marli for, in addition to offering me the opportunity to study, you have always been present and I'm very happy about it; my brother, Wéber, for love and unconditional support. To my fiancée, Stephanie, for the enormous patience, understanding and support at all hours. I am grateful for each loving gesture and every smile.

Finally, I thank my God, my good Father, for letting me through all the difficulties, and for the good health and wellbeing that were necessary to complete this thesis. I have experienced Your guidance day by day. I will keep on trusting You for my future. Thank you, Lord.

## ABSTRACT

SANTOS, L. L. **Extraction of lithium from beta-spodumene using routes with simultaneous acquisition of zeolitic structures.** 2018, July. Thesis - Universidade Federal do Rio Grande do Norte.

The expected increase in demand for lithium salts raises a growing concern regarding this metal scarcity and environmental issues in the national industry of lithium extraction in tilled reserves. The methodologies applied in lithium extraction are associated with the use of sulfates, organic and actinide-based solvents that leads to the formation of sulfated silico-aluminum by-products and radioactive waste. Therefore, this study aimed to develop and to design environmentally efficient routes in order to extract lithium in salt form from beta-spodumene ( $\beta$ -LiAlSi<sub>2</sub>O<sub>6</sub>) and technologically feasible routes to simultaneously obtain zeolites as a by-product. A literature review describes techniques to extract lithium using sulfated additives with by-product recovery after the synthesis process, which indicates that this research is considered unprecedented for having obtained zeolitic crystalline structures formed in the lithium extraction route. In order to elaborate efficient and economically feasible extraction routes, a prior understanding of the attributes of molecular sieves was necessary, in particular, the zeolite types. Thus, the efficiency of lithium extraction using Na<sub>2</sub>CO<sub>3</sub>, NaOH e NaCl additives was evaluated through the measurement of atomic absorption in the supernatant, based on chemoselective ion exchange between Li<sup>+</sup> from  $\beta$ -LiAlSi<sub>2</sub>O<sub>6</sub> and Na<sup>+</sup> from Na<sub>2</sub>CO<sub>3</sub> and NaCl, resulting in up to 85% of extracted lithium. The addition of NaOH promoted the mineralization for the dissolution of  $\beta$ -LiAlSi<sub>2</sub>O<sub>6</sub>, enabling the recovery of Li and the availability of Si and Al for the nucleation and the development of zeolite structures. As a result, two routes were developed operating in the closed and continuous circuit (HTS: high-throughput screening). Each route consisted of different stages such as calcination, hydrothermal treatment, and the use of bicarbonate for the dissolution and precipitation of the associated lithium salt, besides the recovery of new materials like as by-products of cage (LTA and FAU) or channel (LTT, MOR, and MFI) zeolitic topology. At last, in order to validate the strategies used, the materials were categorized applying techniques such as XRD, XRF, TGA, ICP, N<sub>2</sub> adsorption isotherms, SEM, TEM and FT-IR with adsorbed pyridine.

**Keywords:** Beta-spodumene. Lithium extraction. Li<sub>2</sub>CO<sub>3</sub>. High-throughput screening. Zeolites.

## RESUMO

SANTOS, L. L. **Extração de lítio de beta-espodumênio através de rotas para obtenção simultânea de estruturas zeolíticas**. 2018, julho. Tese de Doutorado - Universidade Federal do Rio Grande do Norte.

O aumento previsto na demanda por sais de lítio traz uma crescente preocupação com a escassez desse metal e problemas ambientais na indústria nacional de extração litinífera cujas metodologias empregadas estão associadas a sulfatos, solventes orgânicos e a base de actinídeos, conseqüentemente formando rejeitos silicoaluminosos sulfatados e radioativos. Portanto, o objetivo deste estudo foi desenvolver rota ambientalmente eficiente para extração de lítio na forma de sal a partir de beta-espodumênio ( $\beta$ -LiAlSi<sub>2</sub>O<sub>6</sub>) e tecnologicamente viável para obtenção simultânea de zeólitas como subproduto. Estudos da literatura descrevem metodologias para extração de lítio utilizando aditivos sulfatados, com recuperação do resíduo pós-síntese. O presente estudo, entretanto, é inédito em razão de obter estruturas cristalinas zeolíticas como subproduto em rota para extração de lítio. Em princípio, ao elaborar meios de extração eficiente e economicamente viável, foi importante entender as características das peneiras moleculares, especificamente as zeólitas. Como resultado, a eficiência para extração de lítio com o uso dos aditivos Na<sub>2</sub>CO<sub>3</sub>, NaOH e NaCl foi avaliada por meio de medidas de absorção atômica no sobrenadante, resultando em até 85% de lítio extraído, baseado na troca iônica quimiosseletiva entre Li<sup>+</sup> de  $\beta$ -LiAlSi<sub>2</sub>O<sub>6</sub> e Na<sup>+</sup> de Na<sub>2</sub>CO<sub>3</sub> e NaCl. A adição de NaOH promoveu ação mineralizante com vistas à dissolução de  $\beta$ -LiAlSi<sub>2</sub>O<sub>6</sub>, viabilizando a recuperação de Li e disponibilidade de Si e Al para nucleação e crescimento de estruturas zeolíticas. Como resultado, foram desenvolvidas duas rotas, cada qual operando em circuito cíclico e contínuo (HTS: *High-throughput Screening*), compreendido por etapas como calcinação, tratamento hidrotérmico e bicarbonatação, para extração de lítio e obtenção de subproduto com topologia zeolítica tipo gaiola (LTA e FAU) e tipo canal (LTT, MOR e MFI). Os materiais foram caracterizados por diversas técnicas como DRX, FRX, TG, Espectrometria de emissão atômica por plasma acoplado indutivamente, isoterma de adsorção de N<sub>2</sub>, MEV, MET e Espectroscopia na região do infravermelho por transformada de Fourier com piridina adsorvida.

**Palavras-chave:** Beta-espodumênio. Extração de lítio. Li<sub>2</sub>CO<sub>3</sub>. Triagem de alto rendimento. Zeólitas.

## LIST OF ABBREVIATIONS

AAS	Atomic Absorption Spectrophotometry.
ABNT	In portuguese: “ <i>Associação Brasileira de Normas Técnicas</i> ”.
AES	Atomic Emission Spectrometry.
AFM	Atomic Force Microscope.
AIPO	Aluminophosphate.
ASTM	American Society for Testing and Materials.
BBU	Basic Building Unit.
BET	Brunauer, Emmett and Teller methodology.
BJH	Barrett, Joyner, and Halenda methodology.
CAGR	Composite Annual Growth Rate.
CAN	Cancrinite.
CBL	In portuguese: “ <i>Companhia Brasileira de Lítio</i> ”.
CEC	Cation-exchange Capacity.
D4R	Four-member Double Ring.
D6R	Six-member Double Ring.
DFT	Density Functional Theory.
DSC	Differential Scanning Calorimetry.
DTA	Differential Thermal Analysis.
EDI	Edingtonite.
EDS	Energy-dispersive X-ray Spectrometry.
ERI	Erionite.
FAU	Faujasite.
FCC	Fluid Cracking Catalytic.
FT-IR	Fourier-transform Infrared spectroscopy.
FWHM	Full Width at Half Maximum.
GIS	Gismondine.
GME	Gmelinite.
HC	Hydro-Cracking.
ICP-OES	Inductively Coupled Plasma Optical Emission Spectrometry.
ICSD	Inorganic Crystal Structure Database.
ITQ	In spanish: “ <i>Instituto de Tecnología Química</i> ”.
IUPAC	International Union of Pure and Applied Chemistry.
IZA	International Zeolite Association.
IZA-SC	Structure Commission of the IZA.
LCE	Lithium Carbonate Equivalent.
LPM	In portuguese: “ <i>Laboratório de Peneiras Moleculares</i> ”.
LTA	Linde Type A.

LTT	Linde Type T.
LTX	Linde Type X.
LTY	Linde Type Y.
MCM	Mobil Composition of Matter.
MeAPO	Metal-aluminophosphate.
MEDOX	Medical Oxygen concentrator.
MFI	Mobil-five.
MAR	Mining Annual Report.
MOF	Metal-organic Framework.
MOR	Mordenite.
NMR	Nuclear Magnetic Resonance spectroscopy.
OFF	Offretite.
OSDA	Organic Structure-directing Agent.
PIXE	Proton Induced X-ray Emission.
RCD	Relative Crystallinity Degree.
S6R	Six-membered Single Ring.
SAPO	Silicoaluminophosphate.
SAR	Si/Al Ratio.
S <sub>BET</sub>	BET area.
SBU	Secondary Building Unit.
SEM	Scanning Electron Microscopy.
SIMS	Secondary Ion Mass Spectroscopy.
SOD	Sodalite.
TEAOH	Tetraethylammonium hydroxide.
TEM	Transmission Electron Microscopy.
TEOS	Tetraethylorthosilicate.
TGA	Thermogravimetric Analysis.
TMAOH	Tetramethylammonium hydroxide.
TPA <sup>+</sup>	Tetrapropylammonium cation.
TPD	Temperature Programmed Desorption.
TS	Titanosilicate.
UTD	Dallas University of Texas.
VFI	VPI-five.
VPI	Virginia Polytechnical Institute.
XPS	X-ray Photoelectron Spectroscopy.
XRD	X-ray Diffraction.
XRF	X-ray Fluorescence.
ZK	Mobil Zeolite Kerr.
ZSM-5	Zeolite Socony Mobil-5.

## SUMMARY

### **Chapter 1.**

Introduction ..... 1

### **Chapter 2.**

Objectives ..... 4

### **Chapter 3.**

Literature review..... 5

3.1. Lithium processing ..... 5

3.2. Zeolites and molecular sieves fundamentals ..... 18

3.2.1. Early and industrial history..... 18

3.2.2. Chemical structure and zeolite properties..... 23

3.2.3. Mechanisms of zeolite synthesis ..... 33

3.2.4. Perspectives for zeolite synthesis and catalysis..... 38

3.3. Research justifications ..... 40

### **Chapter 4.**

Calcination-free lithium extraction and simultaneous recovery of LTA-type zeolite.... 58

### **Chapter 5.**

$\text{Li}_2\text{O}:\text{Na}_2\text{CO}_3:\text{NaCl}$  system calcination: kinetic study for conversion to lithium salt .... 81

### **Chapter 6.**

Template-free MFI-type zeolite synthesis in lithium extraction route from beta-spodumene samples ..... 97

### **Chapter 7.**

Channel and cage-type zeolites obtained in lithium extraction route..... 120

### **Chapter 8.**

Final considerations..... 142

Appendix A ..... 144

Appendix B..... 145

## LIST OF FIGURES

### Chapter 3.

Figure 1. Polyhedron representation of the spodumene structure .....	7
Figure 2. Distribution of mining titles (DNPM) for lithium in Brazil.....	8
Figure 3. Overview of Li <sub>2</sub> O reserves in Brazil.....	9
Figure 4. Alkaline process for extraction of lithium (hydroxide).....	10
Figure 5. Acid process for extraction of lithium (carbonate) .....	11
Figure 6. Reactivity of spodumene.....	12
Figure 7. Specifications for pyrometric cone test.....	13
Figure 8. Mechanism of reaction between β-spodumene and Na <sub>2</sub> CO <sub>3</sub> /NaCl.....	15
Figure 9. The solubility of Li <sub>2</sub> CO <sub>3</sub> and NH <sub>4</sub> HCO <sub>3</sub> species in aqueous solution.....	16
Figure 10. Mechanism of formation of the main commercial zeolites.....	24
Figure 11. Classification and analysis of porosity and pore structures .....	26
Figure 12. Mechanisms of induction, nucleation and zeolite growth.....	34

### Chapter 4.

Figure 1. Representation of the (a) 3D framework of LTA-type zeolite; and (b) Six-membered ring (6MR) together with relevant O–O distances obtained after geometry optimization. ....	63
Figure 2. XRD patterns of the solids phases formed by the addition of NaOH .....	64
Figure 3. Solubility kinetics of lithium depending on time, temperature, and Li <sub>2</sub> O:Na <sub>2</sub> CO <sub>3</sub> mass ratio .....	65
Figure 4. XRD patterns of the recovered Li <sub>2</sub> CO <sub>3</sub> .....	66
Figure 5. XRD patterns of products obtained from hydrothermal treatment .....	67
Figure 6. SEM and EDS layered images of samples synthesized .....	69
Figure 7. FT-IR spectra of LTA samples synthesized for different times.....	70
Figure 8. Process diagram for lithium extraction and LTA-type zeolite synthesis.....	71
Figure 9. Na <sup>+</sup> /Al <sup>3+</sup> and H <sup>+</sup> /Al <sup>3+</sup> substitutions showing the positions of cations in a simulated final geometry for Na <sup>+</sup> at Si/Al = 1 .....	74
Figure 10. Simulated geometries with Ca <sup>2+</sup> near of the ring: (a) center-position; (b) edge- position.....	75

## Chapter 5.

Figure 1. Pyrometric cone from glass mold. ....	83
Figure 2. a) SEM and b) XRD of beta-spodumene .....	85
Figure 3. Mixing cones with $\text{Li}_2\text{O}:\text{Na}_2\text{CO}_3$ molar ratio and 5% NaCl.....	86
Figure 4. Cone profiles with 5:1 and 4:1 molar ratios $\text{Li}_2\text{O}:\text{Na}_2\text{CO}_3$ and 5% NaCl .....	86
Figure 5. XRD of the calcined $4\text{Li}_2\text{O}:\text{Na}_2\text{CO}_3$ molar ratio .....	88
Figure 6. Effect of the time and a calcination temperature of the $4\text{Li}_2\text{O}:\text{Na}_2\text{CO}_3$ system for conversion to $\text{Li}_2\text{CO}_3$ .....	88
Figure 7. Micrographs of the calcination product .....	89
Figure 8. Conversion and heating rates at different molar ratios ( $\text{Li}_2\text{O}:\text{Na}_2\text{CO}_3$ ) at 923 K .....	90
Figure 9. Crystallization curves plotted for $\ln(-\ln(1-a))$ vs. $\ln(t)$ .....	92
Figure 10. Correlation between experimental data and the proposed model .....	93
Figure 11. Arrhenius parameters for the decomposition of beta-spodumene by calcination with alkaline salts.....	94

## Chapter 6.

Figure 1. Procedure for extracting lithium from beta-spodumene and formation of template-free MFI-type zeolite .....	100
Figure 2. Ion exchange and thermal decomposition schemes to H-form zeolite .....	100
Figure 3. Morphologies of: a) starting b-spod.; b) dealuminated b-spod .....	102
Figure 4. Influence of 1.2:X $\text{Li}_2\text{O}:\text{Na}_2\text{CO}_3$ mass ratio and percentage of NaCl on the $\text{Li}_2\text{O}$ extraction rate.....	103
Figure 5. XRD patterns of MFI zeolites obtained with different molar ratios: (a) $\text{Na}_2\text{O}/\text{SiO}_2$ ; and (b) $\text{H}_2\text{O}/\text{SiO}_2$ .....	104
Figure 6. Influence of $\text{Na}_2\text{O}/\text{SiO}_2$ and $\text{H}_2\text{O}/\text{SiO}_2$ molar ratios on the crystallinity and percentage of the solid product recovery .....	105
Figure 7. SEM of samples MFI-type zeolites $\text{H}_2\text{O}/\text{SiO}_2$ molar ratio .....	106
Figure 8. Relative crystallinity degree and solid yield of MFI-type zeolite depending on the added amount of $\text{Na}_2\text{O}$ : a) low; b) high .....	107
Figure 9. SEM images of solid products depending on the time of crystallization at 453K to a) low $\text{Na}_2\text{O}$ ; b) high $\text{Na}_2\text{O}$ . .....	108
Figure 10. Crystallization curves (a), and plot of $\ln(-\ln(1-a))$ vs. $\ln(t)$ for the isothermal experiments (b) to MFI zeolite of $\text{Na}_2\text{O}/\text{SiO}_2$ molar ratios .....	110

Figure 11. Arrhenius plots for the calculation of the activation energy (E) for a) nucleation; b) crystal growth process .....	<b>112</b>
Figure 12. N <sub>2</sub> adsorption isotherms of LPM-18 .....	<b>114</b>
Figure 13. TGA/DTG curves of n-butylamine desorption for LPM-18 and ZSM-5....	<b>115</b>

## **Chapter 7.**

Figure 1. Flowchart of the experimental procedures used in the study .....	<b>122</b>
Figure 2. XRD patterns of by-products of the lithium extraction route .....	<b>125</b>
Figure 3. FT-IR spectra of by-products of the lithium extraction route .....	<b>125</b>
Figure 4. SEM images: a) beta-spodumene; b) LPM16-X; c) LPM16-Y; and d) LPM17 .....	<b>127</b>
Figure 5. N <sub>2</sub> adsorption isotherms of the cage and channel-type zeolites .....	<b>128</b>
Figure 6. CH <sub>4</sub> and CO <sub>2</sub> adsorption capacity on the cage and channel-type zeolites at 323 K and 1 bar .....	<b>129</b>
Figure 7. The amount of CH <sub>4</sub> and CO <sub>2</sub> adsorbed on different zeolites as a function of pore size and surface area .....	<b>130</b>
Figure 8. CH <sub>4</sub> and CO <sub>2</sub> adsorption isotherms for cage-type zeolites at 298 K.....	<b>132</b>
Figure 9. CH <sub>4</sub> and CO <sub>2</sub> fractional uptake curves of the cage and channel-type zeolites at 323 K and 1 bar .....	<b>133</b>
Figure 10. The effects of pore volume and surface area on initial adsorption rate (CH <sub>4</sub> and CO <sub>2</sub> ) of the cage and channel-type zeolites .....	<b>134</b>
Figure 11. The effects of pore volume and surface area on equilibrium time (CH <sub>4</sub> and CO <sub>2</sub> ) of the cage and channel-type zeolites .....	<b>135</b>
Figure 12. FT-IR spectra of CH <sub>4</sub> adsorbed on the cage and channel-type zeolites at 293 K and 1 bar.....	<b>136</b>

## LIST OF TABLES

### Chapter 3.

Table 1. Significant lithium minerals. ....	5
Table 2. Lithium production history.....	6
Table 3. Sector overview of the use of the main lithium derivatives.....	10
Table 4. The range of average composition in oxides of spodumene sample.....	13
Table 5. Classification of refractory materials aluminosilicates .....	13
Table 6. A historical perspective of catalysis and molecular sieves .....	20
Table 7. Classification of the main commercial zeolites from SBU's.....	25
Table 8. Properties of zeolites of industrial interest .....	27
Table 9. Characterization techniques for determination of zeolite properties.....	28
Table 10. Comparison between chemisorption and physisorption.....	28
Table 11. Diverse characteristics of the main commercial zeolites .....	30
Table 12. Main factors that influence the synthesis of zeolites.....	33
Table 13. Zeolite growth scheme .....	37

### Chapter 4.

Table 1. Chemical analysis of the beta-spodumene sample (wt%). ....	60
Table 2. The solubility of $\text{Li}_2\text{CO}_3$ in the $\text{NH}_4\text{HCO}_3$ -water system (g/100 g $\text{H}_2\text{O}$ ) .....	66
Table 3. The purity of $\text{Li}_2\text{CO}_3$ .....	66
Table 4. The degree of crystallinity by XRD based on the relative intensity of specific peaks .....	68
Table 5. Different structural groups from FT-IR study of LTA (D6R) zeolites .....	70
Table 6. Synthesis conditions for CEC tests compared with NaP1 and 4A zeolites.....	72
Table 7. Effect of $x/\text{Al}^{3+}$ ( $x = \text{Na}^+$ , $\text{NH}_4^+$ or $\text{Ca}^{2+}$ ) substitutions on zeolite LPM-15 geometry .....	74

### Chapter 5.

Table 1. Mean chemical composition of beta-spodumene samples (wt%). ....	84
Table 2. Dimensional variation data on cones after calcination.....	87
Table 3. Kinetic parameters for the estimated model.....	92

**Chapter 6.**

Table 1. Chemical analysis of the beta-spodumene sample (wt%). .....	<b>99</b>
Table 2. Modified parameters for MFI-type zeolite at different crystallization temperature and Na <sub>2</sub> O/SiO <sub>2</sub> molar rate. Induction period (t <sub>0</sub> ); nucleation rate (V <sub>i</sub> ).....	<b>111</b>
Table 3. Activation energies (E) and pre-exponential factors (A) for nucleation (n) and crystal growth (cg) in MFI-type zeolite crystallization.....	<b>112</b>
Table 4. Physicochemical properties of the synthesized samples of 0.19Na <sub>2</sub> O:0.034Al <sub>2</sub> O <sub>3</sub> :SiO <sub>2</sub> :30H <sub>2</sub> O molar ratio.....	<b>113</b>
Table 5. Acidity properties of n-butylamine desorption in LPM-18.....	<b>116</b>

**Chapter 7.**

Table 1. Chemical analysis of the beta-spodumene sample (wt%). .....	<b>122</b>
Table 2. Different structural groups from FT-IR study of materials.....	<b>126</b>
Table 3. The physical properties of the cage and channel-type zeolites calculated from XRD data and N <sub>2</sub> adsorption data.....	<b>128</b>
Table 4. Initial adsorption rate, equilibrium time and adsorption capacity of CH <sub>4</sub> and CO <sub>2</sub> on the cage and channel-type zeolites.....	<b>134</b>



## Chapter 1. Introduction

---

Lithium is considered a strategic metal, whose use has expanded significantly in recent years. Lithium compounds are used in the preparation of lubricants, in the manufacture of special glasses and alloys, as well as in the pharmaceutical industry, in the production of medicines used in psychiatry. Recently, lithium and its compounds have found use in energy storage devices, by rechargeable lithium-ion batteries <sup>[1, 2]</sup>.

In addition to the gemological interest in spodumene, its lithium content has made it strategically important in view of the strong increase in the consumption of rechargeable batteries over the last decades. Pegmatites account for 26% of the world's known lithium resources, most of it from spodumene <sup>[3]</sup>.

The most common industrial processes used in the extraction of lithium from spodumene are acid and alkaline digestion, as well as the ion exchange method. The acid digestion is carried out with concentrated sulfuric acid at temperatures above 523 K, and the products obtained are lithium carbonate and silicoaluminum residue <sup>[4]</sup>.

Usually, this residue is associated with magnesium, sulfate ions, heavy metals, and lithium remaining in the process, and its complementary extraction is aided by the use of organic and actinide-based solvents <sup>[5]</sup>.

The viability of the extraction process for the production of lithium-based chemical compounds will depend mainly on the percentage of lithium recovered, as well as the possibility of transformation of the residue into a byproduct of commercial interest, such as for zeolites <sup>[6]</sup>. In this context, it is essential to optimize the chemical plant for the extraction of lithium in order to reuse its components.

Zeolites are crystalline aluminosilicates with a periodic arrangement of cages and channels which were found to have extensive industrial use as a catalyst, adsorbent, and ion exchanger. In some cases, it is possible to replace the Si atoms with Al, Ti, B or Ge, among others, obtaining aluminosilicates, titanosilicates, borosilicates or germanosilicates <sup>[7]</sup>.

The potential properties and applications of zeolites depend heavily on their chemical composition and on the size and spatial distribution of their pore and channel systems <sup>[8]</sup>.

In order to develop a lithium extraction route with a byproduct based on zeolites, several synthesis strategies should be considered, including single-step and two-step hydrothermal method, sol-gel techniques, physical and chemical parameters <sup>[9-11]</sup>.

In order to control the synthesis mechanism in obtaining zeolites with specific properties, significant efforts have been devoted to understanding the process of crystallization of zeolites, the influence of numerous variables and their impact on the physicochemical properties of the formed zeolite product. In recent years, several strategies for the synthesis of zeolites have been proposed from solid waste as an alternative source of Si and Al [12-17].

Thus, the optimization of the lithium extraction process to obtain byproduct zeolites should encompass a continuous procedure to guarantee zeolites with high thermal and structural stability, reproducibility, and reliability in catalysis and adsorption activities.

## References

- [1] SWAIN, B.; Recovery and recycling of lithium: A review. **Sep Purif Technol.**, 172 (2017), p. 388-403.
- [2] LAZUEN, J., BAYLIS, R., MERRIMAN, D., & GOTO, M.; **Lithium: Global industry, markets and outlook**, Roskill. 2018.
- [3] GRUBER, P. W., MEDINA, P. A., KEOLEIAN, G. A., KESLER, S. E., EVERSON, M. P., & WALLINGTON, T. J.; Global lithium availability: A constraint for electric vehicles? **J Ind Ecol.**, 15.5 (2011), p. 760-775.
- [4] BRAGA, P. F. A., & FRANÇA, S. C. A.; **Tecnologias para produção de carbonato e hidróxido de lítio a partir de espodumênio e amblygonita**, Rio de Janeiro: CETEM/MCT. 2011.
- [5] MAURICE, A., MACEWAN, J., & OLIVIER, C. A.; **Method of producing lithium carbonate from spodumene**. U.S. Patent No 3,017,243. 1962.
- [6] MESHARAM, P., PANDEY, B. D., & MANKHAND, T. R.; Extraction of lithium from primary and secondary sources by pre-treatment, leaching and separation: A comprehensive review. **Hydrometallurgy**, 150 (2014), p. 192-208.
- [7] BIESEKI, L., SIMANCAS, R., JORDÁ, J. L., BERECIARTUA, P. J., CANTÍN, Á., SIMANCAS, J., PERGHER, S. B. C., VALENCIA, S., REY, F., & CORMA, A.; Synthesis and structure determination via ultra-fast electron diffraction of the new microporous zeolitic germanosilicate ITQ-62. **Chem Commun.**, 54.17 (2018), p. 2122-2125.

- [8] ROUQUEROL, J., ROUQUEROL, F., LLEWELLYN, P., MAURIN, G., & SING, K. S.; **Adsorption by powders and porous solids: principles, methodology and applications**, Massachusetts: Academic press. 2013.
- [9] GOMES, E. S., LUTZWEILER, G., LOSCH, P., SILVA, A. V., BERNARDON, C., PARKHOMENKO, K., PEREIRA, M. M., & LOUIS, B.; Strategy to design zeolite catalysts in the presence of biomass. **Microp Mesop Mat.**, 254 (2017), p. 28-36.
- [10] ELIÁŠOVÁ, P., OPANASENKO, M., WHEATLEY, P. S., SHAMZHY, M., MAZUR, M., NACHTIGALL, P., ROTH, W. J, MORRIS, R. E., & ČEJKA, J.; The ADOR mechanism for the synthesis of new zeolites. **Chem Soc Rev.**, 44.20 (2015), p. 7177-7206.
- [11] ZAAROUR, M., DONG, B., NAYDENOVA, I., RETOUX, R., & MINTOVA, S.; Progress in zeolite synthesis promotes advanced applications. **Microp Mesop Mat.**, 189 (2014), p. 11-21.
- [12] JOHNSON, E. B. G., & ARSHAD, S. E.; Hydrothermally synthesized zeolites based on kaolinite: a review. **Appl Clay Sci.**, 97 (2014), p. 215-221.
- [13] ZOU, J., GUO, C., WEI, C., LI, F., & JIANG, Y.; Synthesis of pure Na-X and Na-P zeolite from acid-extracting residues of CFB fly ash by a single-step hydrothermal method. **Mater Trans.**, 57.5 (2016), p. 726-731.
- [14] VISA, M.; Synthesis and characterization of new zeolite materials obtained from fly ash for heavy metals removal in advanced wastewater treatment. **Powder Technol.**, 294 (2016), p. 338-347.
- [15] HAN, S. W., KIM, J., & RYOO, R.; Dry-gel synthesis of mesoporous MFI zeolite nanosponges using a structure-directing surfactant. **Microp Mesop Mat.**, 240 (2017), p. 123-129.
- [16] OLIVEIRA, M. S. M., NASCIMENTO, R. M., & PERGHER, S. B. C.; **Síntese do material zeolítico LPM-11 de tipologia MOR a partir do resíduo silicoaluminoso gerado na extração do lítio do espodumênio**. BR Patent No 10,2017,016712,7. 2017.
- [17] OLIVEIRA, M. S. M., NASCIMENTO, R. M., & PERGHER, S. B. C.; **Síntese do material zeolítico LPM-12 de tipologia EDI a partir do resíduo silicoaluminoso gerado na extração do lítio do espodumênio**. BR Patente No 10,2017,016757,7. 2017.

## Chapter 2. Objectives

---

The general objective of this doctoral thesis is to elaborate route for the extraction of lithium in the form of lithium carbonate, obtaining byproduct of characteristics and properties of zeolite.

To attain the general objective, several specific objectives were listed:

- Evaluate different extraction routes using  $\text{Na}_2\text{CO}_3$  and  $\text{NaCl}$ ;
- evaluate different extraction routes without the use of organic solvents and structure templates;
- evaluate the recovered lithium content;
- evaluate the main properties of the zeolites obtained.

## Chapter 3. Literature review

In this chapter, the technical and mineralogical aspects of spodumene, its occurrence in pegmatites and the main processing mechanisms used for lithium extraction are presented. A literature survey history of zeolites shows important details for this crystalline aluminosilicate, fundamental in catalytic and adsorption processes.

### 3.1. Lithium processing

Lithium (Li) is the lightest of all metals, with a density only for a half that of water ( $0.534 \text{ g.ml}^{-1}$  at 273 K). It has a low melting point of 453.65 K. Lithium is silvery in appearances, such as for Na and K <sup>[1]</sup>.

Lithium is not found naturally in free form and is distributed in the earth's crust in the order of 0.004%, generally associated with aluminum, potassium, sodium and iron silicates, distributed in more than 130 species of minerals and ores, mainly granitic pegmatites of commercial value associated with the content of  $\text{Li}_2\text{O}$  (theoretical or average on ores), physical characteristics (density measured and Mohs scale hardness), shown in Tab. 1 <sup>[1, 2]</sup>.

Table 1. Significant lithium minerals <sup>[2]</sup>.

Name	Formula	Density ( $\text{g.cm}^{-3}$ )	Mohs	% $\text{Li}_2\text{O}$	
				TMC*	AO**
Amblygonite	$(\text{Li},\text{Na})\text{AlPO}_4(\text{F},\text{OH})$	3.0	5.8	7.4	5.0
Cookeite	$\text{LiAl}_4(\text{AlSi}_3\text{O}_{10})(\text{OH})_8$	2.6-2.7	2.5-3.5	2.9	–
Eucryptite	$\text{LiAlSiO}_4$	2.6	6.5	11.8	4.5-6.5
Lepidolite	$\text{K}(\text{Li},\text{Al})_3(\text{Si},\text{Al})_4\text{O}_{10}(\text{OH},\text{F})_2$	2.7-3.0	2.6	7.7	3.0-4.1
Montebrasite	$\text{LiAl}(\text{PO}_4)(\text{OH},\text{F})$	3.0	5.5-6.0	10.2	7.5-9.5
Petalite	$\text{LiAlSi}_4\text{O}_{10}$	2.0-2.5	6.5	4.5	3.0-4.7
Spodumene	$\text{LiAlSi}_2\text{O}_6$	3.0	7.1	8.0	2.9-7.7
Virgilite	$\text{LiAlSi}_2\text{O}_6$	2.4	5.5-6.0	4.1	–
Zinnwaldite	$\text{KLiFeAl}(\text{AlSi}_3)\text{O}_{10}(\text{OH},\text{F})_2$	2.9-3.1	3.5-4.0	3.4	0.4-0.8

\*TMC: Theoretical maximum content; \*\*AO: Average on ores.

A brief history of lithium production is shown in Tab. 2.

Table 2. Lithium production history <sup>[2]</sup>.

Year	Main events
1790's	José Bonifácio: discovery of the lithium minerals spodumene and petalite; Germany: 1 <sup>st</sup> industrial producer of lithium minerals.
1886	France: production of amblygonite.
1930	Foote Mineral Co.: production of lithium carbonate via alkaline - spodumene process.
1941	Lithium grease has its first major use during World War II.
1946	Lithcoa: development of the acid process for the production of lithium carbonate.
1986	Cyprus Foote/Chemettal (Chile) and FMC/Lithium Division (Argentina): production of lithium from brines; North Carolina (USA): closure of the plants of spodumene due to the high costs of processing, when compared with the brines.
1997	SQM: extraction of LiCl and production of carbonate and hydroxide. Growth in demand (portable, EVs and tools) enables the economic use of lithium minerals;
2005	New projects based on lithium minerals are under development in several countries, aiming to produce battery-grade lithium carbonate (99.95% Li <sub>2</sub> CO <sub>3</sub> ).
2017	Rechargeable batteries represent more than 43% of the worldwide demand for LCE; The share of lithium from mineral sources was 157 kt LCE in the estimated global market of 340 kt LCE (46%).
2018	Nemaska Lithium and Reed Resources Ltd: acid processes for spodumene ore (innovations); Routes for the extraction of lithium (lithium carbonate), with simultaneous formation of zeolitic byproducts <sup>[3,4]</sup> .

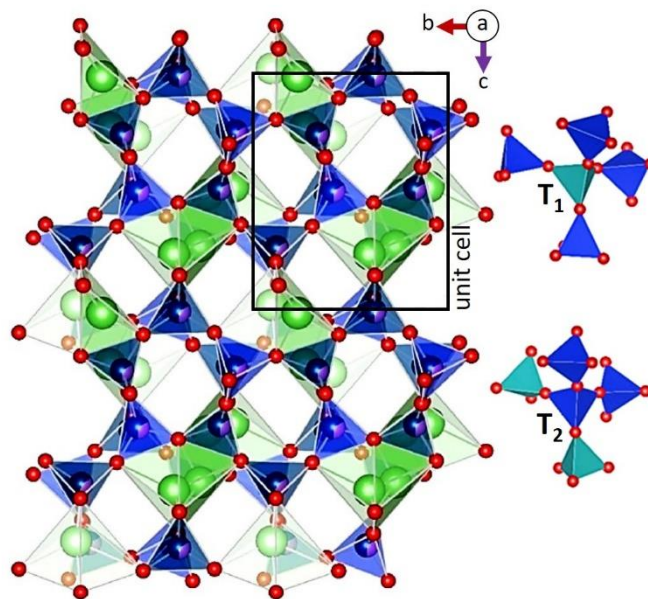
Currently, the main sources of lithium are deposits of brine evaporites, which account for about 66% of global lithium resources, with production concentrated in continental mines of South America (Argentina, Bolivia, and Chile), mainly due to lower costs compared to the extraction in pegmatitic rocks. Although lithium occurs in different minerals, the main sources of commercial exploitation are spodumene, petalite, and lepidolite [5].

Spodumene and petalite occur in granitic pegmatites, in the primary stage, both in Brazil and in other deposits located in Africa and North America. However, as a rule, these two minerals are not associated in nature; the first, denser, arises under higher temperature and pressure conditions [6].

Spodumene is a rare aluminosilicate, of particular importance in several technological applications due to its high thermal and chemical resistivity. Beta-spodumene is the product recrystallized after thermal decomposition of spodumene between 1073-1273 K. Its structure is formed by oxygen ions occupying the vertices of the polyhedra formed by  $\text{Si}^{4+}$  and  $\text{Al}^{3+}$  ( $T_1$ ),  $\text{Li}^+$  surrounded by two surrounding  $\text{AlO}_6$  units, as well as two segments of pyroxene chains enveloping each of the three  $\text{SiO}_4$  ( $T_2$ ) tetrahedra, shown in Fig. 1 [7, 8].

Figure 1. Polyhedron representation of the spodumene structure:

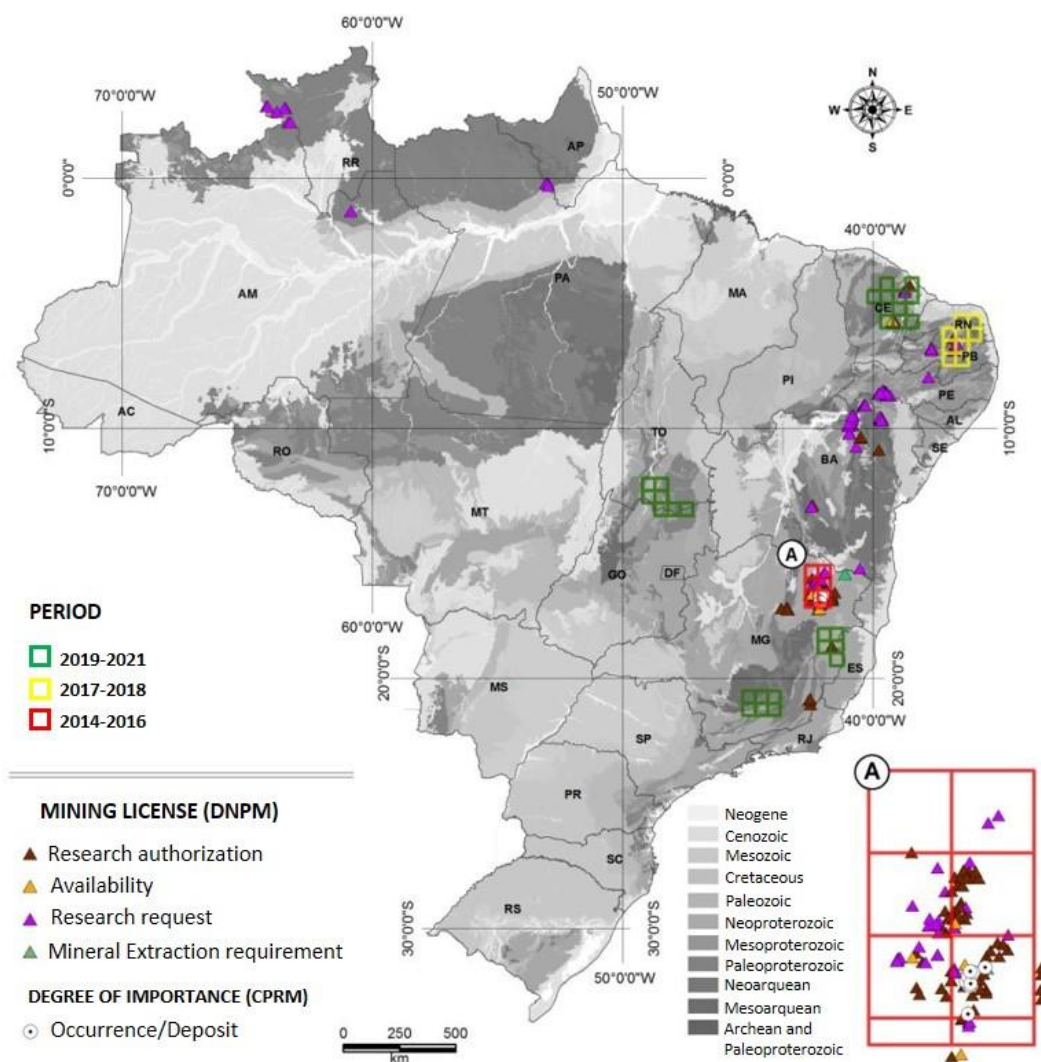
$\text{Al}^{4+}$  and  $\text{Si}^{3+}$  cations (blue),  $\text{Li}^+$  and  $\text{O}^{2-}$  ions (green).



Author (softwares Vesta© and JSmol© [9-11]).

In the national scenario, the main sources of lithium are distributed in the states of Minas Gerais: spodumene concentrate in the pegmatitic province of São João del Rei (AMG mining), and eastern region of the state; Ceará: Solonópole subprovince, large number of occurrences of pegmatites with known lithium minerals; South/southeast of Tocantins: gemological province of São Valério da Natividade (Mata Azul). Rio Grande do Norte and Paraíba: pegmatitic province of Borborema, generally associated with others pegmatites and mafic rocks, shown in Fig. 2 [8, 12].

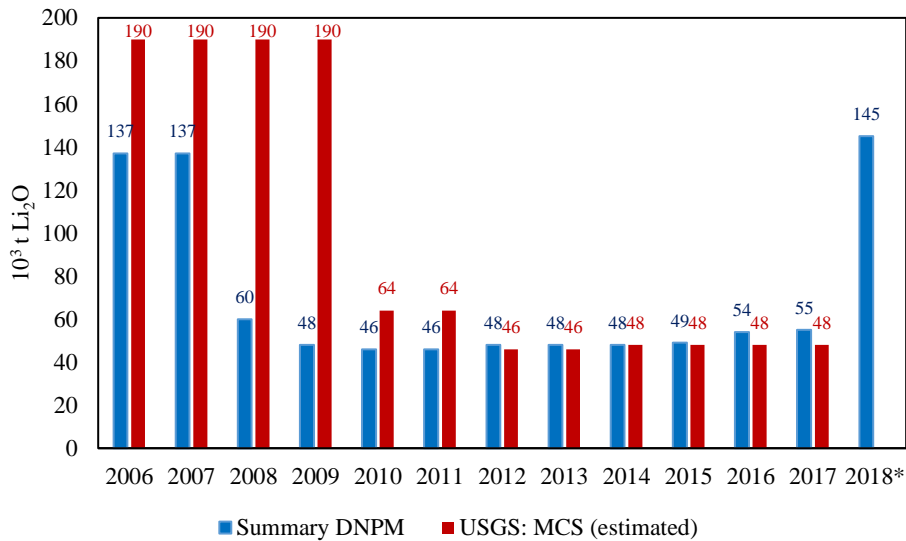
Figure 2. Distribution of mining licenses (DNPM) for lithium in Brazil.



Adapted [8, 12].

In Brazil, there are two major mining companies, Araçuaí Mineração (Sigma Mineração) and Companhia Brasileira de Lítio (CBL). Data from the Departamento Nacional de Produção Mineral (DNPM), show a national reserve capacity of approximately  $50 \times 10^3$  t of  $\text{Li}_2\text{O}$ . For 2018, a substantial increase is expected for  $145 \times 10^3$  t of  $\text{Li}_2\text{O}$  due to the new reserves found, shown in Fig. 3 [12].

Figure 3. Overview of  $\text{Li}_2\text{O}$  reserves in Brazil [12, 13].



\*base-year 2018: position until July/2018, preliminary [12].

The Agência Nacional de Mineração (ANM), created in 2017 linked to the Ministério de Minas e Energia (MME), is responsible for the management of mining activity and Brazilian mineral resources, except hydrocarbons and nuclear substances. The mineral production index, referring to the second half of 2017, shows an increase in the proportion of installed capacity for lithium extraction [12].

This expansion promoted an increase of 8,519 t of concentrated spodumene, as reported by CBL, with an average content of 5.3%  $\text{Li}_2\text{O}$ . In general, 14% of concentrates are available to lubricants and ceramics manufacturers, and 86% are used in the production of chemical compounds: 68% for lithium hydroxide monohydrate and 32% for dry lithium carbonate, among the various derivatives of existing lithium, shown in Tab. 3 [12, 13].

Lithium hydroxide and carbonate are the major forms of compounds in which lithium is used industrially. They are considered mutual derivatives, obtained directly from minerals and brines rich in lithium. The other lithium compounds are generally obtained by reacting them with the acid of the desired salt <sup>[14]</sup>.

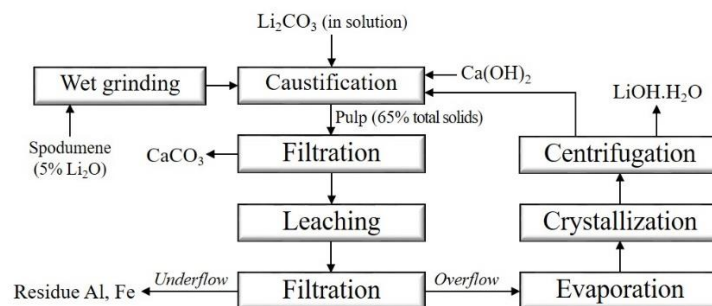
Table 3. Sector overview of the use of the main lithium derivatives <sup>[12, 13]</sup>.

Sector	Derivatives	Main applications
Metallurgical and Nuclear	Metal	Heat conductive metal alloys; electric batteries; a sealant for nuclear reactors.
Ceramic and Pharmaceutical	Oxide and Carbonate	Structural stability during sintering of ceramics; special quality glass (frits); paints and varnishes; medications for treatment of depression and bipolar psychic disorders.
Chemical	Hydroxide	Air purification in confined environments; viscosity oils and greases for $T < 473$ K.
	Hydride	A reducing agent in the synthesis of organic compounds.
	Fluoride	Infrared prisms and spectrophotometers; synthetic enamels.
	Chloride and Bromide	Special lubricants (high temperature).

Carbonate and lithium hydroxide are usually obtained through an acidic and alkaline route, respectively, preceded by a mineral concentration step.

In the alkaline process, the spodumene concentrate is calcined with hydrated lime, and the formed clinker is milled and leached with water to form lithium aluminate and calcium silicate. In the leaching step, excess calcium is hydrolyzed. Later, the lithium aluminate reacts with the calcium hydroxide, forming soluble lithium hydroxide, this associated with a precipitate of calcium aluminate. The lithium hydroxide, upon concentration, is crystallized as lithium monohydrate hydroxide, shown in Fig. 4 <sup>[11]</sup>.

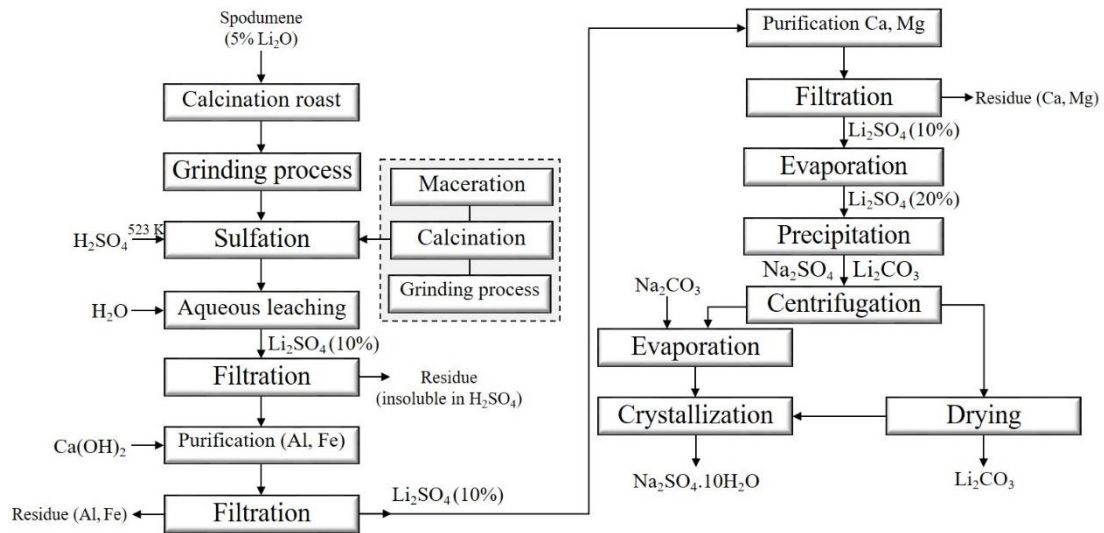
Figure 4. Alkaline process for extraction of lithium (hydroxide).



Adapted <sup>[15]</sup>.

In the acidic route, the spodumene concentrate (calcination roast  $\sim 1323$  K) is sulfated with excess sulfuric acid (98% w/w) at 523 K in specific furnaces. Leached in an aqueous medium, it is finally precipitated as lithium carbonate, after reaction with a solubilizing reducing agent, usually sodium carbonate, shown in Fig. 5 [11].

Figure 5. Acid process for extraction of lithium (carbonate).



Adapted [15].

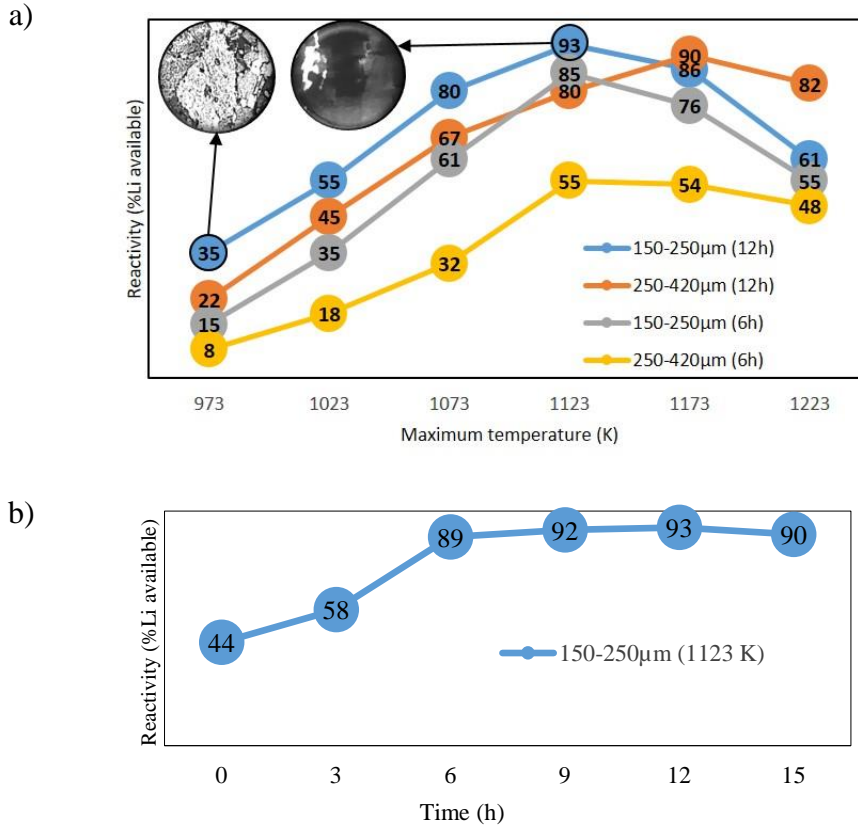
#### a) Heat treatment

The spodumene mineral concentrate requires a specific heat treatment step, preferably in rotating calciner furnaces, for the polymorphic conversion between  $\alpha$ - and  $\beta$ -spodumene, Eq. (A), in order to promote substantial expansion in the structure [2].



This pyrometallurgical phenomenon of irreversible phase transformation justifies the reactivity of spodumene, closely related to temperature and treatment time and, consequently, to the size and the form of agglomeration of the particles of the material, shown in Fig. 6 [16].

Figure 6. Reactivity of spodumene. The increase of a) temperature; and (b) time of calcination roast.



Data provided by CBL.

The period of exposure of the ore to heat favors the reactivity with concentrated sulfuric acid by means of aqueous solubilization by roasting (Fig. 6b). In particular, with increasing temperature ( $> 1143$  K), the probability of partial melting of the material in grain boundaries increases, reducing the percentage of lithium available for the next processing steps (Fig. 6a) <sup>[16]</sup>.

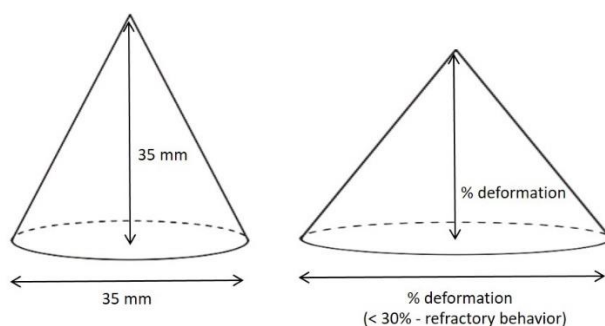
Solubilization reactions, in medium containing lithium aluminosilicates, are mainly bound to silica ( $\text{SiO}_2$ ). Therefore, when the saturation in silica is maintained by quartz, the stability ratios in the morphology of the material will function only of the temperature <sup>[17]</sup>.

The temperature, in this case, becomes a useful parameter in the classification of the material in refractory or similar to the role of fluxes in ceramics, through the formation of porosity as a function of the chemical composition of the material (or glassy phase), when reacting basically with the quartz at low temperatures, retaining the porosity mainly along the contraction cracks <sup>[18]</sup>.

An increase in temperature may cause the formation of a high viscosity liquid, with reduced porosity (similar behavior to the role of fluxes in ceramics), or promote dimensional stability with low permeability (refractory behavior) [18].

The thermal behavior can be predicted by the pyrometric cone test. Samples of aluminosilicates are ground and molded in the form of test cones, shown in Fig. 7, in different composition proportions, arranged under refractory ceramic plates and subjected to the burning process. After cooling, the cones are evaluated for their visual appearance and dimensional variations between test cones and the standard [19, 20].

Figure 7. Specifications for pyrometric cone test.



Adapted [21].

The rate of deformation of the cone will imply the degree of refractoriness, through the thermal conditions used, according to NBR 528/14. In the case of aluminosilicates such as spodumene, this classification falls into the classes of specification SA-5 and SA-4, according to NBR 10237/14, shown in Tab. 4 and Tab. 5 [22].

Table 4. The range of average composition in oxides of spodumene sample (Mina da Cachoeira).

	SiO <sub>2</sub>	Al <sub>2</sub> O <sub>3</sub>	Li <sub>2</sub> O	Na <sub>2</sub> O	Fe <sub>2</sub> O <sub>3</sub>	K <sub>2</sub> O
%	62.9-72.6	18.3-26.5	5.0-8.0	0.1-1.0	0.0-0.7	0.0-0.5

Data provided by CBL.

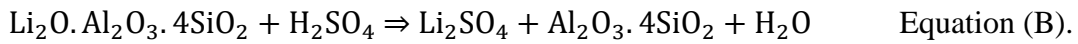
Table 5. Classification of refractory materials aluminosilicates [22].

Classes	SA-5	SA-4	SA-3	SA-2	SA-1
% Al <sub>2</sub> O <sub>3</sub>	18-20.9	21-26.9	27-34.9	35-39.9	40-44.9

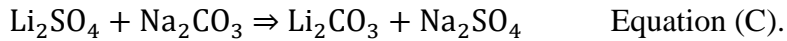
According to NBR 10237/14, aluminosilicates that exceeding 45% of Al<sub>2</sub>O<sub>3</sub> in the calcined base, therefore aluminous, must contain other minerals, rich in free aluminum hydroxide in the form of gibbsite, boehmite or diaspore, which implies a greater refractoriness, with deformation beginning above the Orton cone 15 (1708 K). It is understood as refractory materials that support high temperatures without any pyroplastic deformation <sup>[22, 23]</sup>.

#### b) Hydrothermal treatment

The calcined mixture is treated with sulfuric acid. After aqueous leaching, a solution rich in lithium sulfate is obtained, Eq. (B) <sup>[21]</sup>.



Lithium carbonate is recovered after the addition of sodium carbonate to the solution, accompanied by pH adjustment, precipitation, and drying (acid route), Eq. (C), or liquor concentration and centrifugation (alkaline route), Eq. (D) <sup>[21]</sup>.



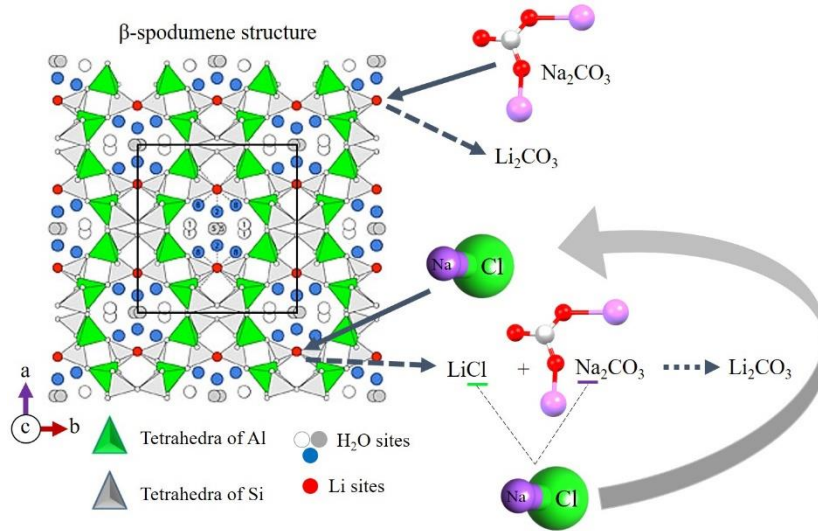
The temperature of the hydrothermal treatment (sulfation and leaching) must be lower than the pre-melting condition of the reactants and products, and higher than the condition that prevents the formation of isometric aluminosilicates of the alkali or alkaline earth metal. For example, in leaching with anhydrous sodium carbonate, the maximum temperature should not exceed the melting temperature of the salt (1124 K) <sup>[24]</sup>.

The major availability (~ 80%) of lithium, within the complex network of atoms that form the β-spodumene structure, interconnects the Si tetrahedra, therefore close to the surface. Easily this lithium is recovered by a chemoselective exchange upon reacting with an alkali metal. However, in all cases, they are salts composed of voluminous molecules with high steric hindrance, which explains their low reactivity <sup>[25]</sup>.

In order to ensure that these reactions occur effectively in order to increase the percentage of lithiferous recovery, promotor substances, typically of lesser spatial geometry, eg NaCl, are added in order to increase the reactivity of the system <sup>[26]</sup>.

These promoters are not consumed or altered by the reaction; therefore, they act in a way to complement the lithium extraction through the exchange reaction. The result is lithium chloride which, after reaction with sodium carbonate, is converted to lithium carbonate, according to the scheme shown in Fig. 8 [27].

Figure 8. Mechanism of reaction between  $\beta$ -spodumene and  $\text{Na}_2\text{CO}_3/\text{NaCl}$ .



Author (softwares JSmol©, Gaussian 03W and GaussView 3.07 [10, 28]).

Although the literature presents data where the use of certain promoters ( $\text{CO}_2$ ,  $\text{CaCl}_2$ ,  $\text{MgCl}_2$ ,  $\text{MgSO}_4$ ) affect the action of the alkali metal carbonate, sulfates and alkali metal chlorides are indicated, due to favoring a higher extraction yield of lithium under conditions relatively mild temperatures. An excess of temperature can lead to side reactions with the formation of lithium compounds difficult to solubilize, except with strong mineral acids [29].

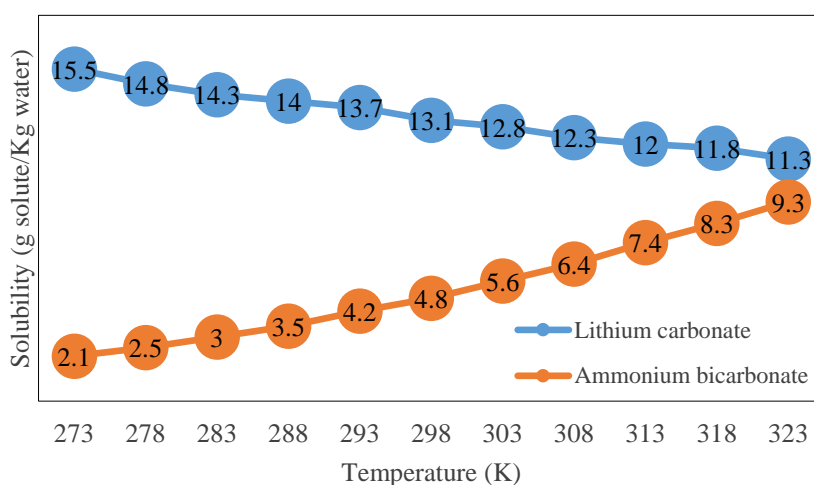
These (unwanted) side reactions are avoided or limited to a comfortable minimum by reducing the system temperature during the hydrothermal treatment; the presence of  $\text{M}_x\text{O} \cdot \text{Al}_2\text{O}_3 \cdot 4\text{SiO}_2$  is an indication that the reaction has reached its maximum of effectiveness [30].

Studies show that ideal lithium-rich fluid formation conditions, easily recoverable after reaction between aluminosilicate and  $\text{M}_x\text{CO}_3$ , are: 773-873 K and 3-5 kbar. According to Averill and Olson (1978), the homogenization temperatures of these fluids occur, preferably, between 823-973 K, with 1.5 kbar for  $\beta$ -spodumene, and between 1123-1173 K, with 4 kbar for  $\alpha$ -spodumene [31-33].

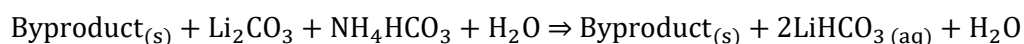
### c) Dissolution and crystallization

The suspension formed in the preceding steps should be treated with agents capable of saturating the resulting mixture in order to complement the solubilization of the lithium complexes present. Usually, ammonia salts, eg  $\text{NH}_4\text{HCO}_3$ , dissolved in a cooled solution of the preceding step, are used under conditions of temperature conducive to solubilization of the lithium salt formed in an aqueous medium, shown in Fig. 9 [34].

Figure 9. The solubility of  $\text{Li}_2\text{CO}_3$  and  $\text{NH}_4\text{HCO}_3$  species in aqueous solution [35].



In the above graph, the temperature range between 298-313 K corresponds to the excellent solubilization of lithium bicarbonate and higher yield of lithium carbonate. By increasing the concentration of  $\text{HCO}_3^-$  species in the solution, the water content can be reduced during the solubilization of the lithium values, Eq. (E) [34].

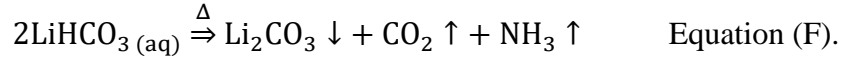


Equation (E).

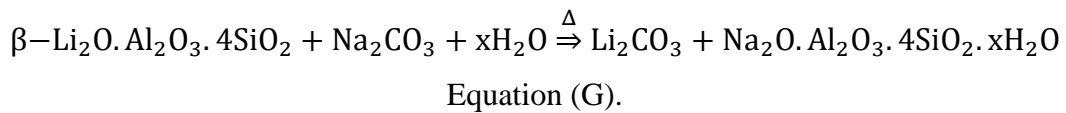
Subsequently, the solids are separated from the solution by filtration (or any other separation medium), stored as: (i) Si/Al molar ratio byproduct equivalent to the starting material, and (ii) lithium-rich solution and alkali metal or alkaline earth metal, heated for precipitation of lithium as the corresponding salt [29].

The precipitation of the dissolved lithium salt is carried out at a temperature close to the boiling temperature of the solution, and preferably under stirring, causing ammonia volatilization (when the bicarbonate agent is ammonia-based) and  $\text{CO}_2$ , complemented

by crystallization of  $\text{Li}_2\text{CO}_3$ , Eq. (F). The resulting slurry is filtered or centrifuged, to recover the corresponding lithium salt. The liquor is partly recirculated, partly for sulfation <sup>[29, 36]</sup>.



The use of autoclaves is also known in processes for the extraction of lithium. Chen et al. (2011b) report a process to treat  $\beta$ -spodumene, after calcination of  $\alpha$ -spodumene, by reacting with sodium carbonate in an autoclave (liquid/solid ratio of 4) and a Na/Li molar ratio of 1.25, at 498 K. After leaching and drying, analyzes of XRD and chemical composition of the solid indicated the presence of lithium carbonate and anisometric silica-alumina structure, Eq. (G) <sup>[31]</sup>.



In general, in processes for the extraction of lithium, the formation of byproducts, usually based on lithium-sodium complex aluminosilicates, is observed, which in turn compromise the extraction yield due to the demand of organic and actinide-based solvents for the addition of lithium, in addition to generating product of leaching poor in lithium, with impurities for difficult separation <sup>[37-39]</sup>.

In the last years, lithium recovery was studied in the extraction process, with the targeting of the residues formed for zeolite synthesis, such as P zeolite (GIS-type), SOD, CAN, MFI, MOR, EDI, LTA, among others, as a consequence of the similarity of chemical composition, mainly related to Si/Al and Na/Al molar ratios <sup>[40, 41]</sup>.

### 3.2. Zeolites and molecular sieves fundamentals

The word zeolite actually originates from a Greek term meaning "to boil" and "stone". This nomenclature clearly entails the property of this material to swell and to lose water when exposed to red heat. After the discovery of the fact that the material responsible for the exchange in soil was zeolites and others, attempts were made to use these natural materials in large scale. But due to certain limitations in using these natural materials attempts were made to synthesize them.

In recent years, versatile approaches have been intensified for the synthesis of zeolites, with the discovery of numerous synthetic microporous materials of great impact in the chemical industry. Some of them have unique pore structures that make them promising for practical use as heterogeneous catalysts <sup>[42]</sup>.

Zeolites are the most widely used catalysts in the world. For this reason, they are probably the group of heterogeneous catalysts better characterized. They have received special attention due to their properties (microporous structure, varied chemical composition and ample load exchange capacity with cation compensation), enabling their use in catalytic processes, such as the conversion of hydrocarbons (alkylation, cracking, hydrocracking, isomerization, hydro-dehydrogenation, selective reforming, dehydration, conversion of methanol to gasoline); inorganic reactions of H<sub>2</sub>S oxidation, oxidation of carbon monoxide, dissociation of water; and in organic chemistry reactions to obtain intermediates and products with high added power <sup>[43, 44]</sup>.

#### 3.2.1. Early and industrial history

Catalyst handling was already an activity known to Arab alchemists, even before Berzelius established the concept and principles of catalysis. Barrer's work in the mid to late 1940's inspired Milton of the Linde Division of Union Carbide Corporation to initiate studies in zeolite synthesis in search of new approaches for separation and purification of air <sup>[45, 46]</sup>.

Since their introduction as a new class of industrial materials in 1954, the annual Market for synthetic zeolites and molecular sieves has grown immensely, to \$1.6-1.7 billion worldwide in 2000's. The major application areas are as adsorbents, catalysts, and ion exchange materials. The largest single market by volume is the detergent application where zeolite A (and recently P-type) functions as an ion exchanger. In the 2000's, 3.9 billion pounds were consumed in that application. Although the second largest volume

use is as catalysts, this is the largest value Market for zeolites, about 55% of the total [47, 48].

Fluid catalytic cracking catalysts, containing primarily silica-enriched forms of zeolite Y, represent more than 95% of total zeolite catalyst consumption, with smaller volumes used in hydrocracking and chemical and petrochemical synthesis. Catalyst consumption in 2000's was estimated at 550 million pounds [48].

Adsorption applications are varied, and include: drying and purification of natural gas, petrochemical streams, e.g., ethylene and propylene, refrigerants, and insulated windows; bulk separations, e.g., xylenes and normal paraffins; and in air separation to produce oxygen by pressure swing adsorption (PSA) or vacuum pressure swing adsorption (VPSA) processes. Adsorbent consumption in 2000's is estimated at 350 million pounds [48].

For 200 years following their discovery by Cronstedt, zeolite minerals (or natural zeolites) were considered to occur typically as minor constituents in vugs or cavities in the basaltic and volcanic rock. Such occurrences precluded their being obtained in mineable quantities for commercial use. From the late 50's to 1962 major geologic discoveries revealed the widespread occurrence of a number of natural zeolites in sedimentary deposits throughout the Western United States [46, 49].

The discoveries resulted from the use of X-ray diffraction to examine very fine-grained (1-5  $\mu\text{m}$ ) sedimentary rock. Some zeolites occur in large near monomineralic deposits suitable for mining. Those that have been commercialized for adsorbent applications include chabazite, erionite, mordenite, and clinoptilolite [46].

The price of zeolites varies considerably depending on the application. The price of catalysts vary from about \$1/pound for FCC to tens of dollars/pound for specialty catalysts; adsorbents from about \$1.50 to \$2/pound, up to tens of dollars/pound for specialty adsorbents; and about \$0.30/pound for detergents. Natural zeolites in bulk applications sell for \$0.02-0.10/pound, and in industrial adsorbent applications for \$1-1.50/pound [48].

A historical perspective of the major events related to catalysis and molecular sieves is shown in Tab. 6. The robustness of the field can be evidenced by the increasing number of annual publications and patents [50].

Table 6. A historical perspective of catalysis and molecular sieves.

Year	Major events
1756	Crönstedt discovered the first zeolite, the stilbite <sup>[51]</sup> .
1777	Fontana described the adsorption phenomenon in charcoal <sup>[52]</sup> .
1836	Berzelius defined <i>catalysis</i> <sup>[53]</sup> .
1840	D'amour studied the reversibility of dehydration of zeolitic crystals <sup>[54]</sup> .
1845	Schafhautle studied the hydrothermal synthesis from silica gel <sup>[55]</sup> .
1858	Eichhorn studied the reversibility of ion exchange in natural zeolites <sup>[56]</sup> .
1862	St. Claire reported the first hydrothermal synthesis of a zeolite, levinite <sup>[57]</sup> .
1895	Ostwald described the kinetic nature of catalysis <sup>[58]</sup> .
1896	Friedel associates the nature of dehydrated zeolitic structures with an open spongy skeleton <sup>[59]</sup> .
1909	Grandjean verified that dehydrated chabazite adsorbs NH <sub>3</sub> , air, and H <sub>2</sub> <sup>[60]</sup> .
1925	Steinhoff and Weigel associated the adsorption property in the chabazite to the definition of <i>molecular sieve</i> <sup>[61]</sup> .
1927	Leonard used X-ray diffraction in the identification of zeolitic minerals <sup>[62]</sup> .
1930	Pauling and Taylor determined the crystallographic structure of the zeolites nantrolite and analcime <sup>[63, 64]</sup> .
1932	McBain conceptualized <i>molecular sieve</i> to define porous solids that act as molecular-scale sieves <sup>[65]</sup> .
40's	Zeolites synthesis of low SAR <sup>[66]</sup> .
1945	Barrer classified zeolites based on molecular size <sup>[67]</sup> .
1948	Milton synthesized zeolites of a structure analogous to mineral mordenite <sup>[68]</sup> .
50's	Milton, Donald et al. synthesized zeolites A, X and Y <sup>[69]</sup> .
1951	Barrer synthesized the analcime, on a large scale <sup>[70]</sup> .
1954	First identification of zeolite X by X-rays <sup>[71]</sup> .
1955	Reed and Breck reported in greater detail the structure of zeolite A <sup>[72]</sup> .
60's	E. Flanigen and D.W. Breck detailed the mechanism of zeolite formation: gel, nucleation, and growth <sup>[70, 72]</sup> ;
	Synthesis of zeolites ZK-5 <sup>[73]</sup> , beta <sup>[74]</sup> , and the ZSM-5 <sup>[75]</sup> , ZSM-11, ZSM-12, ZSM-22, ZSM-23, ZSM-39 and ZSM-48 <sup>[76]</sup> series.
1962	Mobil Oil Corporation has optimized the synthesis of faujasites (X and Y), on a large scale <sup>[77]</sup> . [To be continued...]

---

1968	Weisz developed a commercial process with selectoforming: erionite <sup>[78]</sup> .
1969	Grace described the first chemical modification in the synthesis of ultra-stable Y zeolite <sup>[71, 79]</sup> .
70's	Zeotypes: AIPO <sub>4</sub> , SAPO and MeAPO <sup>[80]</sup> .
1973	Flanigen reported the use of seeds in the crystallization of zeolites <sup>[81]</sup> .
1974	Henkel introduced zeolite A as a substitute for phosphates in detergents <sup>[82]</sup> .
1977	Union Carbide Corporation: 22,000 t of zeolite Y in catalytic cracking in USA <sup>[83]</sup> .
1978	Testing with voluminous templates in the synthesis of commercial zeolites <sup>[84]</sup> .
80's	Secondary synthesis (desalination, isomorphic substitution) <sup>[85]</sup> .
	Wilson synthesized a series of zeotypes from alumino-phosphates, SAPO's and MeAPO's <sup>[86]</sup> ;
1982	Optimization of catalytic cracking from ultra-sensitive Y zeolite: lower coke production and higher gasoline production <sup>[71]</sup> .
	Lok, Cannan, and Messina described the role of organic molecules in the
1983	synthesis of zeolites <sup>[87]</sup> ;
	Enichem synthesized the first redox zeolite: TS-1 (titanosilicate) <sup>[88]</sup> .
1984	Selectivity of form in catalysis: nest effect (confinement) <sup>[89]</sup> .
1985	Mobil process with ZSM-5: conversion of methanol into gasoline <sup>[89]</sup> .
	Jacobs and Martens reported the synthesis of zeolites from high silica
1987	aluminosilicates <sup>[90]</sup> .
1988	VPI-5 synthesis (VFI, 18-R) <sup>[91]</sup> .
	Guth synthesized zeolites in the presence of fluoride ions <sup>[92]</sup> ;
1989	Bell evaluated NMR spectroscopy in the synthesis of zeolites <sup>[93]</sup> .
	Mobil Process with MCM-22 <sup>[88]</sup> ;
90's	Caro used mobilizing agents in the synthesis of zeolites <sup>[94]</sup> ;
	Synthesis of germanosilicate zeolites <sup>[95]</sup> .
1991	Martens performed catalysis in the pore aperture <sup>[96]</sup> .
	Synthesis of mesoporous: MCM-41 <sup>[97]</sup> ;
1992	Jacobs reported the thermodynamic and kinetic effects on the crystallization of zeolites <sup>[98]</sup> .
	Gonthier and Thompson optimize the use of seeds in the synthesis of several
1994	zeolites, on a large scale <sup>[99]</sup> ;
	[To be continued...]

---

---

1994	Kessler, Patarin, and Schott-Darie reported advantages of the fluoride route in the synthesis of microporous materials <sup>[100]</sup> .
1995	Martens optimized the <i>key-lock</i> mechanism <sup>[101]</sup> .
1997	Lewis and Thomas applied computational modeling to describe mechanisms of zeolite synthesis <sup>[102]</sup> ; Morris and Weigel synthesized zeolites from nonaqueous solvents <sup>[103]</sup> ; UTD-1 synthesis (DON, 14-R) <sup>[104]</sup> .
1998	Delamination of nanocrystalline zeolites <sup>[105, 106]</sup> ; Advanced microwave techniques in zeolite synthesis <sup>[107]</sup> ; ITQ-1 synthesis (MWW) <sup>[108]</sup> ; ITQ-2 synthesis (MCM-22/MWW) <sup>[109]</sup> .
1999	Doping of zeolites with boron <sup>[110]</sup> .
2000	Doping of zeolites with gallium <sup>[111]</sup> .
2001	Heterogeneous events in the meso and macroporous catalysis <sup>[112]</sup> .
2003	SDA's: self-structuring of supramolecules with ionic liquids <sup>[113]</sup> ; ITQ-24 synthesis (10,12-R) <sup>[114]</sup> .
2004	UZM-1 synthesis ( $5 < \text{SAR} < 30$ ) <sup>[113]</sup> ; UZM-5 synthesis (UOP, $5 < \text{SAR} < 10$ ) <sup>[115]</sup> ; ITQ-29 synthesis <sup>[116]</sup> .
2005	ITQ-32 synthesis <sup>[117]</sup> .
2006	ITQ-33 synthesis (ITT, 18-R) <sup>[95]</sup> .
2007	Silicon zeolites in the hydrofluoric medium <sup>[113]</sup> .
2008	ITQ-34 synthesis (10-R) <sup>[118]</sup> .
2009	ITQ-37 synthesis (-ITV, 30-R) <sup>[119]</sup> .
2010	ITQ-40 synthesis (-IRY, 16-R) <sup>[120]</sup> ; ITQ-44 synthesis (IRR, 18-R) <sup>[121]</sup> .
2011	ITQ-43 synthesis (28-R) <sup>[122]</sup> .
2012	Organosilanes for silicates/carbon in SDA's <sup>[113]</sup> ; ITQ-50 synthesis (IFY) from pure silica zeolite ITQ-29 (LTA) <sup>[123]</sup> ;
2013	ITQ-51 synthesis (IFO, 16-R) <sup>[124]</sup> ; HPM-1 synthesis <sup>[125]</sup> .
2014	NUD-1 synthesis (18-R) <sup>[126]</sup> ; ITQ-54 synthesis (-IFU, 20-R) <sup>[127]</sup> .

---

[To be continued...]

2015	Extra-large pore zeolites from the C/N ratio <sup>[128]</sup> .
2016	Extra-large porous germanosilicate zeolites <sup>[129]</sup> ; Zeolite MWW: Si/Nb tetrahedrally coordinated as a pillar <sup>[130]</sup> .
2017	Zeolites and zeotypes synthesis from structure-directing agent 2-ethyl-1,3,4-trimethylimidazolium <sup>[131]</sup> . ITQ-55 synthesis <sup>[132]</sup> ;
2018	ITQ-62 synthesis <sup>[133]</sup> ; LPM-15, LPM-16, LPM-17, LPM-18 and LPM-19 synthesis <sup>[3, 4]</sup> .

### 3.2.2. Chemical structure and zeolite properties

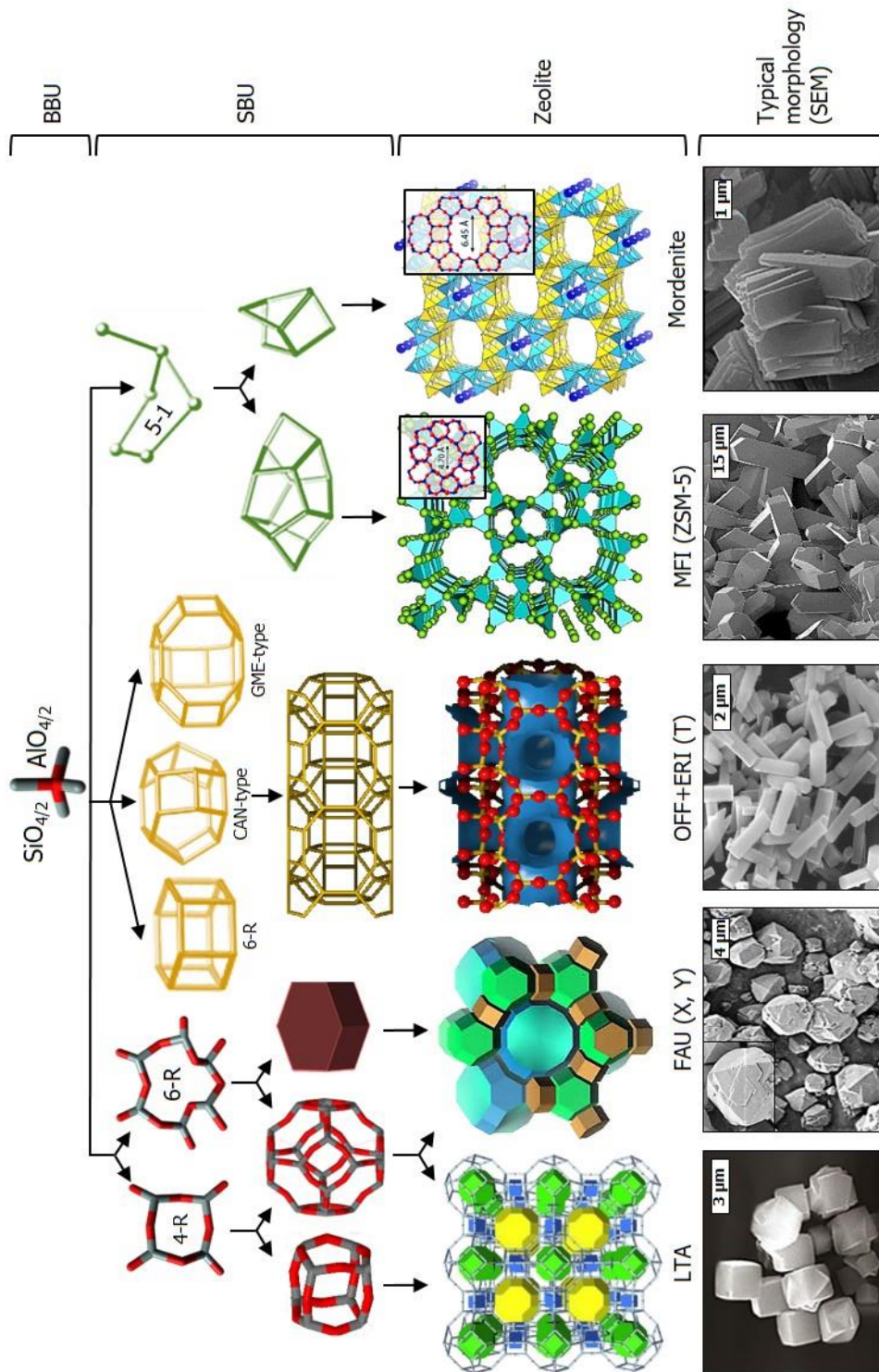
Strictly, zeolites are crystalline aluminosilicates, natural or synthetic, with the inorganic structural arrangement (Si-O-Al) formed by the TO<sub>4</sub> tetrahedra set of vertices occupied by oxygen atoms <sup>[134]</sup>.

Conceptually, they are structures formed by siliceous arrangements, in which Si can be replaced by trivalent elements (T) = Al, Fe, B, Ga, etc., or tetravalent (t) = Ti, Ge, etc. In the substitution between Al<sup>3+</sup> and Si<sup>4+</sup>, the result is a negative overall charge in the arrangement, balanced by the presence of cations located within the pore space, coordinated with oxygen atoms capable of adsorbing atoms and molecules small enough to enter pore openings. Depending on the Si/T molar ratio, these aluminosilicates can be reassembled into zeolites (Si/T < 500) or zeosils (Si/T > 500) <sup>[135]</sup>.

The zeolite structures should not be considered rigid and inert, but rather sensitive, for example, to changes in temperature and pressure; available for modifications without a crystalline collapse by ion exchange, hydrothermal treatment or nitriding; and accessible when in adsorption and catalysis processes <sup>[136]</sup>.

As a rule, zeolitic microstructures can be described through secondary building units (SBUs), which are connected tetrahedra of silicates and aluminates, in combination with basic building units (BBUs). The sodalite cage, or β-cage, for example, is among the main SBUs, because it constitutes the zeolite topologies, LTA and FAU, shown in Fig. 10 and Tab. 7 <sup>[137]</sup>.

Figure 10. Mechanism of formation of the main commercial zeolites.



Author (softwares Gavrog® and Mercury® [138, 139]).

Table 7. Classification of the main commercial zeolites from SBUs <sup>[140]</sup>.

SBU	Zeolite
6 TO <sub>4</sub> single rings (S6R)	Sodalite
4 TO <sub>4</sub> double rings (D4R)	LTA (Na-A)
6 TO <sub>4</sub> double rings (D6R)	FAU (X, Y)
D6R + CAN unit + GME unit	OFF+ERI (T)
Pentasil units (5TO <sub>4</sub> )	MFI (ZSM-5)
Complex 5-1 (T <sub>8</sub> O <sub>16</sub> )	Mordenite

A topological analysis of possible tetrahedra arrangements in the development of zeolite structures suggests a virtually unlimited number even when the structural stability constraint is taken into account. Considering the silicates, more than 150 topologies are reported, with about 950 different zeolites known to date <sup>[141]</sup>.

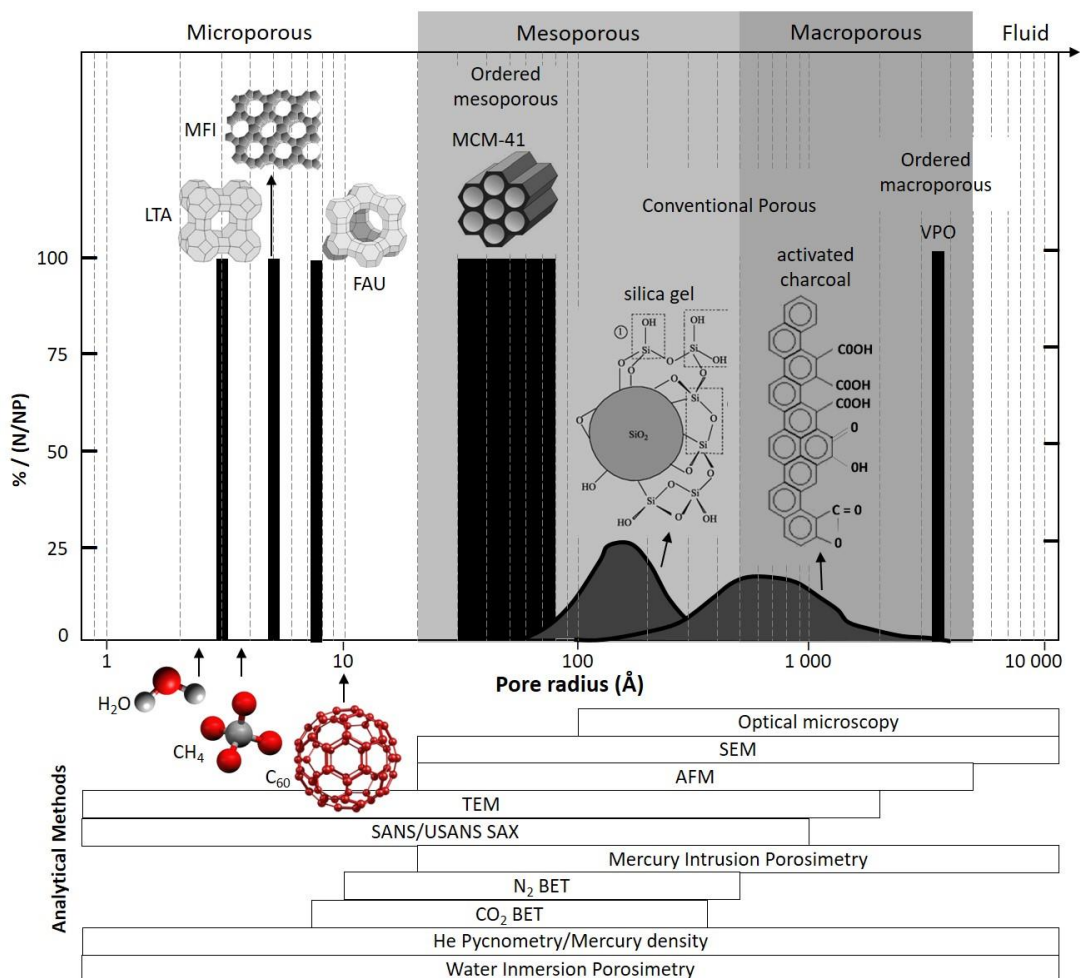
These materials can be described in terms of size, geometry, and connectivity of the porous volume, determined by the structural arrangement. The size of the channels or pore openings controlling the molecular access to the pores is described in terms of the size of the limiting ring in the formation of the cage <sup>[134]</sup>.

Zeolites with channels or flat openings, consisting of 8-membered rings (8MR), have pores with a size of 4 Å, thus classified as microporous; those of medium porosity have flat openings with 10MR of channels with up to 5.5 Å; large pores have apertures or channels of 12MR (7.5 Å). These dimensions are approximate and may vary with the flatness and ellipticity of the rings. Structures with openings limited by 14MR are attributed to extra-large pore solids, shown in Fig. 11 <sup>[142]</sup>.

The pore geometry of some zeolites can be described in terms of channels. For these cases, the connectivity of the porous volume may be one-dimensional, 1D - unconnected channels, 2D - where any point in a plane in the pore system can be accessed from any other point in that plane, or 3D - anywhere in the pore volume is accessible from any other point inside the glass <sup>[134]</sup>.

According to the porous nature of zeolites, these materials have extremely large internal surface areas, in the range of 200-800 m<sup>2</sup>.g<sup>-1</sup>, ideal in catalysis, where the active surface area is very important <sup>[134]</sup>.

Figure 11. Classification and analysis of porosity and pore structures (IUPAC terminology).



Adapted [142, 143].

The factors that influence catalytic activity in zeolites are: their structure (determined by the shape and size of their pores and their high external surface); the type, size and charge of the network cation; the location of the cations in the zeolite and the degree of exchange; SAR, which may affect activity and selectivity; the amount of donor protons present in the structure; the presence of dispersed metallic elements and their activation state [144].

Aluminosilicate zeolites can be easily transformed into acidic catalysts through their ion exchange property. The protons act as Brønsted acids and are the active component of the catalysis, as occurs with faujasite zeolite Y. The charge density can be adjusted to suit the application, varying the SAR [145].

Zeolites exhibit a wide range of physical-chemical behaviors. Some of these structural properties of most zeolites of industrial interest are shown in Tab. 8.

Table 8. Properties of zeolites of industrial interest <sup>[146, 147]</sup>.

Property	Event
↑ Specific area	High degree of hydration, low density and a large volume of voids when dehydrated.
↑ Thermal and hydrothermal stability	Due to the presence of interchangeable cations of the surface that compensate for the negative charges of the structure.
Chemical composition	Si migration results in secondary mesoporosity, improving molecular diffusion and optimum stability to withstand the extreme conditions of catalysis and regeneration in a fluid catalytic cracking.
Acidity	Groups -OH are responsible for the acidity of Brönsted, while the empty orbital of the Al atom is responsible for Lewis acidity.
Basicity	Control over the degree of polymerization of silicates, crystal growth, and a crystalline phase.
Complex networks of channels	Channels of uniform dimensions of the dehydrated crystals, providing different types of shape selectivity.
Shape selectivity	Linear molecules are easily adsorbed.
Catalysis	Related to zeolite surface activity, distribution, and size of internal channels.
Ionic exchange	Related to crystallinity and structure, in terms of the selectivity and extent of ion exchange, as well as the flexibility of the bond between molecular chains.

The catalytic activity of the zeolites occurs within the micropore system, strongly related to pH. The basicity of the zeolites is directly associated with the  $[AlO_4]^-$  and  $[SiO_4]^-$  tetrahedra <sup>[148]</sup>.

The basic sites are associated with the structural oxygen atoms close to the charge-compensating cations. The acid-base properties in zeolites can be classified according to the Lewis model: when the strength of one character increases, the other decreases. Therefore, the lower the acidity of the negative charge compensation cation, the greater the basicity generated by the  $O^{2-}$  anion <sup>[148]</sup>.

When the compensation cation has low electronegativity, the charge density of the oxygen may be large enough to generate basic character properties <sup>[149]</sup>.

In the case of aluminosilicates, the greater the number and concentration of aluminum atoms, the greater the basic strength of the oxygen atoms. The efficiency of this mechanism is associated with the strong electrostatic potentials found inside the channels, reducing the activation energy required for the catalysis phenomenon <sup>[149]</sup>.

Through the parameters of physical-chemical characterization, it becomes possible to identify and define the catalytic properties in the zeolites. To do this, it is necessary to detect specific elements through widely known analytical techniques, shown in Tab. 9.

Table 9. Characterization techniques for determination of zeolite properties <sup>[150]</sup>.

Property	Analysis method
Acidity	FT-IR, Chemical Adsorption: Calorimetry, TPD.
Chemical composition	AAS, XRF, ICP, PIXE.
Network composition	<sup>29</sup> Si and <sup>27</sup> Al NMR, XPS.
Surface composition	XPS, SIMS.
Thermal stability	TGA, DTA.
Structure/Crystal	XRD.
Morphology	SEM, TEM.
Porosity	Physical Adsorption (N <sub>2</sub> , alkanes, ...).

The potential of zeolites as adsorbents in gas separation processes was one of their most easily identified characteristics. The adsorption is a surface phenomenon that occurs through two main mechanisms: chemisorption and physisorption, comparative in some aspects, depending on the interaction and the surface characteristics of the adsorbent, shown in Tab. 10 <sup>[151]</sup>.

Table 10. Comparison between chemisorption and physisorption <sup>[151]</sup>.

Parameter	Chemisorption	Physisorption
Adsorption heat	High	Low
Activation energy	Slow (on)	Fast (not enabled)
Reversibility	Irreversible	Reversible
Temperature	Large temperature range	Low temperatures

The most valuable information in the study of physisorption is the adsorption isotherm, corresponding to the graph of the adsorbed amount (axis of the ordinates) versus pressure (abscissa axis) of the adsorbate, to describe the phenomena that govern the mobility and the affinity of a substance in a porous medium at a certain temperature. An isotherm can be measured experimentally by procedures using volumetric or gravimetric methods [152].

In the literature, several models are mentioned, both to evaluate the adsorption mechanism and the type of isotherm. The isotherms are classified into six different groups. The adsorption kinetics models describe the mechanism that controls the adsorption process [152].

Most of the major adsorbents are essentially low SAR zeolites, synthesized free of organic templates, at comparatively low temperatures and hydrothermal pressures, in short crystallization periods [146].

In turn, higher SAR zeolites (common among industrial catalysts) are synthesized under a wide range of conditions. This is useful for commercial producers who need to manufacture pure products with well-defined specifications, with options for cost control and scale-up, especially in applications involving hydrocarbons and desulphurization [152].

These materials are still used in large quantities and in a variety of commercial processes, in the manufacture of detergents and in the hard water softening [153, 154].

The second largest application is in catalysis, in commercial processes in the petroleum refining industry (FCC and HC). Other applications include adsorbents as well as natural zeolites, soil conditioning, nutrient controlled release agents in fertilizers, odor control agents and selective removal of radioactive isotopes in polluted streams (eg  $^{137}\text{Cs}$  and  $^{90}\text{Sr}$ ) [154].

Approximately 235 different types of structure are currently known. However, only a comparatively small fraction of these is marketed. Even within this commercial subset of zeolites, certain structures, especially zeolites A, X, and Y, tend to dominate in terms of applications in the area of adsorption, shown in Tab. 11 [153, 155].

Table 11. Diverse characteristics of the main commercial zeolites [147, 156].

Zeolite	IZA	Commercial	Cations	Applications (main)	SAR	PS* (Å)
Small pores						
A	LTA	3A	K <sup>+</sup>	EtOH dehydration	2	3-5
		4A	Na <sup>+</sup>	Desiccant agent		
		5A	Ca <sup>2+</sup>	MEDOX		
T	OFF +ERI	KT, NaT	K <sup>+</sup> and Na <sup>+</sup>	Cracking of n-paraffins	5-30	3-5
Intermediate pores						
ZSM-5	MFI	Ammoniacal	NH <sub>4</sub> <sup>+</sup>	Isomerization	25-1000	5-6
		Protonated	H <sup>+</sup>	Catalysis (MTO, MTG, FCC, aromatics, etc.)		
Large pores						
MOR	MOR	Small	Na <sup>+</sup>	Desulfurization	5	6-7
		Big		HC separation	12-200	
X	FAU	13X	Na <sup>+</sup>	Air pre-purification	2-2,5	8
		LiX	Li <sup>+</sup>	O <sub>2</sub> purification (VPSA)		
		AgX	Ag <sup>+</sup>	Catalysis CO/H <sub>2</sub>		
		BaX	Ba <sup>2+</sup> and K <sup>+</sup>	P-xylene recovery		
		CaX	Ca <sup>2+</sup>	H <sub>2</sub> PSA; removal N <sub>2</sub> O		
Y	FAU	NaY	Na <sup>+</sup>	Desulphurisation and	3-5	8
		HY	H <sup>+</sup>	separation HC	20-1000	

\*PS: Pore size.

## a) Zeolite A

The molar composition of the gel for the synthesis of zeolite A presents Na<sub>2</sub>O/Al<sub>2</sub>O<sub>3</sub> molar ratio between 1-3, Na/Si molar ratio of 2, and SAR between 1-2, in addition to a high affinity for cations with high charge density. Distributed between  $\alpha$  and  $\beta$ -cages, these cations influence the size of the pores if they are close to the porous opening [157].

For Na-A, the pore size is about 4 Å (zeolite 4A), whereas, for the potassium form, K-A, the larger cations restrict the pore aperture size to 3 Å (zeolite 3A). If Na<sup>+</sup> is replaced by half the number of Ca<sup>2+</sup> cations, the effective pore size increases to 5 Å (zeolite 5A) [157].

Zeolite A is a typical synthetic zeolite widely used in industry, due to its specific spatial structure useful in gas adsorption and ion exchange in the detergent formulation, as well as acting as a dehydrating agent and separation medium for light paraffin [158].

#### b) Zeolite T

Zeolite T-type is characterized by the infrequency of Offretite (OFF) and Erionite (ERI), normally synthesized in the presence of bulky cations (eg TPA<sup>+</sup>) as structural directing agents. Their effective pore size is equal to that of the erionite pore (3.6 Å and 5.1 Å), due to the stacking faults of the erionite layers in the structure [159].

The zeolite T crystals have a cylindrical structure, stacked in parallel. Of course, the shape and size of its crystals have a strong effect on its performance. The SAR (5-6) makes it resistant to acid and corrosive environments, with potential in catalytic conversion and selective cracking applications. In addition, it constitutes membranes for the dehydration of organic materials, gas selective separation, and mixed matrix membranes [160].

#### c) Zeolite ZSM-5

The empirical formula of ZSM-5 is Na<sub>n</sub>Al<sub>n</sub>Si<sub>96-n</sub>O<sub>192</sub>.16H<sub>2</sub>O. The structural arrangement is formed by the stacking of sheets, members of the silicon-rich pentasil family, characterized by high SAR (15-∞) [161].

The porous structure consists of two interconnected elliptical channel systems: a straight and parallel channel [010], with dimensions 5.1 × 5.7 Å, and another sinusoidal channel in the direction [100], with dimensions 5.4 × 5.6 Å, which intersect perpendicularly. The three-dimensional structure of both channels is accessible through 10MR openings. The substitution of Si<sup>4+</sup> ions by Al<sup>3+</sup> in the structure requires additional protons which, in turn, increase the acidity and, likewise, cause an increase in its activity [162].

The size of the crystals is of the order of 1 to several micrometers, with the versatility of being synthesized as small crystals ( $< 50 \text{ \AA}$ ) or large crystals ( $> 1000 \text{ \AA}$ ), with applications in petrochemical, oil and fine chemical reactions, important in cracking, isomerization, alkylation and aromatization of olefins <sup>[150]</sup>.

#### d) Mordenite zeolite

It is a high silica zeolite. Its network consists of a micropore system with parallel elliptic channels of small and large crystallographic diameters of 5.8 and 6.9  $\text{\AA}$ , respectively. The main channels are interconnected by side channels of 2.9  $\text{\AA}$  in diameter. The most common crystalline structure has SAR = 5 <sup>[163]</sup>.

Numerous forms reported in the literature are derivatives obtained from the sodium form by the ion exchange process. Applied in the separation and adsorption of gas or liquid mixtures, involving acidic or basic components at elevated temperatures, such as for catalyst in numerous industrially important reactions such as hydrocracking, hydroisomerization, and alkylation. In addition, the mordenite is used as a support for semiconductor materials, nonlinear chemical and optical sensors <sup>[164]</sup>.

#### e) Zeolites of FAU topology

Zeolites of the faujasite family are separated into two classes. The zeolites X and Y have identical (isostructural) crystalline structures, but with distinct characteristics, both in chemical composition and in their physical and chemical properties. The greater amount of aluminum in the FAU-X structure confers a greater cation exchange capacity since the greater amount of silicon in the FAU-Y confers greater thermal and hydrothermal stability <sup>[165]</sup>.

The structural similarity between the X and Y zeolites makes it difficult to distinguish them through a simple X-ray diffraction analysis, complemented by other chemical and physical techniques: thermal analysis, chemical analysis, adsorption capacity, specific surface, ion exchange, ionic conductivity, infrared, among others <sup>[165]</sup>.

Normally, the crystalline structure, natural or synthetic, is formed by the union of two types of polyhedra: a hexagonal prism and a truncated octahedron (sodalite cavity). The combination of these two cavities gives rise to the three-dimensional structure <sup>[166]</sup>. The most important applications were shown in Tab. 11 (p. 30).

### 3.2.3. Mechanisms of zeolite synthesis

Several mechanisms have been proposed for the development of zeolites from the very first laboratory design. As a general approximation, they are based on a phase transformation of the amorphous reactants towards a crystalline microporous product, via solution-mediated crystallization or solid transformation <sup>[167]</sup>.

The zeolites are mostly synthesized by the hydrothermal method, influenced by the factors: gel composition (SAR, -OH, inorganic cations); nature of the reagents and pre-treatments; process temperature; duration of reaction; pH of the reaction mixture, shown in Tab. 12 <sup>[168]</sup>.

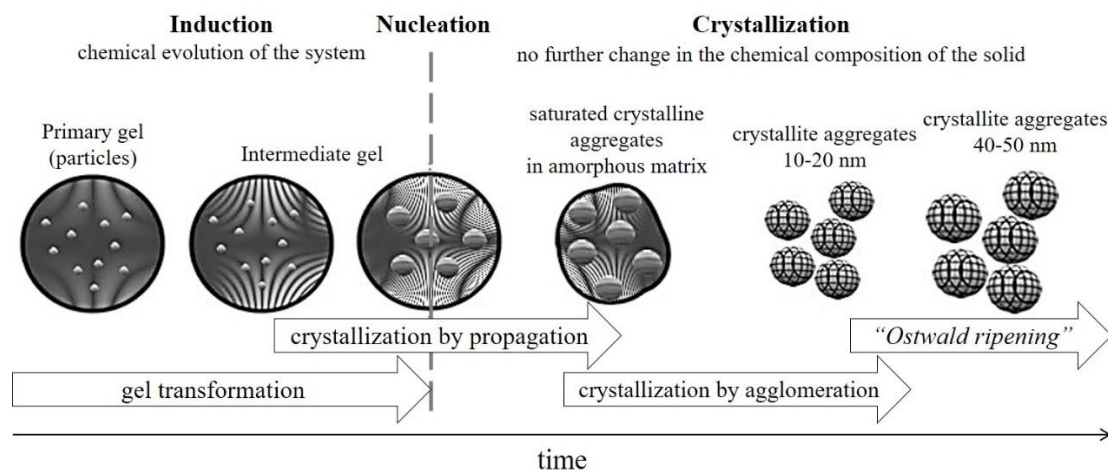
Table 12. Main factors that influence the synthesis of zeolites <sup>[167]</sup>.

Factor	Events
Gel composition	<ul style="list-style-type: none"> <li>○ SAR strongly affects the physical properties of zeolites;</li> <li>○ <math>\uparrow \text{H}_2\text{O}/\text{Na}_2\text{O} \propto \downarrow</math> concentrations of the precursors Si and Al: less stable phases, more open structures;</li> <li>○ <math>\uparrow</math> alkalinity <math>\propto \downarrow</math> induction/nucleation period <math>\propto \uparrow</math> crystallization;</li> <li>○ inorganic cations: structure directing agents, load balancing, crystal purity, product yield;</li> <li>○ monovalent cations: zeolites rich in silicon.</li> </ul>
Nature of reagents	<ul style="list-style-type: none"> <li>○ High reactivity;</li> <li>○ inorganic precursors: hydroxylated surfaces;</li> <li>○ organic precursors: easily incorporate metals into the network.</li> </ul>
Hydrothermal conditions	<ul style="list-style-type: none"> <li>○ <math>\uparrow</math> temperature <math>\propto \uparrow</math> crystallization rate <math>\propto \downarrow</math> nucleation rate: synthesis of denser structures;</li> <li>○ <math>\uparrow \text{H}_2\text{O} \propto \downarrow</math> viscosity.</li> </ul>
Time	Adjusted to minimize unwanted phases.
pH	Usually in alkaline medium (pH > 10).
Others	<ul style="list-style-type: none"> <li>○ The synthesis can be carried out in a continuous or semi-continuous mode, depending on the capacity of industrial application;</li> <li>○ presence of salts (except iron salts);</li> <li>○ agitation rate before and during crystallization.</li> </ul>

In the hydrothermal synthesis, Si and Al sources are combined in an aqueous medium together with cation source to form an amorphous gel. The gel is then subjected to high temperatures (> 333 K) for solubilization of the reactants and subsequent crystallization <sup>[134]</sup>.

In general, low silica zeolites are treated in synthesis reactors at ambient pressure, whereas those of high SAR composition require reactors capable of operating at higher hydrothermal pressures. The mechanism of crystallization occurs in three stages: induction, nucleation and crystal growth, shown in Fig. 12 [169].

Figure 12. Mechanisms of induction, nucleation and zeolite growth.



Adapted [133, 169].

During the induction, equilibrium steps occur for the formation of an amorphous gel from the precursors, i.e., the first cores with ions present in the reaction medium are formed. Next, the gel undergoes a transition from the primary amorphous phase to the intermediate (or secondary) amorphous phase, gradually transformed into the crystalline material along the crystallization mechanism [170].

A nucleation is a discrete event defined as a phase by which the volume transition of a semi-ordered gel is transformed into a structure that is sufficiently ordered to form a growth center from which the crystal lattice will propagate [171].

Finally, crystallization occurs the growth of the zeolitic crystals by transferring material from the liquid phase to the surface of the crystalline structure is formed. The diffusion of the individual species to the surface of the crystal promotes an increase of the dimensions, with the growth rate of the faces determined by the kinetics of the diffusion of the solute and the surface area [171].

Thermodynamic analysis of systems that produce zeolites points to nucleation kinetics as the most critical step in the formation of the synthesis product. Therefore, the domain of zeolite synthesis means the precise control of nucleation in precursors with distinct chemistry under various synthesis conditions [172].

In general, the proposed mechanisms for aggregation of particles leading to the formation of zeolite crystals are: (i) transformation of an amorphous phase into crystalline, (ii) construction of the BBU and SBU blocks to determine the structural characteristics of the final material, (iii) adding templates for growth, and (iv) combining the three main mechanisms [49].

However, the presence of different sources of heteroatoms, inorganic cations, organic cations with different sizes and valence, mineralizing agents, gel concentration, temperature etc., neutralizes the ability to control the synthesis stage on the atomic scale (nucleation) and growth of the crystal [173].

#### a) Zeolite A

In the standard synthesis, 40 mL of solution (0.22 mol/L NaOH) is divided into two equal volumes. To volume V1, 4.13 g sodium aluminate (50-56%  $\text{Al}_2\text{O}_3$ , 40-45%  $\text{Na}_2\text{O}$ ) is added, with stirring maintained for 5 min. To volume V2, 2.23 g of  $\text{SiO}_2$  (silica aerosil) + 2.92 g of NaOH (97%) + 3.29 g of  $\text{H}_2\text{O}$  are added. This solution is stirred for 10 min [178].

Subsequently, solution V1 is poured rapidly into solution V2, and the mixture is under mechanical stirring for 30 min. Subsequently, the gel is transferred to autoclaves at 373 K for 4 h. The product obtained is washed with distilled  $\text{H}_2\text{O}$  to pH 9 and heated in an oven at 363 K overnight [178].

#### b) Zeolite T (ERI+OFF)

The usual method of preparing zeolites of the OFF-type and ERI-type is hydrothermal crystallization by conventional heating. The synthesis gel has a molar chemical composition of  $50\text{SiO}_2:2\text{Al}_2\text{O}_3:13\text{Na}_2\text{O}:4.5\text{K}_2\text{O}:700\text{H}_2\text{O}$ , of whitish appearance after 30 min stirring in the presence of the TMAOH and TEAOH templates [179].

The obtained gel is aged with vigorous stirring at room temperature for 12 h, and crystallization should occur among the techniques: conventional reflux heating; conventional hydrothermal heating; microwave reflux heating; or hydrothermal heating by microwave. Zeolite T of the intergrowth type can be prepared in template-free medium,  $15 < \text{SAR} < 29$  <sup>[180]</sup>.

#### c) Zeolite ZSM-5

The standard synthesis for ZSM-5 zeolite is based on aqueous gels containing structural elements, mineralizing agent, directing agent and, in some cases, co-precipitating agent. These templates perform two functions in the synthesis: to define the specific topology (by which the charge density, shape and volume of the molecule are determinants), and to moderate the pH of the synthesis gel <sup>[181]</sup>.

In the synthesis of MFI topology zeolites (ZSM-5 structure), the synthesis gel can be obtained from the dissolution of NaOH in deionized water, with the addition of  $\text{Al}(\text{NO}_3)_3 \cdot 9\text{H}_2\text{O}$ , in addition to network template TPABr, and TEOS as a source of silicon. The aging lasts for 48 h at room temperature and stirring vigorously, followed by hydrothermal treatment between 443-463 K, up to 72 h, under stirring and heating at 353 K in the nucleation stage for higher percent crystallinity <sup>[181]</sup>.

#### d) Mordenite zeolite

Although the presence of an organic template (eg  $\text{TPA}^+$ ) is excellent, it can cause many problems, such as toxicity and high production cost. A template-free mordenite can be synthesized from a solution formed by dissolving 7.98 g of NaOH and 12.5 g of aluminum nitrate in 70 g of deionized water with the slow addition to the mixture of 50 g of colloidal silica under low stirring speed <sup>[164]</sup>.

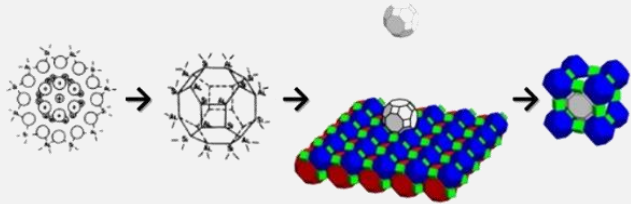
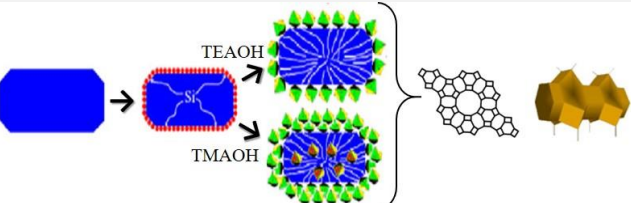
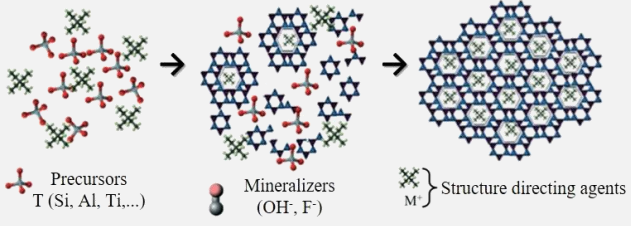
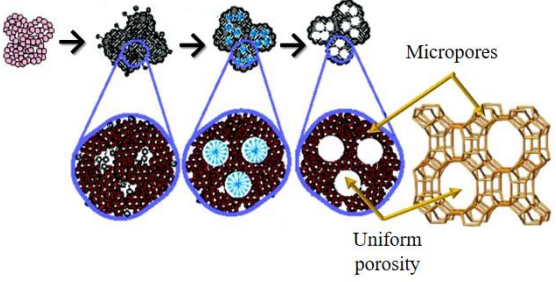
The molar composition of the resulting synthetic gel will naturally be  $6\text{Na}_2\text{O}:50\text{SiO}_2:\text{Al}_2\text{O}_3:250\text{H}_2\text{O}$ . Prior to autoclaving, the above synthetic solution should be aged between 18-24 h at room temperature and then hydrothermally treated for 5 days in an oven at 453 K. After the hydrothermal treatment, the product is recovered, washed thoroughly with deionized water and heat treated at 393 K <sup>[164]</sup>.

e) Faujasite topology zeolites

The synthesis of FAU topology zeolites (LTX) usually involves the hydrothermal reaction of solution formed by sodium hydroxide, alumina and silicon source, with aging of the gel at room temperature for 30 min, with the possibility of zeolite nanocrystals from adjustments in the time/temperature parameters of induction, in addition to a significant reduction of the presence of zeolite P, GIS-type. Crystallization occurs in static, in the range of 2-40 days, from 358 K, with the recovery of the product at  $\text{pH} < 10$  after overnight drying at 343 K <sup>[182]</sup>.

Tab. 13 presents the main mechanisms for the synthesis of commercial zeolites of greater use.

Table 13. Zeolite growth scheme.

Topology	System	Scheme	Ref.
LTA, FAU	Na-A, Na-X		[174]
OFF+ERI	Na-T		[175]
MFI	Na-ZSM-5		[176]
Mordenite	Na-MOR		[177]

Author (softwares Gavrog® e Mercury® <sup>[136]</sup>).

### 3.2.4. Perspectives for zeolite synthesis and catalysis

More specifically in the current decade, we see an expanding scientific base in the field of catalysis, mainly aimed at obtaining zeolites through modifications in the synthesis mechanisms, instead of concentrating only on the search for new structures. The number of modified methods continues to grow, providing the catalytic community with new tools to adjust the equilibrium and rate properties, enabling high-performance compositions to be obtained <sup>[154, 183-185]</sup>.

It is also important to consider the feasibility of several characterization techniques that accompany such an advance, exemplified by the analysis of zeolites at the atomic level or an individual molecule, as well as in vibrational spectroscopy, a characterization technique among the most used for the investigation of porous functional materials <sup>[186, 187]</sup>.

By moving the zeolites for practical use as catalysts, it is necessary to devise easy or alternative methods that assist in this task. Theoretical chemistry, for example, clearly modified the way science and technology of zeolites were approached in the present study. Computational methods can now be routinely used to model and, with increasing success, predict the reactivity as well as the molecular properties of sorption and diffusion of a wide variety of zeolite structures <sup>[188]</sup>.

The accessibility of these materials is of paramount importance for their application in catalysis. Consequently, the industry has directed its attention to the understanding and adaptation of processes that allow the development of materials with micro, meso and macroporosity, as well as hierarchical zeolites, from optimizations in the industrial processing mechanisms. However, to ensure commercial success, cost and manufacturing restrictions must be recognized and respected during processing <sup>[189]</sup>.

In general, as already mentioned, the zeolites are synthesized under hydrothermal conditions from amorphous aluminosilicate gel. Almost always, the formation of a zeolitic phase may be preceded by a different phase during the course of crystallization. This phenomenon may be an alternative synthesis strategy to obtain zeolites during an industrial processing activity (ceramics, mineral extraction, among others). In this case, the idea is to reverse the formation of residues in byproducts of commercial interest, for example, zeolites.

An important advantage as a heterogeneous catalyst is in the generation of active centers in its interior, in addition to the selectivity due to the strength of the centers, there is a selectivity of form. Thus, the size and shape of the reactants, the reaction intermediates, and the products correspond to the structure and dimensions of the zeolitic pore <sup>[144]</sup>.

Considering this line of research, the use of zeolites as a support for Ni in the preparation of heterogeneous catalysts for selective CO<sub>2</sub> hydrogenation may be a very interesting option. In particular, it is found that carriers with high specific areas, such as zeolites, can enhance the catalytic activity of a catalyst by an improvement in the dispersion of the active centers. In addition, the topology and crystalline structure of these materials appear to affect the interactions of the metal carrier particles, improving their stability against sintering <sup>[190, 191]</sup>.

### 3.3. Research justifications

Industrial processing activities for the extraction of lithium, with obtaining the corresponding salt (carbonate, hydroxide, chloride), from spodumene and regardless of the route used (acid or alkaline digestion), contain intrinsic disadvantages, such as the formation of high residue levels of sulfate ions and heavy metals.

In addition, in the acid digestion, about 0.95 tons of aluminosilicose residue is generated for each ton of processed ore, indicating that only Li is recovered from the spodumene, with Al and Si dispensed in the residue. In Brazil, only the acid route is used on an industrial scale, with lithium carbonate being the product of greater demand <sup>[40]</sup>.

Therefore, the strategy used to reduce the formation of these residues involved adjusting the parameters at each processing step during the extraction to simultaneously obtain zeolites how byproduct.

To sum up, the objective of this doctoral thesis is to study the mechanisms of synthesis and to develop means for the extraction of lithium (lithium carbonate) that allows the recovery of zeolite-rich byproduct.

After the brief literature review presented in this chapter (Chapter 3), the Chapter 4 and Chapter 5 are the first chapters addressing this problematic, describing the effects of the calcination step on lithium extraction, seeking to elucidate the reaction mechanism between beta-spodumene and  $\text{Na}_2\text{CO}_3$  in the conversion to  $\text{Li}_2\text{CO}_3$ .

Afterward, the zeolites obtained in the lithium extraction routes, of MFI topology (Chapter 6) and cage/channel-types (Chapter 7), are presented. Finally, the last considerations are addressed in Chapter 8.

## References

- [1] NPCS. **Handbook on rare earth metals and alloys** (Properties, extraction, preparation and applications), Asia Pacific Business Press. 2009.
- [2] LAZUEN, J., BAYLIS, R., MERRIMAN, D., & GOTO, M.; **Lithium: Global industry, markets and outlook**, Roskill. 2018.
- [3] SANTOS, L. L., NASCIMENTO, R. M., PERGHER, S. B. C.; **Processo para obtenção dos materiais LPM-15, LPM-16 e LPM-17, com topologias zeolíticas LTA, FAU e MOR, respectivamente, como subproduto da extração do lítio a partir do beta-espodumênio**. BR Patent No 10,2018,016312,4. 2018.
- [4] SANTOS, L. L., NASCIMENTO, R. M., PERGHER, S. B. C.; **Processo para obtenção dos materiais LPM-18 e LPM-19, com topologias zeolíticas MFI e LTT, respectivamente, como subproduto da extração do lítio a partir do beta-espodumênio**. BR Patent No 10,2018,016339,6. 2018.
- [5] SWAIN, B.; Recovery and recycling of lithium: a review. **Sep and Purif Technol.**, 172 (2017), p. 388-403.
- [6] WIETELMANN, U., & BAUER, R. J.; **Lithium and lithium compounds**, Ullmann's Encyclopedia of Industrial Chemistry. 2000.
- [7] PELTOSAARI, O., TANSKANEN, P., HEIKKINEN, E. P., & FABRITIUS, T.;  $\alpha \rightarrow \gamma \rightarrow \beta$ -phase transformation of spodumene with hybrid microwave and conventional furnaces. **Minerals Engineering**, 82 (2015), p. 54-60.
- [8] PAES, V. J. C., SANTOS, L. D., TEDESCHI, M. F., & BETIOLLO, L. M.; **Avaliação do potencial do lítio no Brasil: área do Médio Rio Jequitinhonha, nordeste de Minas Gerais**, Belo Horizonte: CPRM. 2016.
- [9] MOMMA, K., & IZUMI, F.; VESTA: a three-dimensional visualization system for electronic and structural analysis. **J. Appl. Cryst.**, 41.3 (2008), p. 653-658.
- [10] HANSON, R. M., PRILUSKY, J., RENJIAN, Z., NAKANE, T., & SUSSMAN, J. L.; JSmol and the next-generation web-based representation of 3D molecular structure as applied to proteopedia. **Isr. J. Chem.**, 53 (2013), p. 207-216.
- [11] ALMEIDA, A. L.; **Lítio: Processos de obtenção, aplicações e perspectivas de produção no Brasil**, São Paulo: Centro Técnico Aeroespacial. 1973.

- [12] DNPM. **Sumário Mineral Brasileiro: Lítio**, Brasília: Departamento Nacional de Produção Mineral. Base-years: 2006 to 2017.
- [13] USGS. **Mineral Commodity Summaries: Lithium**, Reston: U.S. Department of the Interior and U.S. Geological Survey. Base-years: 2006 to 2017.
- [14] SHARMA, Y.; **Production of lithium hydroxide**. U.S. Patent No 9,988,279. 2018.
- [15] BRAGA, P. F. A., & FRANÇA, S. C. A.; **Tecnologias para produção de carbonato e hidróxido de lítio a partir de espodumênio e ambligonita**, Rio de Janeiro: CETEM/MCT. 2011.
- [16] MARGARIDO, F., VIECELI, N., DURÃO, F., GUIMARÃES, C., & NOGUEIRA, C. A.; Minerio-metallurgical processes for lithium recovery from pegmatitic ores. **Comunicações Geológicas**, 101 (2014), p. 795-798.
- [17] LONDON, D.; **Pegmatites**, Quebec: Mineralogical Association of Canada. 2008.
- [18] HAHN, H. T., & TSAI, S. W.; **Introduction to composite materials**, London: Routledge. 1980.
- [19] SOLTAN, A. M., PÖLLMANN, H., KADEN, R., KÖNIG, A., EL-RAOOF, F. A., ELTAHER, M., & SERRY, M.; Degradation of aluminosilicate refractories: An integrated approach. **J Eur Ceram Soc.**, 35 (2015), p. 4573-4592.
- [20] OSARENMWINDA, & J., ABEL, C. P.; Performance evaluation of refractory bricks produced from locally sourced clay materials. **J Ap Sci and Enviro Manage.**, 18 (2014), p. 151-157.
- [21] **ABNT NBR ISO 528** (2014). Produtos refratários – Determinação do cone pirométrico equivalente (refratariedade), p. 1-4.
- [22] **ABNT NBR 10237** (2014). Materiais refratários – Classificação, p. 1-9.
- [23] **ABNT NBR 8826** (2014). Materiais refratários – Terminologia, p. 1-71.
- [24] COOK, R. B.; **Handbook of mineralogy: borates, carbonates, sulfates**, United Kingdom: Taylor & Francis. 2004.
- [25] OSTERTAG, W., FISCHER, G. R., & WILLIAMS, J. P.; Thermal expansion of synthetic  $\beta$ -spodumene and  $\beta$ -spodumene-silica solid solutions. **J Am Ceram Soc.**, 51 (1968), p. 651-654.

- [26] LI, C., & PEACOR, D. R.; The crystal structure of  $\text{LiAlSi}_2\text{O}_6$ -II (“ $\beta$ -spodumene”). **Z Kristallogr Cryst Mater.**, 126 (1968), p. 46-65.
- [27] CHOUBEY, P. K., KIM, M. S., SRIVASTAVA, R. R., LEE, J. C., & LEE, J. Y.; Advance review on the exploitation of the prominent energy-storage element: Lithium. Part I: From mineral and brine resources. **Minerals Engineering**, 89 (2016), p. 119-137.
- [28] POPLE, J. A.; Publisher's note: Sir John A. Pople, 1925-2004. **J Comput Chem.**, 25 (2004), p. v-viii.
- [29] MAURICE, A., & OLIVIER, C. A.; **Carbonatizing roast of lithiumbearing ores**. U.S. Patent No 3,380,802. 1968.
- [30] STAMP, A., LANG, D. J., & WAGER, P. A.; Environmental impacts of a transition toward e-mobility: the present and future role of lithium carbonate production. **Journal of Cleaner Production**, 23.1 (2012), p. 104-112.
- [31] CHEN, Y., TIAN, Q., CHEN, B., SHI, X., & LIAO, T.; Preparation of lithium carbonate from spodumene by a sodium carbonate autoclave process. **Hydrometallurgy**, 109.1-2 (2011), p. 43-46.
- [32] KUANG, G., LIU, Y., LI, H., XING, S., LI, F., & GUO, H.; Extraction of lithium from  $\beta$ -spodumene using sodium sulfate solution. **Hydrometallurgy**, 177 (2018), p. 49-56.
- [33] AVERILL, W. A., & OLSON, D. L.; A review of extractive processes for lithium from ores and brines. **Lithium Needs and Resources**, (1978), p. 305-313.
- [34] PERRY, D. L.; **Handbook of inorganic compounds**, Boca Raton: CRC press. 2016.
- [35] HAYNES, W. M.; **Handbook of chemistry and physics** (Aqueous Solubility of Inorganic Compounds at Various Temperatures), Boca Raton: CRC press. 2014.
- [36] MAURICE, A.; **Process for producing lithium carbonate with concomitant recovery of reactants**. U.S. Patent No 3,131,022. 1964.
- [37] VICTOR, K. A.; **Method of recovering lithium compounds from lithium minerals**. U.S. Patent No 2,662,809. 1953.

- [38] MESHARAM, P., PANDEY, B. D., & MANKHAND, T. R.; Extraction of lithium from primary and secondary sources by pre-treatment, leaching and separation: A comprehensive review. **Hydrometallurgy**, 150 (2014), p. 192-208.
- [39] MAURICE, A.; **Lithium carbonate production**. U.S. Patent No 3,112,171. 1963.
- [40] OLIVEIRA, M. S. M., NASCIMENTO, R. M., PERGHER, S. B. C.; **Síntese do material zeolítico LPM-11 de tipologia MOR a partir do resíduo silicoaluminoso gerado na extração do lítio do espodumênio**. BR Patent No 10,2017,016712,7. 2017.
- [41] OLIVEIRA, M. S. M., NASCIMENTO, R. M., PERGHER, S. B. C.; **Síntese do material zeolítico LPM-12 de tipologia EDI a partir do resíduo silicoaluminoso gerado na extração do lítio do espodumênio**. BR Patent No 10,2017,016757,7. 2017.
- [42] BAERLOCHER, C., MCCUSKER, L. B., & OLSON, D. H.; **Atlas of Zeolite Framework Types**, New York: Elsevier. 2007.
- [43] CHICA, A., CORMA, A., & MIGUEL, P. J.; Isomerization of C5-C7 n-alkanes on unidirectional large pore zeolites: activity, selectivity and adsorption features. **Catalysis Today**, 65.2-4 (2001), p. 101-110.
- [44] MARTÍNEZ, C., & CORMA, A.; Inorganic molecular sieves: Preparation, modification and industrial application in catalytic processes. **Coord Chem Rev.**, 255.13-14 (2011), p. 1558-1580.
- [45] BOUDART, M., & DJÉGA-MARIADASSOU, G.; **Kinetic of heterogeneous catalytic reactions** (Vol. 767), Princeton: Princeton University press. 2014.
- [46] BYRAPPA, K.; & YOSHIMURA, M.; **Handbook of hydrothermal technology**, (2013), p. 269-347.
- [47] FLANIGEN, E. M.; Zeolites and molecular sieves an historical perspective. **Stud Surf Sci Catal.**, 58 (1991), p. 13-34.
- [48] DEGNAN, T. F.; Applications of zeolites in petroleum refining. **Topics in Catalysis**, 13.4 (2000), p. 349-356.
- [49] CUNDY, C. S., & COX, P. A.; The hydrothermal synthesis of zeolites: history and development from the earliest days to the present time. **Chemical Reviews**, 103.3 (2003), p. 663-702.

- [50] VAN BEKKUM, H., FLANIGEN, E. M., JACOBS, P. A., & JANSEN, J. C.; **Studies in surface science and catalysis** (Chap. 2), New York: Elsevier. 2001.
- [51] FONTANA, F.; **Memorie Mat Fis Soc Ital Sci.**, (1777), p. 679-691.
- [52] COHEN, B. L., & NASON, R.; A diffusion barrier charcoal adsorption collector for measuring Rn concentrations in indoor air. **Health Physics**, 50.4 (1986), p. 457-463.
- [53] THOMAS, J. M.; Turning points in catalysis. **Angew Chem Int Ed Engl.**, 33.9 (1994), p. 913-937.
- [54] D'AMOUR, A; **Ann Mines J.**, 17 (1840), p. 191-209.
- [55] MOREY, G W; & INGERSON, E; **Economic Geology J.**, 32 (1837), p. 607-771.
- [56] EICHHORN, H; **Poggendorff Ann Phys Chem.**, 105 (1858), p. 126-135.
- [57] CLAIRE-DEVILLE, H. de St.; **Comptes Rendus Chimie**, 54 (1862), p. 324-333.
- [58] BRAILSFORD, A. D., & WYNBLATT, P.; The dependence of Ostwald ripening kinetics on particle volume fraction. **Acta Metallurgica**, 27.3 (1979), p. 489-497.
- [59] FRIEDEL, G.; **Bull SOC Franc Miner Crystallography**, 19 (1896), p. 94-118.
- [60] GRANDJEAN, F.; **Comptes Rendus Chimie**, 149 (1909), p. 866-868.
- [61] WEIGEL, O., & STEINHOFF, E. Z.; **Kristallogr Kristallgeom Kristallphys Kristallchem.**, 61 (1925), p. 125-154.
- [62] LEONARD, R. J.; **Handbook Zeolites in industrial separation and catalysis** (The hydrothermal alteration of certain silicate minerals), New Jersey: Wiley. 2010.
- [63] TAYLOR, W. H.; **Kristallogr Kristallgeom Kristallphys Kristallchem.**, 74 (1930), p. 1-37.
- [64] PAULING, L.; The structure of the micas and related minerals. **Proc Natl Acad Sci**, 16.2 (1930), p. 123-129.
- [65] McBRAIN, J. W.; **The sorption of gases and vapors by solids** (Chap. 5), London: Rutledge and Sons. 1932.

- [66] JACOBS, P. A., FLANIGEN, E. M., JANSEN, J. C., & VAN BEKKUM, H.; **Introduction to zeolite science and practice** (Vol. 137), Amsterdam: Elsevier. 2001.
- [67] BARRER, R. M.; **J Chem Soc. Ind.**, 64 (1945), p. 130.
- [68] BARRER, R. M.; 435. Syntheses and reactions of mordenite. **J Chem Soc. (resumed)**, 67 (1948), p. 2158-2163.
- [69] BRECK, D. W., EVERSOLE, W. G., MILTON, R. M., REED, T. B., & THOMAS, T. L.; Crystalline zeolites. I. The properties of a new synthetic zeolite, type A. **J Am Chem Soc**, 78.23 (1956), p. 5963-592.
- [70] CORMA, A.; From microporous to mesoporous molecular sieve materials and their use in catalysis. **Chemical Reviews**, 97.6 (1997), p. 2373-2420.
- [71] MOTA, C. J. A.; **Aplicações e necessidades da Petrobrás à produção de gasolina: Química e tecnologia para o desenvolvimento**, Rio de Janeiro: Cenpes. 1994.
- [72] WEITKAMP, J.; Zeolites and catalysis. **Sol Stat Ion**, 131.1-2 (2000), p. 175-188.
- [73] KERR, G. T.; Zeolite ZK-5: a new molecular sieve. **Science**, 140.3574 (1963), p. 1412-1412.
- [74] WADLINGER, R. L., KERR, G. T., & ROSINSKI, E. J.; **Catalytic composition of a crystalline zeolite**. US Patent No 3,308,069. 1967.
- [75] FYFE, C. A., STROBL, H., KOKOTAILO, G. T., KENNEDY, G. J., & BARLOW, G. E.; Ultrahigh-resolution silicon-29 solid-state MAS NMR investigation of sorbate and temperature-induced changes in the lattice structure of zeolite ZSM-5. **J Am Chem Soc.**, 110.11 (1988), p. 3373-3380.
- [76] CUNDY, C. S., & COX, P. A.; The hydrothermal synthesis of zeolites: history and development from the earliest days to the present time. **Chemical Reviews**, 103.3 (2003), p. 663-702.
- [77] MARCELO, J. L.; **Thesis**, Brasília: Chemistry department/UnB. 2007.
- [78] BRECK, D. W.; **Zeolite molecular sieves: structure, chemistry and use**, New York: John Wiley and Sons. 1974.
- [79] THOMAS, J. M.; Turning points in catalysis. **Angew Chem Int Ed Engl.**, 33.9 (1994), p. 913-937.

- [80] JOHNSON, E. B. G., & ARSHAD, S. E.; Hydrothermally synthesized zeolites based on kaolinite: A review. **Applied Clay Science**, 97 (2014), p. 215-221.
- [81] FLANIGEN, E. M.; A review and new perspectives in zeolite crystallization. **Advances in Chemistry Series**, 121 (1973), p. 119-139.
- [82] NAGY, J. B.; **Synthesis, characterization and use of zeolitic microporous materials**, Szeged: DecaGen Ltd. 1998.
- [83] CORRÉA, M. L. S., WALLAU, M., & SCHUCHARDT, U.; AIPO-type zeolites: synthesis, characterization and catalytic properties. **Química Nova**, 19.1 (1996), p. 43-50.
- [84] DANIELS, R. H., KERR, G. T., & ROLLMANN, L. D.; Cationic polymers as templates in zeolite crystallization. **J Am Chem Soc.**, 100.10 (1978), p. 3097-3100.
- [85] SANCHEZ, C. M., PARIENTE, J. P.; **Zeolites and ordered porous solids: fundamentals and applications**, València: Editorial Universitat Politècnica de València. 2011.
- [86] WILSON, S. T., LOK, B. M., MESSINA, C. A., CANNAN, T. R., & FLANIGEN, E. M.; Aluminophosphate molecular sieves: A new class of microporous crystalline inorganic solids. **J Am Chem Soc.**, 104 (1982), p. 1146-1147.
- [87] LOK, B. M., CANNAN, T. R., & MESSINA, C. A.; The role of organic molecules in molecular sieve synthesis. **Zeolites**, 3.4 (1983), p. 282-291.
- [88] CLERICI, M. G., BELLUSSI, G., & ROMANO, U.; Synthesis of propylene oxide from propylene and hydrogen peroxide catalyzed by titanium silicalite. **J Catal.**, 129.1 (1991), p. 159-167.
- [89] DEROUANE, E. G.; Shape selectivity in catalysis by zeolites: the nest effect. **J Catal.**, 100.2 (1986), p. 541-544.
- [90] JACOBS, P. A., & MARTENS, J. A.; **Synthesis of high-silica aluminosilicate zeolites**, Amsterdam: Elsevier Science Publishers. 1987.
- [91] DAVIS, M. E., SALDARRIAGA, C., MONTES, C., GARCES, J., & CROWDERT, C.; A molecular sieve with eighteen-membered rings. **Nature**, 331 (1988), p. 698-699.

- [92] GUTH, J. L., KESSLER, H., HIGEL, J. M., LAMBLIN, J. M., PATARIN, J., SEIVE, A., CHEZEAU, J. M., & WEY, R.; **Zeolite synthesis in the presence of fluoride ions** (Chap. 13), ACS Symposium Series. 1989.
- [93] BELL, A. T.; Applications of NMR spectroscopy to the study of zeolite synthesis. **ACS Symposium Series**, 176 (1989), p. 66-82.
- [94] CARO, J.; Guidelines for mastering the properties of molecular sieves. **Zeitschrift für Physikalische Chemie**, 1776.1 (1992), p. 127-132.
- [95] CORMA, A., DÍAZ-CABAÑAS, M. J., JORDÁ, J. L., MARTINEZ, C., & MOLINER, M.; High-throughput synthesis and catalytic properties of a molecular sieve with 18- and 10-member rings. **Nature**, 443 (2006), p. 842-845.
- [96] OH, S. C., NGUYENDO, T., HE, Y., FILIE, A., WU, Y., TRAN, D. T., LEE, I. C., & LIU, D.; External surface and pore mouth catalysis in hydrolysis of inulin over zeolites with different micropore topologies and mesoporosities. **Catal Sci Technol.**, 7.5 (2017), p. 1153-1166.
- [97] BECK, J. S., VARTULI, J. C., ROTH, W. J., LEONOWICZ, M. E., KRESGE, C. T., SCHMITT, K. D., CHU, C. T. W., OLSON, D. H., SHEPPARD, E. W., MCCULLEN, S. B., HIGGINS, J. B., & SCHLENKER, J. L.; New family of mesoporous molecular sieves prepared with liquid crystal templates. **J Am Chem Soc.**, 14 (1992), p. 10834-10843.
- [98] JACOBS, P. A., & GILSON, J. P.; **Zeolite microporous solids: synthesis, structure and reactivity**, Dordrecht: Kluwer. 1992.
- [99] GONTHIER, S., & THOMPSON, R. W.; **Effects of seeding on zeolite crystallization, and the growth behavior of seeds**, Amsterdam: Elsevier. 1994.
- [100] KESSLER, H., & PATARIN, J.; The opportunities of the fluoride route in the synthesis of microporous materials. **Stud Surf Sci Catal.**, 85 (1994), p. 75-113.
- [101] MARTENS, J. A., VANBUTSELE, G., JACOBS, P. A., DENAYER, J., OCAKOGLU, R., BARON, G., ARROYO, J. A. M., THYBAUT, J., & MARIN, G. B.; Evidences for pore mouth and key-lock catalysis in hydroisomerization of long n-alkanes over 10-ring tubular pore bifunctional zeolites. **Catalysis Today**, 65.2-4 (2001), p. 111-116.

- [102] LEWIS, D., & THOMAS, J.; Application of computer modeling to the mechanisms of synthesis of microporous catalytic materials. **Faraday Discussions**, 106 (1997), p. 451-471.
- [103] MORRIS, R. E., & WEIGEL, S. J.; The synthesis of molecular sieves from nonaqueous solvents. **Chem Soc Rev.**, 26.4 (1997), p. 309-317.
- [104] LOBO, R. F., TSAPATSIS, M., FREYHARDT, C. C., KHODABANDEH, S., WAGNER, P., CHEN, C. Y., BALKUS JR, K. J., ZONES, S. I., & DAVIS, M. E.; Characterization of the extra-large-pore zeolite UTD-1. **J Am Chem Soc.**, 119 (1997), p. 8474-8484.
- [105] CORMA, A., FORNES, V., PERGHER, S. B., MAESEN, T. L., & BUGLASS, J. G.; Delaminated zeolite precursors as selective acidic catalysts. **Nature**, 396 (1998), p. 353-356.
- [106] CORMA, A., DIAZ, U., DOMINE, M. E., & FORNÉS, V.; AlITQ-6 and TiITQ-6: synthesis, characterization, and catalytic activity. **Angewandte Chemie**, 112 (2000), p. 1559-1561.
- [107] CUNDY, C. S.; Microwave techniques in the synthesis and modification of zeolite catalysts. A review. **Collect Czechoslov Chem Commun.**, 63.11 (1998), p. 1699-1723.
- [108] CAMBLOR, M. A., CORMA, A., DÍAZ-CABAÑAS, M. J., & BAERLOCHER, C.; Synthesis and structural characterization of MWW type zeolite ITQ-1, the pure silica analog of MCM-22 and SSZ-25. **J Phys Chem B.**, 102.1 (1998), p. 44-51.
- [109] CORMA, A., FORNES, V., PERGHER, S. B., MAESEN, T. L., & BUGLASS, J. G.; Delaminated zeolite precursors as selective acidic catalysts. **Nature**, 396.6709 (1998), p. 353-356.
- [110] MILLINI, R., PEREGO, G., & BELLUSSI, G.; Synthesis and characterization of boron-containing molecular sieves. **Topics in Catalysis**, 9.1-2 (1999), p. 13-34.
- [111] FRICKE, R., KOSSLICK, H., LISCHKE, G., & RICHTER, M.; Incorporation of gallium into zeolites: syntheses, properties and catalytic application. **Chemical reviews**, 100.6 (2000), p. 2303-2406.
- [112] BALKUS, K. J.; Synthesis of large pore zeolites and molecular sieves. **Prog in Inorg Chem.**, 50 (2001), p. 217-268.

- [113] ROBSON, H.; **Verified synthesis of zeolitic materials**, Houston: Gulf Professional Publishing. 2001.
- [114] CASTAÑEDA, R., CORMA, A., FORNÉS, V., REY, F., & RIUS, J.; Synthesis of a new zeolite structure ITQ-24, with intersecting 10-and 12-membered ring pores. **J Am Chem Soc.**, 125.26 (2003), p. 7820-7821.
- [115] JAN, D. Y., LEWIS, G. J., MEZZA, T. M., MOSCOSO, J. G., PATTON, R. L., KOLJACK, M. P., & TOTA, P. V.; Synthesis, characterization, and applications of the new zeolite UZM-5. **Stud Surf Sci Catal.**, 154 (2004), p. 1332-1340.
- [116] CORMA, A., REY, F., RIUS, J., SABATER, M. J., & VALENCIA, S.; Supramolecular self-assembled molecules as organic directing agent for synthesis of zeolites. **Nature**, 431.7006 (2004), p. 287.
- [117] CANTÍN, A., CORMA, A., LEIVA, S., REY, F., RIUS, J., & VALENCIA, S.; Synthesis and structure of the bidimensional zeolite ITQ-32 with small and large pores. **J Am Chem Soc.**, 127.33 (2005), p. 11560-11561.
- [118] CORMA, A., DIAZ-CABANAS, M. J., JORDA, J. L., REY, F., SASTRE, G., & STROHMAIER, K. G.; A zeolitic structure (ITQ-34) with connected 9-and 10-ring channels obtained with phosphonium cations as structure directing agents. **J Am Chem Soc.**, 130.49 (2008), p. 16482-16483.
- [119] SUN, J., BONNEAU, C., CANTÍN, Á., CORMA, A., DÍAZ-CABAÑAS, M. J., MOLINER, M., ZHANG, D., LI, M., & ZOU, X.; The ITQ-37 mesoporous chiral zeolite. **Nature**, 458.7242 (2009), p. 1154-1157.
- [120] CORMA, A., DÍAZ-CABAÑAS, M. J., JIANG, J., AFEWORKI, M., DORSET, D. L., SOLED, S. L., & STROHMAIER, K. G.; Extra-large pore zeolite (ITQ-40) with the lowest framework density containing double four-and double three-rings. **Proc Natl Acad Sci.**, 107.32 (2010), p. 13997-14002.
- [121] JIANG, J., JORDA, J. L., DIAZ-CABANAS, M. J., YU, J., & CORMA, A.; The synthesis of an extra-large-pore zeolite with double three-ring building units and a low framework density. **Angew Chem.**, 49.29 (2010), p. 4986-4988.
- [122] JIANG, J., JORDA, J. L., YU, J., BAUMES, L. A., MUGNAIOLI, E., DIAZ-CABANAS, M. J., KOLB, U., & CORMA, A.; Synthesis and structure determination of the hierarchical meso-microporous zeolite ITQ-43. **Science**, 333.6046 (2011), p. 1131-1134.

- [123] JORDÁ, J. L., REY, F., SASTRE, G., VALENCIA, S., PALOMINO, M., CORMA, A., SEGURA, A., ERRANDONEA, D., LACOMBA, R., MANJÓN, F. J., GOMIS, Ó., KLEPPE, A. K., JEPHCOAT, A. P., AMBOAGE, M., & RODRÍGUEZ-VELAMAZÁN, J. A.; Synthesis of a novel zeolite through a pressure-induced reconstructive phase transition process. **Angew Chem.**, 52.40 (2013), p. 10652-10656.
- [124] MARTÍNEZ-FRANCO, R., MOLINER, M., YUN, Y., SUN, J., WAN, W., ZOU, X., & CORMA, A.; Synthesis of an extra-large molecular sieve using proton sponges as organic structure-directing agents. **Proc Natl Acad Sci.**, 110.10 (2013), p. 3749-3754.
- [125] ROJAS, A., ARTEAGA, O., KAHR, B., & CAMBLOR, M. A.; Synthesis, structure, and optical activity of HPM-1, a pure silica chiral zeolite. **J Am Chem Soc.**, 135.32 (2013), p. 11975-11984.
- [126] CHEN, F. J., XU, Y., & DU, H. B.; An extra-large-pore zeolite with intersecting 18-, 12-, and 10-membered ring channels. **Angew Chem.**, 53.36 (2014), p. 9592-9596.
- [127] JIANG, J., YUN, Y., ZOU, X., JORDA, J. L., & CORMA, A.; ITQ-54: a multi-dimensional extra-large pore zeolite with 20× 14× 12-ring channels. **Chem Sci.**, 6.1 (2015), p. 480-485.
- [128] LI, J., CORMA, A., & YU, J.; Synthesis of new zeolite structures. **Chem Soc Rev.**, 44.20 (2015), p. 7112-7127.
- [129] BAI, R., SUN, Q., WANG, N., ZOU, Y., GUO, G., IBORRA, S., CORMA, A., & YU, J.; Simple quaternary ammonium cations-templated syntheses of extra-large pore germanosilicate zeolites. **Chem Mat.**, 28.18 (2016), p. 6455-6458.
- [130] SCHWANKE, A. J.; **Thesis**, Natal: Department of Materials Science and Engineering/UFRN. 2016.
- [131] MELGUIZO, P. V.; **Thesis**, Natal: Department of Materials Science and Engineering/UFRN. 2017.
- [132] CANOS, A. C., GARCIA, F. R., VALENCIA, S. V., SANZ, A. C., & MORET, J. L. J.; **Material ITQ-55, method for preparation and use**. U.S. Patent No 9,856,145. 2018.

- [133] BIESEKI, L., SIMANCAS, R., JORDÁ, J. L., BERECIARTUA, P. J., CANTÍN, Á., SIMANCAS, J., PERGHER, S. B., VALENCIA, S., REY, F., & CORMA, A.; Synthesis and structure determination via ultra-fast electron diffraction of the new microporous zeolitic germanosilicate ITQ-62. **Chem Commun.**, 54.17 (2018), p. 2122-2125.
- [134] LIPPMAA, E., MAEGI, M., SAMOSON, A., TARMAK, M., & ENGELHARDT, G.; Investigation of the structure of zeolites by solid-state high-resolution silicon-29 NMR spectroscopy. **J Am Chem Soc.**, 103.17 (1981), p. 4992-4996.
- [135] GUO, P., SHIN, J., GREENAWAY, A. G., MIN, J. G., SU, J., CHOI, H. J., LIU, L., COX, P. A., HONG, S. B., WRIGHT, P. A., & ZOU, X.; A zeolite family with expanding structural complexity and embedded isorecticular structures. **Nature**, 524.7563 (2015), p. 74-78.
- [136] LI, Y., YU, J.; New stories of zeolite structures: their descriptions, determinations, predictions, and evaluations. **Chemical reviews**, 114.14 (2014), p. 7268-7316.
- [137] BRAGA, A. A. C., MORGON, N. H.; Descrições estruturais cristalinas de zeólitos. **Química Nova**, 30.1 (2007), p. 178-188.
- [138] **Gavrog**, “The Gavrog Project”, Olaf Delgado-Friedrichs, [Online]. Available: <[www.gavrog.org](http://www.gavrog.org)> [Access in Oct/2015].
- [139] **Mercury**, “The Cambridge Crystallographic Data Centre”, [Online]. Available: <<https://www.ccdc.cam.ac.uk/solutions/csd-system/components/mercury/>> [Access in Dec/2015].
- [140] LUZ, A. B. D.; **Zeólitas: propriedades e usos industriais**, Rio de Janeiro: CETEM. 1995.
- [141] LIU, X., MÄKI-ARVELA, P., AHO, A., VAJGLOVA, Z., GUN'KO, V. M., HEINMAA, I., KUMAR, N., ERÄNEN, K., SALMI, T., & MURZIN, D. Y.; Zeta potential of beta zeolites: influence of structure, acidity, pH, temperature and concentration. **Molecules**, 23.4 (2018), p. 946-959.
- [142] TASI, G., PÁLINKÓ, I., MOLNÁR, Á., & HANNUS, I.; Molecular shape, dimensions, and shape selective catalysis. **J Mol Struct.**, 666-667 (2003), p. 69-77.

- [143] ANOVITZ, L. M., & COLE, D. R.; Characterization and analysis of porosity and pore structures. **Rev Mineral Geochem.**, 80.1 (2015), p. 61-164.
- [144] CHICA, A., & SAYAS, S.; Effective and stable bioethanol steam reforming catalyst based on Ni and Co supported on all-silica delaminated ITQ-2 zeolite. **Catalysis Today**, 146.1-2 (2009), p. 37-43.
- [145] GEBBIE, J.; **Tese** (Doutorado), United Kingdom (The University of Manchester): Chemistry department, 2014.
- [146] KULPRATHIPANJA, S. (Ed.); **Zeolites in industrial separation and catalysis**. New Jersey: John Wiley & Sons. 2010.
- [147] ROUQUEROL, J., ROUQUEROL, F., LLEWELLYN, P., MAURIN, G., & SING, K. S.; **Adsorption by powders and porous solids: principles, methodology and applications**. Massachusetts: Academic press. 2013.
- [148] ALMEIDA, K. A., MARTINS, L., & CARDOSO, D.; Preparação e propriedades de zeólitas faujasita contendo cátions amônio. **Química Nova**, 33.5 (2010), p. 1077-1081.
- [149] VAN GRIEKEN, R., SOTELO, J. L., MENENDEZ, J. M., & MELERO, J. A.; Anomalous crystallization mechanism in the synthesis of nanocrystalline ZSM-5. **Micropor and Mesopor Mat.**, 39.1-2 (2000), p. 135-147.
- [150] CALDEIRA, V. P. S.; **Dissertation**, Natal: Chemistry department/UFRN. 2011.
- [151] AL-JABARI, M.; Kinetic models for adsorption on mineral particles comparison between Langmuir kinetics and mass transfer. **Environ Technol & Innov.**, 6 (2016), p. 27-37.
- [152] FOO, K. Y., & HAMEED, B. H.; Insights into the modeling of adsorption isotherm systems. **Chem Eng J.**, 156.1 (2010), p. 2-10.
- [153] BAERLOCHER, C.; & MCCUSKER, L. B.; **Database of zeolite structures**. International Zeolite Association, IZA, [Online]. Available: <<http://www.iza-structure.org/databases>> [Access in July/2018].
- [154] WECKHUYSSEN, B. M., & YU, J.; Recent advances in zeolite chemistry and catalysis. **Chem Soc Rev.**, 44.20 (2015), p. 7022-7024.
- [155] MOLINER, M., MARTÍNEZ, C., & CORMA, A.; Multipore zeolites: synthesis and catalytic applications. **Angew Chem Int Ed Engl.**, 54.12 (2015), p. 3560-3579.

- [156] WEITKAMP, J., & PUPPE, L. (Eds.); **Catalysis and zeolites: fundamentals and applications**, Berlin: Springer. 2013.
- [157] Li, X., Li, K., Tao, S., Ma, H., Xu, R., Wang, B., Wang, P., & Tian, Z.; Ionothermal synthesis of LTA-type aluminophosphate molecular sieve membranes with gas separation performance. **Microp and Mesop Mat.**, 228 (2016), p. 45-53.
- [158] SHIRAZIAN, S., & ASHRAFIZADEH, S. N.; LTA and ion-exchanged LTA zeolite membranes for dehydration of natural gas. **J Ind Eng Chem.**, 22 (2015), p. 132-137.
- [159] YIN, X., LI, Z., WANG, S., CHU, N., YANG, J., & WANG, J.; Hydrothermal synthesis of hierarchical zeolite T aggregates using tetramethylammonium hydroxide as single template. **Microp and Mesop Mat.**, 201 (2015), p. 247-257.
- [160] CHANG, C. D.; Methanol conversion to light olefins. **Catal Surf Sci.**, (2017), p. 23-45.
- [161] VERBOEKEND, D., & PÉREZ-RAMÍREZ, J.; Desilication mechanism revisited: highly mesoporous all-silica zeolites enabled through pore-directing agents. **Chem-A Eur J.**, 17.4 (2011), p. 1137-1147.
- [162] WANG, H., & PINNAVAIA, T. J.; MFI zeolite with small and uniform intracrystal mesopores. **Angewandte Chemie**, 118.45 (2006), p. 7765-7768.
- [163] LI, X., PRINS, R., & BOKHOVEN, J. A.; Synthesis and characterization of mesoporous mordenite. **Journal of Catalysis**, 262.2 (2009), p. 257-265.
- [164] KHALIL, U., MURAZA, O.; Microwave-assisted hydrothermal synthesis of mordenite zeolite: Optimization of synthesis parameters. **Microp and Mesop Mat.**, 232 (2016), p. 211-217.
- [165] FRISING, T.; & LEFLAIVE, P.; Extraframework cation distributions in X and Y faujasite zeolites: A review. **Microp and Mesop Mat.**, 114.1-3 (2008), p. 27-63.
- [166] GIANETTO, G. E.; **Zeolitas: características, propiedades e aplicaciones industriales**, Caracas: Editorial Innovacion Tecnologica. 1989.

- [167] BODART, P., NAGY, J. B., GABELICA, Z., & DEROUANE, E. G.; Factors governing the synthesis of zeolites from silicoaluminate hydrogels: a comparative study of the crystallization mechanisms of zeolites Y, mordenite and ZSM-5. **J Chim Phys.**, 83 (1986), p. 777-790.
- [168] PETROV, I., & MICHALEV, T.; Synthesis of zeolite A: A review. (2012), p. 1-6.
- [169] MARTÍNEZ-FRANCO, R., PARIS, C., MARTÍNEZ-ARMERO, M. E., MARTÍNEZ, C., MOLINER, M., & CORMA, A.; High-silica nanocrystalline beta zeolites: efficient synthesis and catalytic application. **Chemical Science**, 7.1 (2016), p. 102-108.
- [170] CUNDY, C. S., & COX, P. A.; The hydrothermal synthesis of zeolites: Precursors, intermediates and reaction mechanism. **Microp and Mesop Mat.**, 82.1-2 (2005), p. 1-78.
- [171] KARGE, H. G.; Post-synthesis modification of microporous materials by solid-state reactions. **Stud Surf Sci Catal.**, 105 (1997), p. 1901-1948.
- [172] ZAAROUR, M., DONG, B., NAYDENOVA, I., RETOUX, R., & MINTOVA, S.; Progress in zeolite synthesis promotes advanced applications. **Microp and Mesop Mat.**, 189 (2014), p. 11-21.
- [173] LOBO, R. F., ZONES, S. I., & DAVIS, M. E.; Structure-direction in zeolite synthesis. **J Incl Phenom Macrocycl Chem.**, 21.1-4 (1995), p. 47-78.
- [174] OLEKSIK, M. D., SOLTIS, J. A., CONATO, M. T., PENN, R. L., & RIMER, J. D.; Nucleation of FAU and LTA zeolites from heterogeneous aluminosilicate precursors. **Chemistry of Materials**, 28.14 (2016), p. 4906-4916.
- [175] LILLERUD, K. P., & RAEDER, J. H.; On the synthesis of erionite-offretite intergrowth zeolites. **Zeolites**, 6.6 (1986), p. 474-483.
- [176] GRAND, J., AWALA, H., & MINTOVA, S.; Mechanism of zeolites crystal growth: new findings and open questions. **Cryst Eng Comm.**, 18.5 (2016), p. 650-664.
- [177] CHAOUATI, N., SOUALAH, A., CHATER, M., TARIGHI, M., & PINARD, L.; Mechanisms of coke growth on mordenite zeolite. **Journal of Catalysis**, 344 (2016), p. 354-364.

- [178] RIGO, R. T., PERGHER, S. B., PETKOWICZ, D. I., & DOS SANTOS, J. H.; A new procedure for A zeolite synthesis from natural clays. **Química Nova**, 32.1 (2009), p. 21-25.
- [179] ZHOU, R., ZHONG, S., LIN, X., & XU, N.; Synthesis of zeolite T by microwave and conventional heating. **Microp and Mesop Mat.**, 124.1-3 (2009), p. 117-122.
- [180] JUSOH, N., YEONG, Y. F., MOHAMAD, M., LAU, K. K., & SHARIFF, A. M.; Rapid-synthesis of zeolite T via sonochemical-assisted hydrothermal growth method. **Ultrason Sonochem.**, 34 (2017), p. 273-280.
- [181] PASHKOVA, V., KLEIN, P., DEDECEK, J., TOKAROVÁ, V., & WICHTERLOVÁ, B.; Incorporation of Al at ZSM-5 hydrothermal synthesis. **Microp and Mesop Mat.**, 202 (2015), p. 138-146.
- [182] VERBOEKEND, D., NUTTENS, N., LOCUS, R., VAN AELST, J., VEROLME, P., GROEN, J. C., PÉREZ-RAMÍREZ, J., & SELS, B. F.; Synthesis, characterisation, and catalytic evaluation of hierarchical faujasite zeolites: milestones, challenges, and future directions. **Chem Soc Rev.**, 45.12 (2016), p. 3331-3352.
- [183] SHI, J., WANG, Y., YANG, W., TANG, Y., & XIE, Z.; Recent advances of pore system construction in zeolite-catalyzed chemical industry processes. **Chem Soc Rev.**, 44.24 (2015), p. 8877-8903.
- [184] KIM, J., CHO, K., & RYOO, R.; High catalytic performance of surfactant-directed nanocrystalline zeolites for liquid-phase Friedel-Crafts alkylation of benzene due to external surfaces. **Appl Catal-A**, 470 (2014), p. 420-426.
- [185] RANGNEKAR, N., MITTAL, N., ELYASSI, B., CARO, J., & TSAPATSI, M.; Zeolite membranes: A review and comparison with MOFs. **Chem Soc Rev.**, 44.20 (2015), p. 7128-7154.
- [186] MAHMOUD, E., & LOBO, R. F.; Recent advances in zeolite science based on advanced characterization techniques. **Microp and Mesop Mat.**, 189 (2014), p. 97-106.
- [187] BORDIGA, S., LAMBERTI, C., BONINO, F., TRAVERT, A., & THIBAUT-STARYK, F.; Probing zeolites by vibrational spectroscopies. **Chem Soc Rev.**, 44.20 (2015), p. 7262-7341.

- [188] VAN SPEYBROECK, V., HEMELSOET, K., JOOS, L., WAROQUIER, M., BELL, R. G., & CATLOW, C. R. A.; Advances in theory and their application within the field of zeolite chemistry. **Chem Soc Rev.**, 44.20 (2015), p. 7044-7111.
- [189] WEI, Y., PARMENTIER, T. E., DE JONG, K. P., & ZEČEVIĆ, J.; Tailoring and visualizing the pore architecture of hierarchical zeolites. **Chem Soc Rev.**, 44.20 (2015), p. 7234-7261.
- [190] LLORCA, J., DE LA PISCINA, P. R., SALES, J., & HOMS, N.; Direct production of hydrogen from ethanolic aqueous solutions over oxide catalysts. **Chem Commun.**, 7 (2001), p. 641-642.
- [191] SAYAS, S., & CHICA, A.; Furfural steam reforming over Ni-based catalysts. Influence of Ni incorporation method. **Int J Hydrogen Energy**, 39.10 (2014), p. 5234-5241.

## Chapter 4. Calcination-free lithium extraction and simultaneous recovery of LTA-type zeolite

---

Leonardo L. dos Santos<sup>1</sup>; Rubens M. do Nascimento<sup>1</sup>; Sibebe B. C. Pergher<sup>2</sup>

<sup>1</sup> Department of Materials Science and Engineering, Federal University of Rio Grande do Norte, Natal 59078-97, Brazil.

<sup>2</sup> Department of Chemistry, Laboratório de Peneiras Moleculares, Federal University of Rio Grande do Norte, Natal 59078-97, Brazil.

**Abstract:** This article presents a methodology applied to lithium extraction from beta-spodumene based on an organic solvent-free synthesis that is calcination-free, through solubilization with sodium salts and reuse of the mother liquor, with lithium content quantified by atomic absorption (AAS) on the supernatant. Synthesis conditions were optimized to obtain simultaneous LTA-type zeolite, such as cubic morphology with spherical facets, and properties were evaluated from a computational simulation using density functional theory (DFT) to show the effects of cation exchange of  $\text{Na}^+/\text{Al}^{3+}$ ,  $\text{NH}_4^+/\text{Al}^{3+}$  and  $\text{Ca}^{2+}/\text{Al}^{3+}$  on zeolite stability and molecular diffusion from the size of pores, as well as the mobility of cations present in LTA-type zeolite evaluated through cation-exchange capacity (CEC).

**Keywords:** Lithium recovery. Calcination-free. LTA-type. Adsorptive properties. Molecular simulation. DFT study.

### Introduction

Lithium production processes from litiniferous aluminosilicates generally use the following mechanisms: (i) calcination and roasting, sulfate coprecipitation, ion exchange and organic-inorganic polymer blend sorption for the recovery of structural lithium; (ii) leaching in grinding circuit and flotation for the separation of byproducts; and (iii) chemical reduction by anhydrous chlorides or fluorides and electrolysis of chloride-fused salts or oxide-fluoride mixtures for the precipitation and purification of the lithium salt on the supernatant <sup>[1, 2]</sup>.

The lithium nature and content, the salt purity formed (carbonate, hydroxide, chloride, bromide, and n-butyllithium), and the physicochemical properties of the byproduct will determine the appropriate set of techniques [2].

Byproduct formation, normally based on complex sodium-lithium aluminosilicate, makes the extraction procedure more expensive, compromising the extraction yield due to the demand of organic solvents and actinide base for extraction of the remaining lithium, in addition to generating lithium-poor liquor with impurities for difficult separation [3].

Byproduct treatment has been targeted to molecular sieve synthesis (especially zeolites) and extraction postsynthesis, such as for MFI-, MOR- or EDI-types, although several aspects of the synthesis of these materials are still open for discussion: (i) kinetics and the apparent activation energy; (ii) starting material treatment dependence and the activation temperature; and (iii) Ostwald's rule of successive transformation for the first polymorph formed and its substitution by increasingly stable polymorphs [4-6].

According to their microporous nature, zeolites can accommodate various cations. The cation exchange in their network modifies the ability to selectively classify the various molecules based on their physical properties and pore size. Due to its low cost and high thermal stability, LTA-type zeolite has potential applications in separation processes and shape-selective catalysis [7].

The objectives of this study were to evaluate (i) the solubilization parameters of sodium salts in the conversion of beta-spodumene to  $\text{Li}_2\text{CO}_3$  in a calcination-free process; (ii) hydrothermal treatment conditions to optimize the process and obtain LTA-type zeolite; (iii) the precipitation rate of  $\text{Li}_2\text{CO}_3$  in relation to its yield and purity; (iv) cation mobility in the LTA-type zeolite through the cation-exchange capacity (CEC) in the presence of other electrolytes; and (v) structural modifications through cation exchange for  $\text{Na}^+$ ,  $\text{NH}_4^+$  and  $\text{Ca}^{2+}$ , and the possibility of estimating the molecules that can be adsorbed on the network through computer simulation, correlating experimental data by spectroscopy with the electronic structure modeled by density functional theory (DFT).

A computational simulation is a tool based on the fundamental laws of quantum mechanics that allows for mathematically simulating structures and chemical reactions, which allows the investigation of the effects of physical and chemical phenomena, helping to understand problems with difficult solutions from an experimental point of view.

## Experimental

### Raw materials.

The beta-spodumene was provided by Companhia Brasileira de Lítio (CBL), and the chemical composition is shown in Tab. 1 for Si/Al molar ratio = 2.6. The lithium content in the concentrate is limited because the maximum lithium content in the mineral spodumene is 3.73% Li <sup>[8]</sup>. All reagents used were of analytical grade without further purification.

Table 1. Chemical analysis of the beta-spodumene sample (wt%).

Component	SiO <sub>2</sub>	Al <sub>2</sub> O <sub>3</sub>	Li <sub>2</sub> O	Fe <sub>2</sub> O <sub>3</sub>	K <sub>2</sub> O	Others
Content (%)	68.97	22.31	6.43	0.92	0.42	<0.40

### Procedures.

The procedure and the initial synthesis methodology were based on the literature <sup>[8]</sup>. At first, sodium hydroxide (1.0 g) was dissolved to solubilize beta-spodumene (10.0 g) in a reflux system at 353 K for 120 min. The solution was divided into two equal volumes, (i) and (ii): (i) was treated with sodium aluminate, following the amount used for LTA-type zeolite synthesis (50.694% Al<sub>2</sub>O<sub>3</sub>, 34.596% Na<sub>2</sub>O, 14.710% H<sub>2</sub>O), and (ii) was treated with sodium carbonate (5.0 g) in an autoclave between 368 K and 523 K for 720 min. Volume (i) was added to volume (ii) and subjected to hydrothermal treatment between 368 K and 383 K in the range of 30-360 min.

The solution was filtered still warm, similar to the mother liquor recirculated for a new solubilization in sodium hydroxide solution with similar concentration as previously employed. The resulting solution was treated with ammonium bicarbonate, which was sufficient to promote the solubility of lithium carbonate, in reaction for 60 min and filtered. The solid content was separated from the supernatant and subjected to drying and heat treatment, while the supernatant was heated to evaporation of NH<sub>3</sub> and to Li<sub>2</sub>CO<sub>3</sub> insolubilization.

Evaluation of zeolite adsorptive properties.

a) Cation-exchange capacity

The methodology employed simple exchange consisting of placing the zeolite sample in contact with the solution of the ion to be changed under constant agitation until reaching saturation [9]. The concentration of the ions in solution was determined in the supernatant before and after contact with the zeolite.

The CECs of the synthesized zeolites were performed for the exchange of  $\text{Na}^+$  ions in the structure by  $\text{NH}_4^+$  and  $\text{Ca}^{2+}$  ions using solutions of  $0.1 \text{ mol.L}^{-1}$   $\text{NH}_4\text{Cl}$  and  $\text{CaCl}_2$ , respectively, saturated with the 1.0 g sample. The zeolite suspension was stirred at room temperature for 30 min and then filtered, and the content trapped in the filter was washed with 1.0 L of deionized water and dried in a drying oven (overnight). The time of contact with the zeolite was set at 30 min.

The dried sample was weighed and stirred (7000 rpm) for 10 min with 100 mL of ammonium chloride solution. An aliquot of 0.5 mL of the supernatant was collected for determination of ammonia absorption ( $q$ ), expressed as ammonia removal per unit mass of the zeolite ( $\text{mgNH}_3\cdot\text{Zg}^{-1}$ ), and calculated according to Eq. (1), where  $C_o$  and  $C_f$  are the initial and final concentrations of ammonia, respectively.  $V$  is the volume (l), and  $m$  is the mass of zeolite used (g) [9].

$$q = \frac{(C_o - C_f) \cdot V}{m} \quad \text{Eq. (1)}$$

For the analysis of the concentration of  $\text{Ca}^{2+}$  ions, an aliquot of the supernatant, formed by 100 mL of calcium chloride, was removed, diluted, filtered and analyzed by ion-exchange chromatography.

The concentration of  $\text{Na}^+$  ions present in the LTA-type zeolite was determined by ICP-OES (inductively coupled plasma optical emission spectrometry). For the measurements of the  $\text{NH}_4^+$  exchange ion, an atomic absorption spectrophotometer (Shimadzu) was used, and units were converted to milliequivalents/gram ( $\text{meq.g}^{-1}$ ).

## b) The density functional theory study

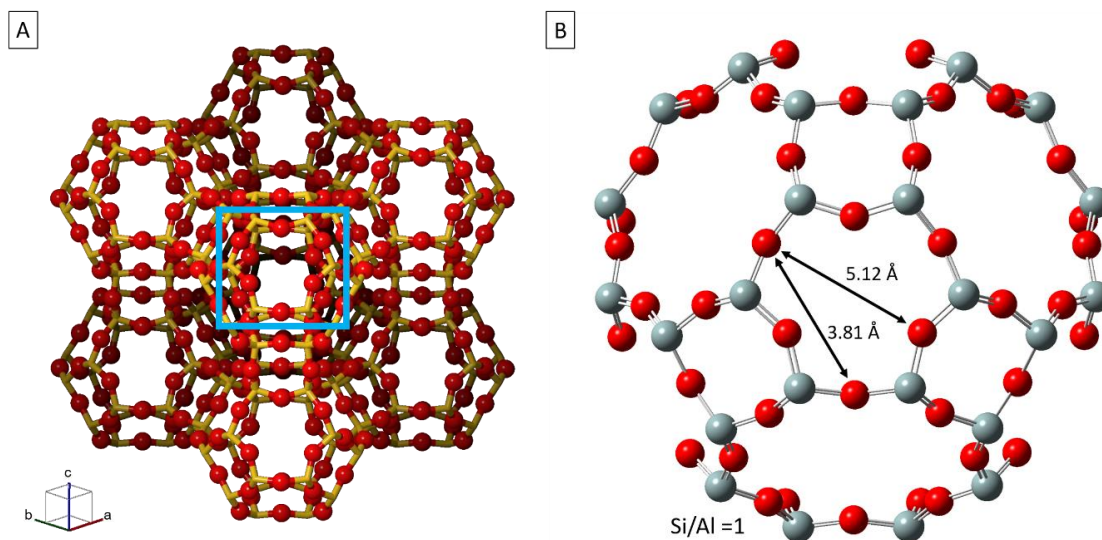
Fig. 1a shows the unit cell obtained in the Database of Zeolite Structures (IZA), with the model drawn in GaussView 5.0.8 software, based on the structure of the minimum mean energy of LTA-type zeolite <sup>[10]</sup>. The number of Al in the LTA-type simulation cell is equal to 24. The conformational isomers for each substituent Na<sup>+</sup>/Al<sup>3+</sup>, NH<sub>4</sub><sup>+</sup>/Al<sup>3+</sup> and Ca<sup>2+</sup>/Al<sup>3+</sup> were analyzed systematically.

The initial proposal was to use the simplest conformation (Fig. 1b) as a guide for the replacement of each Al<sup>3+</sup> ion by a cation (Na<sup>+</sup>, NH<sub>4</sub><sup>+</sup> and Ca<sup>2+</sup>) introduced into the central site or edge, with structural constraints in the "star" form to avoid groups of simultaneous isomers. There was no ordinary conformational analysis of the drawn structures; that is, the three coordinates of the molecule were considered.

The calculations were performed in Gaussian 09W software at the DFT level, with the advantage of including electronic correlation for a good description of complex systems such as zeolites. Functional M06-2X was employed with double the amount of nonlocal exchange (2X), using the valence base of Pople 6-311<sup>++</sup>G(d,p) indicated for kinetic calculations, noncovalent interactions and Rydberg states <sup>[11]</sup>. Frequency calculations should show which conformation has stationary minimum points. The structural geometries allow for the identification of the planarity of the molecules and modifications in the energies of connection with the change in this planarity <sup>[12]</sup>.

A calculation of the atomic loads was performed using the Qeq method for load balancing with the Ewald algorithm to include weak interactions (electrostatic, H-bond and van der Waals forces). To reduce the computational demand and to optimize the time duration in the computation of the calculations, the UKS configuration (spin-polarized calculation using alpha and beta orbitals) was deactivated (UKS-off). This means that the DFT calculations consider the same orbitals for the alpha and beta-paired electrons <sup>[13]</sup>.

Figure 1. Representation of the (a) 3D framework of LTA-type zeolite; (b) Six-membered ring (6MR) together with relevant O–O distances obtained after geometry optimization. The unit cell is represented by a blue line.



Characterization.

Powder XRD patterns of the samples were recorded by a PANalytical X'pert diffractometer with CuK $\alpha$  radiation ( $\lambda=1.54 \text{ \AA}$ ). The relative crystallinity was determined from the peak areas  $2\theta = 7.1^\circ$ ;  $10.1^\circ$ ;  $12.4^\circ$ ;  $16.1^\circ$ ;  $21.6^\circ$ ;  $23.9^\circ$ ;  $27.1^\circ$ ; and  $34.1^\circ$  using highly crystalline LTA (Si/Al molar ratio is 1) as a reference. The morphology of the samples was characterized by field-emission scanning electron microscopy (SEM). FT-IR spectroscopy was used to reveal significant structural differences between the starting material (beta-spodumene) and the LTA-type zeolite formed. The chemical composition was obtained using the AAS method (atomic absorption spectrometer).

## Results and discussion

Recovery of lithium as  $\text{Li}_2\text{CO}_3$ .

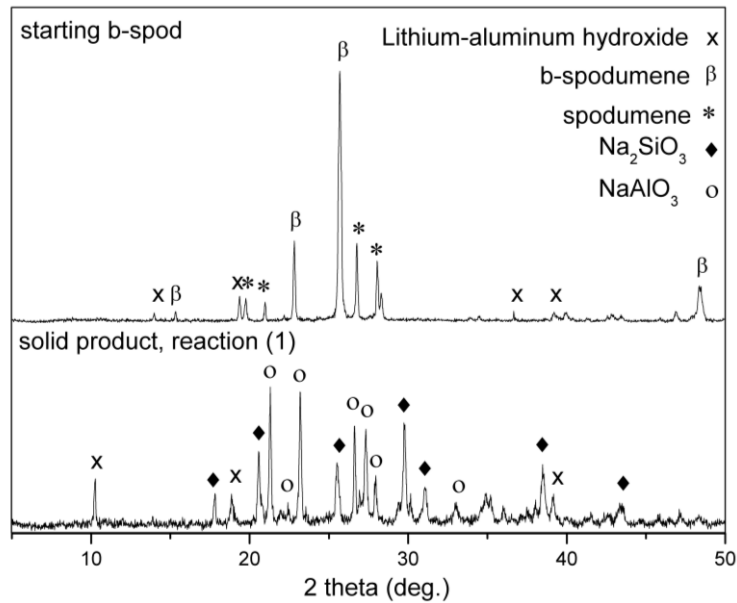
The lithium present in the beta-spodumene is mostly located between the tetrahedra of Si and Al and organized in the absence of channels and cavities of molecular dimension, limiting the access of other molecules to chemical exchange and its extraction from the network <sup>[14]</sup>.

Through the XRD analysis shown in Fig. 2, it is possible to observe the presence of several crystalline phases on the starting beta-spodumene, which is rich in silicon and aluminum. Some of these phases are highly stable, and in such cases, pretreatment by the alkaline fusion extraction method, for example, was carried out to dissolve these phases, providing a greater amount of available silicon and aluminum.

The addition of NaOH provided the presence of a mineralizing agent, enabling the chemoselective ion exchange between  $\text{Li}^+$  of  $\beta\text{-LiAlSi}_2\text{O}_6$  and  $\text{Na}^+$  of  $\text{Na}_2\text{CO}_3$ . The Si and Al species obtained in the mother-liquor after leaching of the mineral were removed as the compounds  $\text{Na}_2\text{SiO}_3$  and  $\text{NaAlO}_3$ , according to reactions (1) and (2), with the XRD patterns shown in Fig. 2.

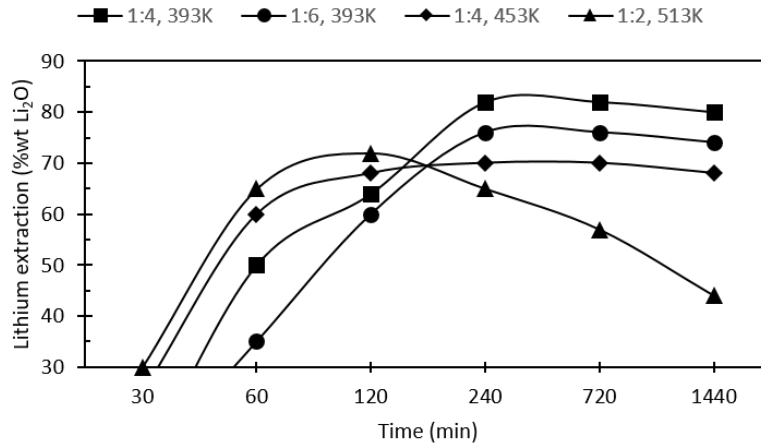


Figure 2. XRD patterns of the solid phases formed by the addition of NaOH.



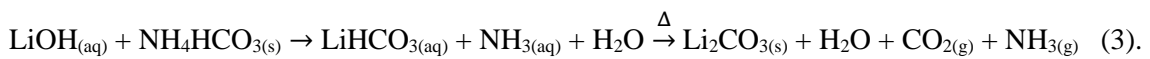
The maximum yield for recovery of the solid phase was obtained for an amount of 7 g NaOH after tests were carried out by varying the amount of NaOH in the leaching liquor, which is necessary for the occurrence of reaction (1). Fig. 3 shows the dependence of time and temperature employed for different  $\text{Li}_2\text{O}:\text{Na}_2\text{CO}_3$  mass ratios.

Figure 3. Solubility kinetics of lithium depending on time, temperature, and  $\text{Li}_2\text{O}:\text{Na}_2\text{CO}_3$  mass ratio.



According to Fig. 3, the dissolution of lithium occurred rapidly for the  $\text{Li}_2\text{O}:\text{Na}_2\text{CO}_3$  mass ratio and was mostly completed within 120 min (72% extracted Li). The extraction percentage was independent of the hydrothermal treatment time after 240 min of reaction, except for the  $\text{Li}_2\text{O}:\text{Na}_2\text{CO}_3$  mass ratio at 513 K. The decrease in temperature from 453 K to 393 K favored an increase in the lithium yield extracted by approximately 10% (240 min).

The extraction of Li from the resulting solution after the precipitation of Al and Si can be carried out by any known method. In this case, the carbonation process was used. Lithium was precipitated from an  $\text{NH}_4\text{HCO}_3$  solution according to reaction (3) [15].



The dissolution rate of  $\text{Li}_2\text{CO}_3$  in the  $\text{NH}_4\text{HCO}_3$ -water system is proportional to the partial pressure of  $\text{CO}_2$  in a closed system and inversely proportional to the increase in solids concentration and the  $\text{Li}_2\text{CO}_3$  particle size [16].

Through reaction (3),  $\text{CO}_2$  can be recovered by heating the  $\text{LiHCO}_3$  solution under vacuum and recirculated. All methods that can improve the dissolution of  $\text{CO}_2$  in the pulp are beneficial to the process. Ambient temperature is recommended because the dissolution of  $\text{Li}_2\text{CO}_3$  decreases with increasing temperature, according to Tab. 2.

Table 2. The solubility of  $\text{Li}_2\text{CO}_3$  in the  $\text{NH}_4\text{HCO}_3$ -water system (g/100 g  $\text{H}_2\text{O}$ ) [17].

Temp. (K)	373	353	333	323	298
Solubility	0.72	0.85	1.01	1.08	1.27

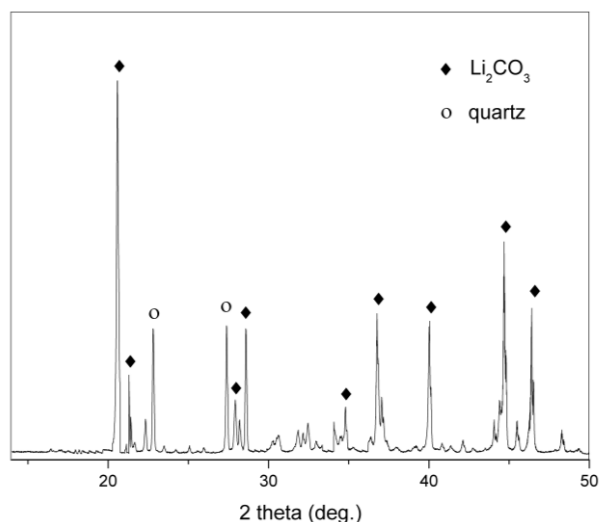
The lithium was recovered as lithium carbonate after heating the solution to  $95^\circ\text{C}$  and the removal of  $\text{H}_2\text{O}$  and  $\text{NH}_3$ . The precipitated lithium carbonate was removed by filtration, washed with water and allowed to dry.

Fig. 4 shows the XRD patterns of the obtained  $\text{Li}_2\text{CO}_3$ , with the precipitate analyzed by AAS (Tab. 3). Gravimetric analysis showed that the recovery of Li as  $\text{Li}_2\text{CO}_3$  was close to 82% ( $\text{Li}_2\text{O}$ , wt%). As a suggestion to increase the lithium content in solution, add  $\text{Li}_2\text{CO}_3$  (10 g Li/L solution) during precipitation to obtain yields greater than 90%  $\text{Li}_2\text{O}$  (wt%).

Table 3. The purity of  $\text{Li}_2\text{CO}_3$ .

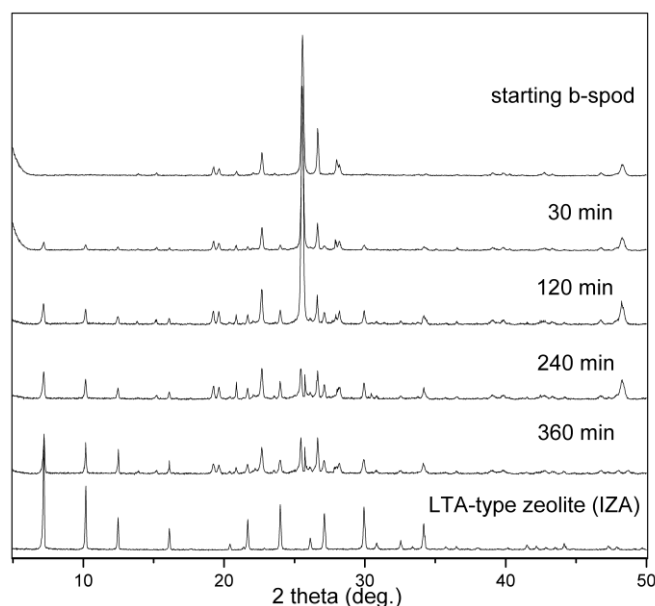
The purity of $\text{Li}_2\text{CO}_3$ (%)	Content of impurities					
	Na	Si	Mg	K	Al	Others
95.4	1.83	1.12	0.88	0.53	0.03	0.21

Figure 4. XRD patterns of the recovered  $\text{Li}_2\text{CO}_3$ .



From the experimental conditions that resulted in a higher yield for lithium extraction, an Al source (sodium aluminate, for example) was added to the mother liquor to form a gel-like Si/Al molar ratio similar to LTA-type zeolite (IZA). Fig. 5 shows the XRD patterns of the obtained materials, and the  $\text{Li}_2\text{O}:8\text{Al}_2\text{O}_3$  molar ratio is correlated to the period of autoclaving.

Figure 5. XRD patterns of products obtained from hydrothermal treatment.



The product formed after hydrothermal treatment for 360 min showed no impurities related to the sodalite and analcime phases ( $2\theta = 13.9^\circ, 19.8^\circ, 28.1^\circ$  and  $31.5^\circ$ ), confirming efficient dissolution of the  $\text{Na}_2\text{SiO}_3$  and  $\text{NaAlO}_3$  species present in the mother liquor from excess  $\text{NaOH}$  in the reaction medium for higher crystallization periods. The products obtained after treatment for 120 min and 240 min showed low-intensity  $2\theta = 7.02^\circ, 10.13^\circ, 12.21^\circ$  and  $16.44^\circ$  reflections, indicating that although the Si/Al ratio was adjusted, it was not possible to obtain a pure zeolite phase.

The addition of aluminate created an excess of Al since the quartz was not dissolved under the initial treatment conditions. Through this mechanism, a gel layer was formed in the support after aging in situ that was abundant in zeolitic aqueous nuclei. After an appropriate period of crystallization, the amorphous particles were transformed into zeolite crystals. This growth by propagation acts subsequent or in parallel to the agglomeration and densification of the primary particles, as observed for the 360 min reaction.

The low-temperature conditions employed in the hydrothermal treatment (368 K) and leaching ( $298 \text{ K} < T < 303 \text{ K}$ ) stages were important not only to permit the growth of the crystals but also to avoid the formation of competing phases such as SOD- or GIS-type <sup>[18]</sup>.

The degree of crystallinity (DC) was calculated by comparing the intensities (or inclusion of all intensities) of the reflection of the formed material and the standard sample (IZA) for  $2\theta = 7.18^\circ, 10.16^\circ, 12.49^\circ, 16.11^\circ, 21.68^\circ, 23.98^\circ, 27.10^\circ$  and  $34.18^\circ$  [18]. The sum of the eight intensities of the  $2\theta$  reflections was used to obtain the crystallinity of the synthesized samples, according to Eq. (2), detailed in Tab. 4.

$$DC = \frac{\sum_1^8 \text{Peak intensities of the investigated sample}}{\sum_1^8 \text{Peak Intensities of the reference sample}} \quad \text{Eq. (2)}$$

Table 4. The degree of crystallinity by XRD based on the relative intensity of specific peaks.

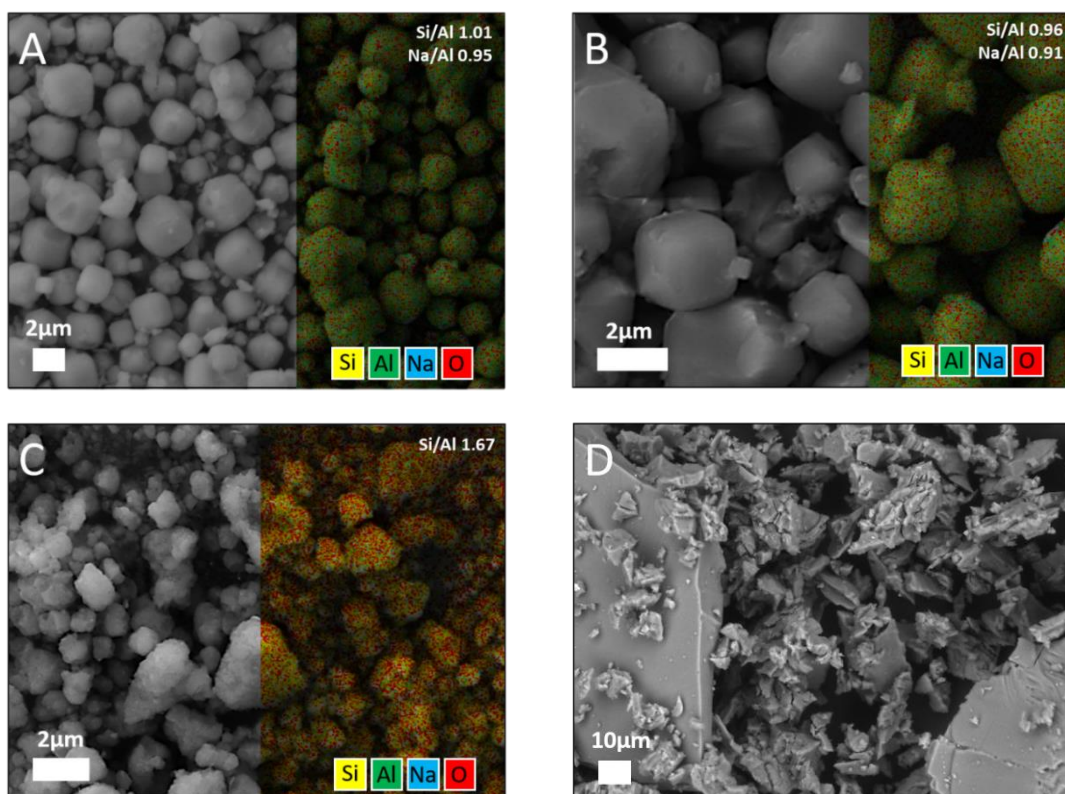
reference	360 min	240 min	120 min	30 min
LTA-type zeolite (IZA)	0.89	0.76	0.56	0.44

The peaks of a diffractogram are affected by the size of the particles. The full width at half maximum (FWHM) is inversely proportional to the crystallite size (Fig. 6). Since the peak area (integral intensity) must be preserved and the FWHM is reduced with increasing crystallite size, the result is a proportional increase in peak intensity to keep the area constant.

Another factor that may have influenced the similarity between the diffractograms in Fig. 5 and the discrepancy of the degree of crystallinity in Tab. 4 may be related to the configuration of the diffractometer.

Fig. 6 shows the SEM and EDS layered images for the LTA-type zeolite crystals obtained from irregular beta-spodumene particles. The sample in Fig. 6a presented cubic morphology with spherical facets, typical for LTA-type zeolite, showing that a certain equilibrium between the rates of dissolution and crystallization of the material was reached for a treatment of 360 min. In the other cases (Figs. 6b and 6c), the crystals presented irregular morphology deposited under quartz crystal, indicating that the synthesis conditions were mild.

Figure 6. SEM and EDS layered images of samples synthesized in a) 360 min; b) 240 min; c) 30 min. d) beta-spodumene.

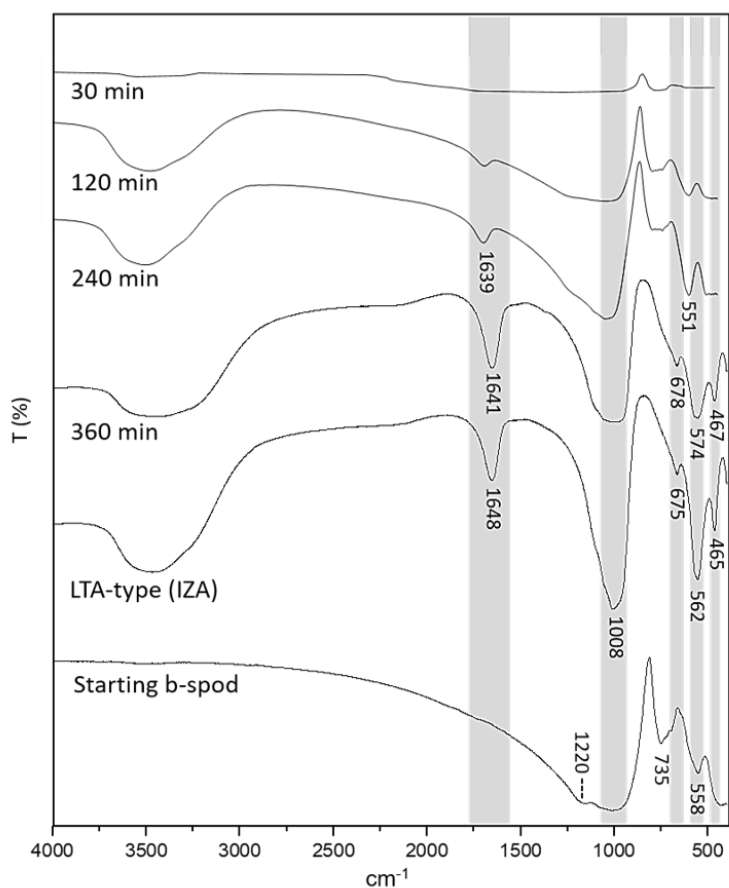


The transformation of beta-spodumene into LTA-type zeolite can be confirmed by the IR spectra in the  $4000\text{-}400\text{ cm}^{-1}$  region (Fig. 7). Structural differences were observed in the bands at approximately  $1000\text{ cm}^{-1}$ , characteristic of the Si-O-Al bond of the tetrahedral  $\text{TO}_4$  of primary building units; bands at  $675\text{ cm}^{-1}$ ,  $562\text{ cm}^{-1}$ , and  $465\text{ cm}^{-1}$  indicate the crystallinity of an LTA-type zeolite; the band at  $678\text{ cm}^{-1}$  indicates typical symmetrical stretches of primary internal T-O vibrations (T = Si, Al) <sup>[19]</sup>.

The conversion to LTA-type zeolite eliminated some of these bands, leaving a wide asymmetric range at  $1220\text{ cm}^{-1}$  as the main feature. Changes in the Si-O elongation bands and the disappearance of the Si-O-Al band at  $735\text{ cm}^{-1}$  are consistent with distortion of the tetrahedral and octahedral layers <sup>[19]</sup>.

The band at approximately  $570\text{ cm}^{-1}$  is associated with the vibration of the  $\text{TO}_4$  double ring (D4R), predominant in the secondary building unit for LTA-type zeolite. Bands with maximum vibrations of  $3500\text{ cm}^{-1}$  and  $1650\text{ cm}^{-1}$ , typical of -OH functional groups, are attributed to water of a zeolitic nature <sup>[19]</sup>.

Figure 7. FT-IR spectra of LTA samples synthesized for different times.



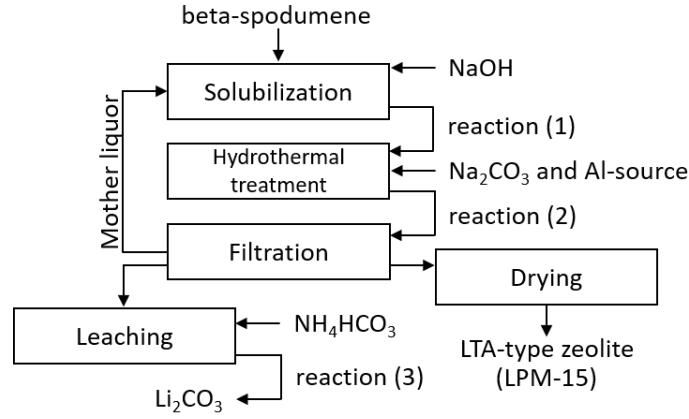
Based on the interpretation of the spectra of the theoretical D6R units (experimental LTA), the vibrations of the following bands can be assigned according to Tab. 5 [20].

Table 5. Different structural groups from the FT-IR study of LTA (D6R) zeolites.

Wavenumber ( $\text{cm}^{-1}$ )	Denotation
1008	Asymmetric stretching vibrations of bridge bonds – $\nu_{\text{as}}$ Si-O(Si) and $\nu_{\text{as}}$ Si-O(Al).
675	Symmetric stretching vibrations of bridge bonds – $\nu_{\text{s}}$ Si-O-Si and $\nu_{\text{s}}$ Si-O-Al.
562	Symmetric stretching vibrations of bridge bonds – $\nu_{\text{s}}$ Si-O-Si and bending vibrations – $\delta$ O-Si-O.
465	Bending vibrations – $\delta$ O-Si-O, occurring in “antiphase”, and $\delta$ O-Al-O.

Therefore, the diagram of the procedure is shown in Fig. 8. The synthesized LTA-type zeolite was named LPM-15.

Figure 8. Process diagram for lithium extraction and LTA-type zeolite synthesis.



Cation-exchange capacities.

Tab. 6 presents the results for the CEC of materials with zeolite characteristics obtained at different times of hydrothermal treatment, according to the synthesis conditions presented and compared with the synthesized NaP1 and 4A zeolites, with CEC for ammonium ( $\text{NH}_4^+$ ) and calcium ions ( $\text{Ca}^{2+}$ ).

Table 6. Synthesis conditions for CEC tests compared with NaP1 and 4A zeolites.

Samples	synthesis							yield		CEC <sub>(NH<sub>4</sub><sup>+</sup>)</sub>	CEC <sub>(Ca<sup>2+</sup>)</sub>
	solubilization		hydrothermal treatment				leaching	Li <sub>2</sub> CO <sub>3</sub>	zeolite		
	b-spod	NaOH	Na <sub>2</sub> CO <sub>3</sub>	NaOH <sup>(i)</sup>	NaAlO <sub>2</sub>	time <sup>(ii)</sup>	NH <sub>4</sub> HCO <sub>3</sub>				
	g	mol.L <sup>-1</sup>	g	mol.L <sup>-1</sup>	mol.L <sup>-1</sup>	min	mol.L <sup>-1</sup>	%Li <sub>2</sub> O	% <sup>(iv)</sup>	meq <sub>NH<sub>4</sub>Cl</sub> ·g <sup>-1</sup>	meq <sub>CaCl<sub>2</sub></sub> ·g <sup>-1</sup>
1	6.0	0.22	1.6	3.3	30	30	0.16	18	25	0.3	2.0
2	6.0	0.22	1.6	3.3	30	240	0.16	82	42	0.8	3.6
3 (LPM-15)	6.0	0.22	1.6	3.3	30	360	0.16	77	73	2.2	4.1
NaP1 <sup>(iii)</sup>	–	3.0	–	–	–	240	–	–	–	2.5	–
4 A <sup>(iii)</sup>	–	3.0	–	–	–	240	–	–	–	–	4.5

i= recirculated mother liquor; ii= 368 K/autoclave; iii= synthesis based on IZA; iv= [g<sub>(synthesized)</sub>/g<sub>(zeolite IZA)</sub>].

The CEC result for synthesized NaP1 zeolite was  $2.5 \text{ meqNH}_4^+ \cdot \text{g}^{-1}$ , compatible with the literature ( $2.5\text{-}4.0 \text{ meq.g}^{-1}$ ) [21]. The zeolites synthesized for 30 min, 120 min and 360 min showed CECs of 0.3, 0.8 and  $2.2 \text{ meq.g}^{-1}$ , respectively. Larger reaction periods favored the dissolution of the vitreous matrix and quartz. Reduction of the reaction time was obtained using materials with higher content of impurities (mullite and quartz) or undesirable phases (sodalite and analcime).

The CEC of the synthesized 4A zeolite was  $4.5 \text{ meqCa}^{2+} \cdot \text{g}^{-1}$ , lower than that found in the literature ( $5.4 \text{ meq.g}^{-1}$ ) [21]. The CEC tests presented values of 2.0, 3.6 and  $4.1 \text{ meq.g}^{-1}$  to calcium in the 30, 240 and 360 min reaction periods, respectively. The latter value is satisfactory in obtaining a product with high added value for the detergent industry, and quite significant when compared directly with the synthesized 4A zeolite, confirming the viability of the synthesis in the procedure for the extraction of lithium from beta-spodumene.

DFT study of  $x/\text{Al}^{3+}$  substitution in LPM-15 ( $x = \text{Na}^+, \text{NH}_4^+$  or  $\text{Ca}^{2+}$ ).

In the  $\text{Na}^+/\text{Al}^{3+}$  exchange, the positions of the extra structural cations were studied to compare the relative energies of the respective geometries (center or edge). As shown in Tab. 7, the most stable position of the  $\text{Na}^+$  cation was with the exchange in the center position, close to  $\text{O}^{2-}$ , due to the ionic attraction forces (Fig. 9).

Unlike if we had extrastructural hydrogen ( $\text{H}^+$ ), the tendency would be to remain close to the oxygen atoms in the LPM-15 for the formation of O-H bonds, preferably at the edges (energetically more stable). The effective ionic radius of sodium was  $1.07 \text{ \AA}$ . Energy values were converted from Hartree to electron-volt (eV) and  $\text{kJ.mol}^{-1}$  ( $1 \text{ Hartree} = 27.2 \text{ eV} = 2,630 \text{ kJ.mol}^{-1}$ ).

According to Tab. 7, the substitutions were proportional to the accessible pore volume, showing that as larger cations were introduced into the LPM-15,  $\text{Na}^+$  and  $\text{Ca}^{2+}$  occupied more physical space, shrinking the internal volume of the zeolite and resulting in repulsive forces greater than the forces of attraction exerted by  $\text{O}^{2-}$  repelling  $\text{Na}^+$  toward the center of the unit cell.

Table 7. Effect of  $x/\text{Al}^{3+}$  ( $x = \text{Na}^+$ ,  $\text{NH}_4^+$  or  $\text{Ca}^{2+}$ ) substitutions on the zeolite LPM-15 geometry.

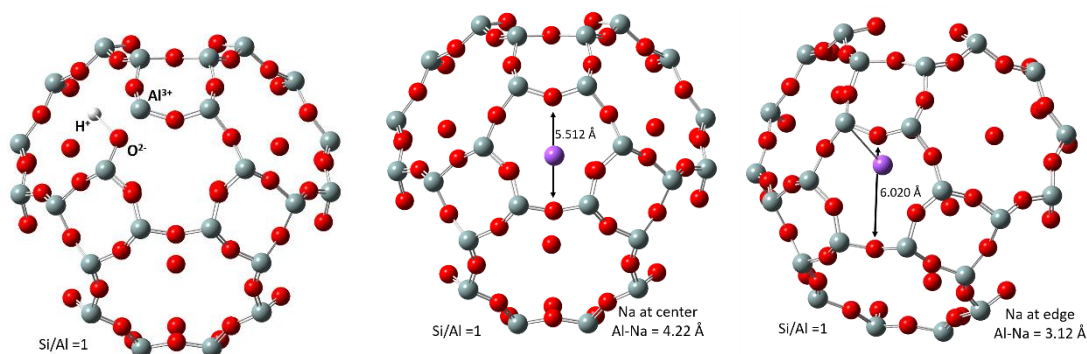
$x/\text{Al}^{3+}$	RPCS <sup>(i)</sup>	LP <sup>(ii)</sup>	APV <sup>(iii)</sup>	POD <sup>(iv)</sup>	E <sup>(v)</sup>	$\Delta E$ <sup>(vi)</sup>
$x = \text{Na}^+$	Center	10.7	688.6	5.5	< 0.01	77.5
	Edge	12.8	695.1	6.0	0.04	101.2
$x = \text{NH}_4^+$	Center	11.9	3,338.7	10.7	< 0.01	106.1
	Edge	11.7	2,338.7	9.8	0.25	307.3
$x = \text{Ca}^{2+}$	Center	11.9	876.2	5.8	< 0.01	115.4
	Edge	12.0	863.3	5.9	0.14	188.5

i= Relative Position of Cations in the Structure; ii= Lattice Parameter ( $\text{\AA}$ );

iii= Accessible Pore Volume ( $\text{\AA}^3$ ); iv= Pore Opening Diameter ( $\text{\AA}$ );

v= absolute energies in Hartrees; vi= relative energies between the isomers ( $\text{kJ}\cdot\text{mol}^{-1}$ ).

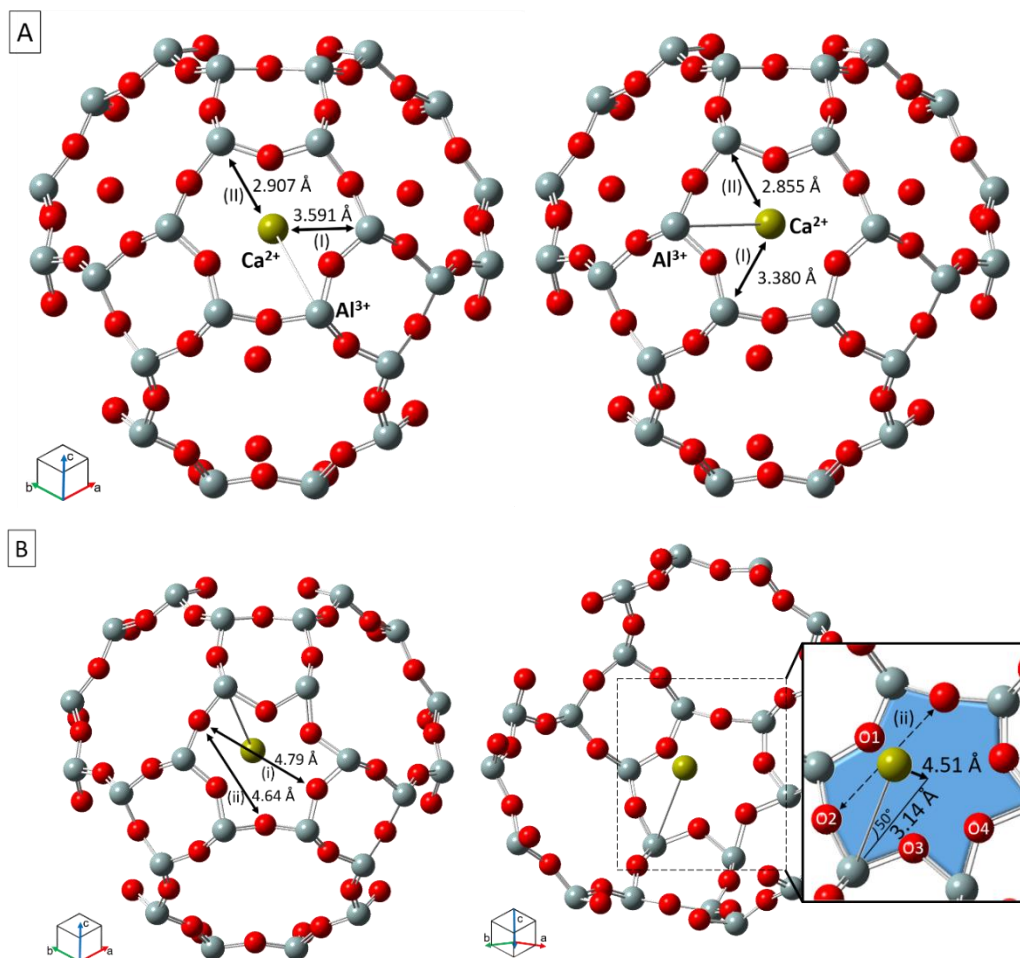
Figure 9.  $\text{Na}^+/\text{Al}^{3+}$  and  $\text{H}^+/\text{Al}^{3+}$  substitutions showing the positions of cations in a simulated final geometry for  $\text{Na}^+$  at  $\text{Si}/\text{Al} = 1$ .



The attraction force exerted by the six  $\text{O}^{2-}$  ions around the  $\text{Ca}^{2+}$  ion contributed to a greater stability in the Ca-center configuration (Fig. 10a).

In the Ca-edge configuration (Fig. 10b), the attractive effect of only four of these ions (O1, O2, O3 and O4) distorted the network with the decrease of the O-O interatomic distances, resulting in Ca-ring repulsive interference ( $\Delta\text{length} = 4.51 \text{ \AA}$ ), justifying the energy increase observed in Tab. 7 ( $\Delta E$ ) compared to the Na-center and Na-edge configurations. An increase in the net parameter ( $a^3$ ) may reduce the probability of repulsion between the rings. However, volume expansion may lead to an increase in accessible pore volume.

Figure 10. Simulated geometries with  $\text{Ca}^{2+}$  near the ring: (a) center-position; (b) edge-position. Ca-Al and O-O distances were labeled as (I) or (II) and (i) or (ii), respectively.



Considering the Al-Na bonding distance, we can observe the influence of the position of the substituents. Groups such as methyl and ethyl, for example, would suffer greater repulsions because they are bulky. When comparing the pore opening diameter between oxygen atoms, the distance to the Na center was  $5.512 \text{ \AA}$  vs  $6.020 \text{ \AA}$  to the Na edge.

The similarity in the values for pore volume accessible between  $\text{Na}^+$  and  $\text{Ca}^{2+}$  is justified by the similarity between the ionic radii of these species ( $1.02 \text{ \AA}$  and  $1.0 \text{ \AA}$ , respectively). In the computer simulation, the difference was UKS-off; that is, the "star" symmetry did not use all available orbitals, limiting the interaction effect of the electrons present.

The column identified in relative energies represents the most stable geometry whose substitution is preferred. The stability sequence of the isomers of the first series of substitutions (center) was  $\text{Na}^+ > \text{NH}_4^+ > \text{Ca}^{2+}$ . In the second series (edge), the order of stability was  $\text{Na}^+ > \text{Ca}^{2+} > \text{NH}_4^+$ .

According to R. Astala et al. (2004), an ion exchange between  $\text{Na}^+$  and  $\text{Ca}^{2+}$  is normally observed in the process of hard water softening. The values in Tab. 7 indicate that if LPM-15- $\text{Na}^+$  was placed in contact with water containing calcium, the ion exchange would render the pore less accessible as the pore opening diameter shrunk (6.045 Å to 5.903 Å), showing that calcium was replaced by sodium, concluding the slowing process [22].

In the  $\text{NH}_4^+/\text{Al}^{3+}$  change, the interaction of the ammonium ion was extremely strong due to the auxiliary aluminum in the formation of hydrogen bonds between the oxygen of the Si-O-Al bond, which acts as a Lewis acid, and hydrogen of the  $\text{NH}_4^+$  ion, by which the other hydrogen atoms belonging to the ion are stabilized by the confinement effect caused by the oxygen atoms of the LPM-15 crystalline lattice [23].

This action can establish an acidic character to the material due to the formation of surface hydroxyl groups (Brønsted acid sites), originating in the absence of adsorptive affinity between  $\text{NH}_3$  and Lewis acid sites, which are unable to form strong hydrogen bonds, resulting in the formation of active sites in zeolite pentasil units, while generating computational data with the preferred  $\text{H}^+/\text{Al}^{3+}$  change location: center (relative energy: center < edge position) [23].

Simulations with simultaneous  $x/\text{Al}^{3+}$  ( $x = \text{Na}^+, \text{NH}_4^+$  or  $\text{Ca}^{2+}$ ) substitutions were not performed since the placement of more than one extrastructural cation would compromise the stability of LPM-15, decreasing the Si/Al molar ratio. According to the Lowenstein rule, Al-O-Al bonds are prohibited in a zeolite structure. Therefore, the minimum ratio of Si/Al for cationic aluminum substitution is 1. For a single cell of LTA-type zeolite with 24 Si atoms, when there is no cation substitution, the Si/Al molar ratio is  $24/0 = \infty$  [19].

Lima et al. (2008) studied the interference of these cations in the retention of the  $\text{NH}_4^+$  ion in residual water. The retention sequence was  $\text{Na}^+ > \text{Ca}^{2+}$ , with  $\text{Na}^+$  highly adsorbed, although they have a similar ionic radius. The influence of the  $\text{Ca}^{2+}$  ion on the retention of the  $\text{NH}_4^+$  ion was very small, in accordance with the preferred series of cation adsorption in the zeolite structure [24].

## Conclusions

In the synthesis of zeolites, the closer to the Si/Al ratio of the feedstock, the fewer pretreatment steps that are required. The compounds present in the chemical composition of beta-spodumene at very low mass percentages did not have a significant influence on the final composition of the zeolites.

For longer crystallization times, more material becomes stable, and consequently, particles in the structure become smaller, resulting in pores and channels with smaller diameters. The obtained zeolite exhibited the formation of a homogeneous structure, with zeolite NaP1 being the exclusive phase and quartz being an impurity, which is undesirable residue that can be separated from the material by decantation or flotation.

Extraction was strongly influenced by reaction time. The solubilization and precipitation rates presented two behaviors: (i) to 120 min, with  $\text{Li}_2\text{CO}_3$  precipitation proportional to the temperature and inversely proportional to the  $\text{Li}_2\text{O}:\text{Na}_2\text{CO}_3$  mass ratio; and (ii) after 240 min, with the extraction percentage slightly proportional to the  $\text{Li}_2\text{O}:\text{Na}_2\text{CO}_3$  mass ratio after reduction of temperature.

Conversion to  $\text{Li}_2\text{CO}_3$  occurred without calcination and showed an extraction yield of greater than 80% Li after 240 min of solubilization. The dissolution occurred for the  $\text{Li}_2\text{O}:4\text{Na}_2\text{CO}_3$  mass ratio at 393 K. This result shows that the residual lithium is embedded in the zeolite structure, likely as a compensation cation, in cavities interconnected with molecular dimensions where compensation cations allow ion exchange.

Therefore, with the optimization of the process, it was possible to simultaneously obtain LTA-type zeolite (LPM-15) with the addition of excess NaOH in the mother liquor that was recirculated ( $3\text{Li}_2\text{O}:35\text{NaOH}$  mass ratio) for a reaction of 360 min at 368 K.

The CEC values indicate that the LPM-15 zeolite has good adsorption characteristics, as an alternative for the treatment of effluents, with physical properties equivalent to the zeolites synthesized in pressurized reactors under a higher reaction temperature [25].

From the modeling structure calculations, the geometric and electronic parameters pointed to a stabilization in the LPM-15 structure around the cationic  $\text{Na}^+/\text{Al}^{3+}$  exchange, showing planarity, the result of the lower effect of repulsion compared to the other substituents. The data presented for the geometric parameters "accessible pore

volume" and "pore opening diameter" are expected to provide theoretical support for research on the LPM-15 structure and its application in water purification processes, catalytic cracking, and biofuel production.

### Acknowledgments

This study was financed in part by the Coordenação de Aperfeiçoamento de Pessoal de Nível Superior - Brazil (CAPES) - finance code 001. The authors would like to thank Companhia Brasileira de Lítio - Brazil (CBL), for the beta-spodumene samples and the Instituto de Tecnología Química - Spain (ITQ), for the characterization of the materials.

### References

- [1] GRUBER, P. W., MEDINA, P. A., KEOLEIAN, G. A., KESLER, S. E., EVERSON, M. P., & WALLINGTON, T. J.; Global lithium availability: A constraint for electric vehicles?. **J. Ind. Ecol.**, 15.5 (2011), p. 760-775.
- [2] TAPIA-DIAZ, J. D.; **Lithium-extraction method for obtaining lithium carbonate from a brine or ore and/or clay pretreated in order to be boron-free.** WO Patent No 2013,049952,A1. 2013.
- [3] XIANG, W., LIANG, S., ZHOU, Z., QIN, W., & FEI, W.; Extraction of lithium from salt lake brine containing borate anion and high concentration of magnesium. **Hydrometallurgy**, 166 (2016), p. 9-15.
- [4] OLIVEIRA, M. S. M., NASCIMENTO, R. M., PERGHER, S. B. C.; **Síntese do material zeolítico LPM-11 de tipologia MOR a partir do resíduo silicoaluminoso gerado na extração do lítio do espodumênio.** BR Patent No 10,2017,016712,7. 2017.
- [5] OLIVEIRA, M. S. M., NASCIMENTO, R. M., PERGHER, S. B. C.; **Síntese do material zeolítico LPM-12 de tipologia EDI a partir do resíduo silicoaluminoso gerado na extração do lítio do espodumênio.** BR Patent No 10,2017,016757,7. 2017.
- [6] DAVIS, M. E.; Zeolites from a materials chemistry perspective. **Chemistry of Materials**, 26.1 (2013), p. 239-245.
- [7] DAVIS, M. E., & LOBO, R. F.; Zeolite and molecular sieve synthesis. **Chemistry of Materials**, 4.4 (1992), p. 756-768.

- [8] BIESEKI, L., MELO, V. R. M., V SOBRINHO, E., MELO, D. M. A., & PERGHER, S. B. C.; Extraction of lithium from  $\beta$ -spodumene sample. **Cerâmica**, 59.352 (2013), p. 557-562.
- [9] CARDOSO, A. M., HORN, M. B., FERRET, L. S., AZEVEDO, C. M., & PIRES, M.; Integrated synthesis of zeolites 4A and Na-P1 using coal fly ash for application in the formulation of detergents and swine wastewater treatment. **J. Hazard. Mater.**, 287 (2015), p. 69-77.
- [10] BAERLOCHIER, C., & MCCUSKER, L. B.; International Zeolite Association. Database of Zeolite Structures. <<http://www.iza-structure.org/databases/>>, 2017. Accessed on: March 21, 2018.
- [11] PARR, R. G., & YANG, W.; **Density-functional theory of atoms and molecules**, New York, Oxford University press. 1989.
- [12] VAN SPEYBROECK, V., HEMELSOET, K., JOOS, L., WAROQUIER, M., BELL, R. G., & CATLOW, C. R. A.; Advances in theory and their application within the field of zeolite chemistry. **Chem. Soc. Rev.**, 44.20 (2015), p. 7044-7111.
- [13] JOHN, M., ALEXOPOULOS, K., REYNIERS, M. F., & MARIN, G. B.; Reaction path analysis for 1-butanol dehydration in H-ZSM-5 zeolite: Ab initio and microkinetic modeling. **Journal of Catalysis**, 330 (2015), p. 28-45.
- [14] BERGER, A., BOLDYREV, V., & MENZHERES, L.; Mechanical activation of  $\beta$ -spodumene. **Mater. Chem. Phys.**, 25.4 (1990), p. 339-350.
- [15] AN, J. W., KANG, D. J., TRAN, K. T., KIM, M. J., LIM, T., & TRAN, T.; Recovery of lithium from Uyuni salar brine. **Hydrometallurgy**, 117 (2012), p. 64-70.
- [16] YI, W. T., YAN, C. Y., & MA, P. H.; Kinetic study on carbonation of crude  $\text{Li}_2\text{CO}_3$  with  $\text{CO}_2$ -water solutions in a slurry bubble column reactor. **Korean J. Chem. Eng.**, 28.3 (2011), p. 703-709.
- [17] ROBERT, C. W.; **Handbook of chemistry and physics** (55<sup>th</sup> ed.), CRC Press. 1975.
- [18] MINTOVA, S., & BARRIER, N.; **Verified synthesis of zeolitic materials** (3rd ed.), Elsevier. 2016.
- [19] SZOSTAK, R.; **Molecular sieves: principles of synthesis and identification**, New York: Van Nostrand Reinhold. 1989.

- [20] MOZGAWA, W., JASTRZEBSKI, W., & HANDKE, M.; Vibrational spectra of D4R and D6R structural units. **J. Mol. Struct.**, 744 (2005), p. 663-670.
- [21] CARDOSO, A. M., PAPROCKI, A., FERRET, L. S., AZEVEDO, C. M., & PIRES, M.; Synthesis of zeolite Na-P1 under mild conditions using Brazilian coal fly ash and its application in wastewater treatment. **Fuel**, 139 (2015), p. 59-67.
- [22] ASTALA, R., AUERBACH, S. M., & MONSON, P. A.; Density functional theory study of silica zeolite structures: stabilities and mechanical properties of SOD, LTA, CHA, MOR, and MFI. **J. Phys. Chem. B**, 108.26 (2004), p. 9208-9215.
- [23] ALMUTAIRI, S. M., MEZARI, B., FILONENKO, G. A., MAGUSIN, P. C., RIGUTTO, M. S., PIDKO, E. A., & HENSEN, E. J.; Influence of extraframework aluminum on the brønsted acidity and catalytic reactivity of faujasite zeolite. **Chem. Cat. Chem.**, 5.2 (2013), p. 452-466.
- [24] de LIMA, R. M. G., WILDHAGEN, G. R. D. S., & DA CUNHA, J. W. S. D.; Remoção do íon amônio de águas produzidas na exploração de petróleo em áreas offshore por adsorção em clinoptilolita. **Química Nova**, 31.5 (2008), p. 1237-1242.
- [25] FERRARINI, S. F., CARDOSO, A. M., PAPROCKI, A., & PIRES, M.; Integrated synthesis of zeolites using coal fly ash: element distribution in the products, washing waters and effluent. **J. Braz. Chem. Soc.**, 27.11 (2016), p. 2034-2045.

## Chapter 5. Li<sub>2</sub>O:Na<sub>2</sub>CO<sub>3</sub>:NaCl system calcination: a kinetic study of the conversion to lithium salt

---

Leonardo L. dos Santos<sup>1</sup>; Rubens M. do Nascimento<sup>1</sup>; Sibeles B. C. Pergher<sup>2</sup>

<sup>1</sup> Department of Materials Science and Engineering, Federal University of Rio Grande do Norte, Natal 59078-97, Brazil.

<sup>2</sup> Department of Chemistry, Laboratório de Peneiras Moleculares, Federal University of Rio Grande do Norte, Natal 59078-97, Brazil.

**Abstract:** A kinetic model of the calcination reaction between beta-spodumene and alkaline salts was developed. The parameters affecting the kinetics were investigated. The influences of the temperature, rate of heating and reaction time were evaluated to determine the conversion kinetics to lithium salt (Li<sub>2</sub>CO<sub>3</sub>) in addition to exploring the solid-solid molar ratio closest to the ideal one reported in the literature. The results indicate that the best Li<sub>2</sub>O:Na<sub>2</sub>CO<sub>3</sub> molar ratio is 3:1 + 5% w/w NaCl for the conversion to Li<sub>2</sub>CO<sub>3</sub>, with 70% recovered lithium. The conversion range is maximum over the range of 823-923 K with a calcination cycle of 120 min. Scanning Electron Microscopy (SEM), also known as SEM analysis or SEM microscopy, of the products for which the conversion was < 50% indicates a selective attack at certain locations of the particle. Treatment of the experimental data was performed using the Modelado software. The model that best represents the decomposition of beta-spodumene in the calcination reaction with the Na<sub>2</sub>CO<sub>3</sub> + NaCl mixture, with the highest yield of conversion to Li<sub>2</sub>CO<sub>3</sub>, is:  $\ln(1-X) = -b_1[\ln(1+b_2t) - b_2t/(1+b_2t)]$ . This model was adjusted based on the theory of "nucleation and crystal growth".

**Keywords:** Lithium. Beta-spodumene. Calcination. Kinetics. Carbonate.

### Introduction

Metal extraction processes are directly related to the rates of the chemical reactions involved. In hydrometallurgical processes, the working temperatures are less than those used in pyrometallurgical processes, which implies that reaction rates are lower and that the limitations found in these processes are mainly kinetic <sup>[1]</sup>.

Therefore, for the elaboration of kinetic models describing the mechanisms of the conversion and formation of lithium salts – in particular, for lithium extraction, the ion exchange reaction between  $\text{Li}^+$  of beta-spodumene ( $\beta\text{-LiAlSi}_2\text{O}_6$ ) and  $\text{Na}^+$  ( $\text{Na}_2\text{CO}_3$  and  $\text{NaCl}$ ) – it is of particular importance to know the parameters involved in the calcination reaction [2].

Lithium is a highly required metal throughout the world, mainly because it is known as the lighter metal, with fascinating electrochemical reactivity. As for its metallurgy, lithium can be found in nature as rock ore or in brine [3].

Spodumene, a double lithium aluminum silicate, is the largest natural lithium carrier, containing up to 4% of the metal (5% to 9%  $\text{Li}_2\text{O}$ ), and the monoclinic structure of the pyroxene type imposes a resistance to the attack of chemical agents, gaseous or liquidous. Spodumene turns into its  $\beta$  (beta) phase after pyrometallurgical treatment at 1273 K, and this phase is substantially more reactive and less resistant to alkaline salts [4].

The most common industrial processes for the extraction of lithium from spodumene and the conversion to the corresponding salts are acid digestion, alkaline treatment, and ionic exchange. The main products obtained by these methods are lithium carbonate, hydroxide and chloride, respectively [4].

Acid digestion is carried out with concentrated sulfuric acid at temperatures above 523 K, while alkaline digestion is performed with  $\text{CaCO}_3$  and  $\text{MgCO}_3$  at 1313 K. However, these methods have intrinsic drawbacks such as high levels of sulfate ions and heavy metals in the final concentrate, requiring a sophisticated process for eliminating sodium sulfate and high energy consumption [5, 6].

In addition, from the acidic methodology, 0.95 t of acid residue is generated for each ton of processed ore; this indicates that only Li is recovered from beta-spodumene, and Al and Si remain as residues. In Brazil, only the acid route is used on an industrial scale, and lithium carbonate is the product of greater demand [7].

In the ion exchange process, beta-spodumene is heated in the presence of organic sodium and potassium salts at 673 K. The obtained lithium compounds are usually associated with calcium, magnesium and other elements as impurities, which increase the use of organic solvents and/or the actinide base for purification [6, 7].

The strategy to reduce these resources involves adjusting the calcination parameters, aligning them with those of the alkaline treatment of the reactants. The use of alkaline processing for the recovery of lithium contained in beta-spodumene is an alternative that should provide advantages, since in the tetragonal (beta) configuration, it

is easier to extract lithium with a thermal-chemoselective attack <sup>[8]</sup>.

Relevant studies show the dissolution of beta-spodumene in an autoclave with  $\text{Na}_2\text{CO}_3$  at temperatures near 823 K with a conversion efficiency of less than 60% of that of the corresponding salt, e.g., chloride salt. Other recently used routes are the pyrometallurgical chlorination of beta-spodumene with NaCl and calcination with  $\text{Na}_2\text{CO}_3$  at temperatures between 1173-1373 K <sup>[8, 9]</sup>.

Therefore, the objective of this work was to evaluate the calcination step in the lithium extraction process and to elaborate a kinetic model that best fits the reaction between beta-spodumene and the salts  $\text{Na}_2\text{CO}_3$  and NaCl in the conversion to  $\text{Li}_2\text{CO}_3$ , in an attempt to explain the mechanism of calcination (the nature and rate of the reaction dependent on variables such as time, temperature and velocity). From the model, you can reduce and balance processing costs.

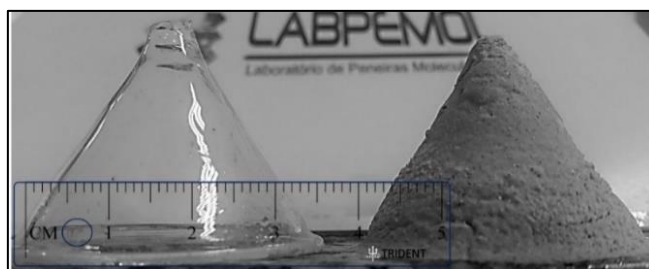
## Experimental

To promote the solid-solid reaction in a muffle furnace that would result in a higher percentage of lithium extracted in the  $\text{Li}_2\text{CO}_3$  form, different mass proportions of  $\text{Li}_2\text{O}:\text{Na}_2\text{CO}_3$  (1:1, 2:1, 3:1, 4:1 and 5:1) were studied with the addition of 5% w/w NaCl.

The mixtures were placed in alumina crucibles and subjected to a calcination heat treatment, using temperatures between 673 K and 1073 K in 50 K intervals, with a thermal cycle duration of 30-300 min in 30 min intervals and heating at a rate of 5 or 50°C/min.

The calcination parameters (heating rate and final temperature) were evaluated using the simple refractoriness test by comparison of equivalent pyrometric cones (Fig. 1) for the mixtures of spodumene,  $\text{Na}_2\text{CO}_3$  and NaCl <sup>[10]</sup>.

Figure 1. Pyrometric cone from the glass mold.



After calcination and cooling, measurements were made of the height (h) and the base diameter (db) of the cones to classify them according to the percentage of dimensional variations. Further measurements were performed to identify the composition ratios of Li<sub>2</sub>O:Na<sub>2</sub>CO<sub>3</sub>:NaCl based on the temperature and time intervals, determining the ideal cycles of calcination that promote a higher yield of lithium extraction.

In the characterization of the materials, X-ray diffractograms were obtained with a Bruker D2-Phaser equipped with a Lynxeye detector and Cu radiation, using a divergent slit of 0.6 mm and a central slit of 1 mm. The measurement step (acquisition time) was 0.02° (0.1 s) for fast measurements and 0.004° (0.6 s) for indexing data.

The micrographs were obtained by SEM, and the images were obtained mainly through the use of secondary electrons, using a JEOL (JSM 6300) Link-Isis scanning electron microscope, equipped with a conventional thermionic emitter and working at 20 kV, with the sample at a distance of 7-15 mm from the microscope lens.

The chemical compositions were obtained with an atomic absorption spectrophotometer by VARIAN, model AA.

The beta-spodumene was supplied by Companhia Brasileira de Lithium (CBL), with the chemical composition shown in Tab. 1, with a Si/Al molar ratio = 2.6. Carbonate and sodium chloride were of analytical quality without further purification.

Table 1. Mean chemical composition of beta-spodumene samples (wt%).

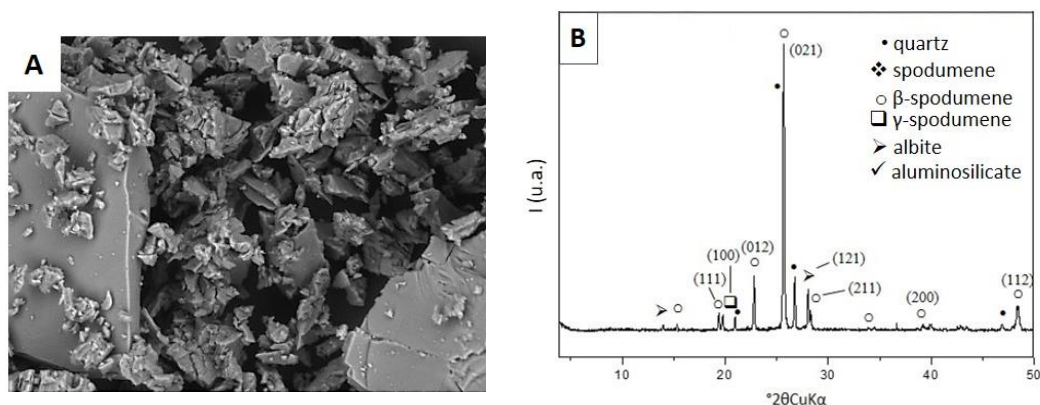
Component	SiO <sub>2</sub>	Al <sub>2</sub> O <sub>3</sub>	Li <sub>2</sub> O	Fe <sub>2</sub> O <sub>3</sub>	K <sub>2</sub> O	others
Content (%)	68.97	22.31	6.43	0.92	0.42	< 0.40

## Results and discussion

The result of the characterization of the ore by XRD is shown in Fig. 2a. The main species identified were: quartz (ICSD 27831), beta-spodumene (ICSD 14235), gamma-spodumene (ICSD 24897) and albite (ICSD 87654).

The presence of gamma-spodumene was confirmed by the reflections at  $2\theta = 19.6^\circ, 25.6^\circ, 34.4^\circ, 39.8^\circ$  and  $48.7^\circ$ , with the last four reflections superimposed with the beta-spodumene reflections, and increases the stability due to the polymorph gamma from the transition between alpha and beta-spodumene <sup>[1]</sup>.

Figure 2. a) SEM and b) XRD of beta-spodumene.



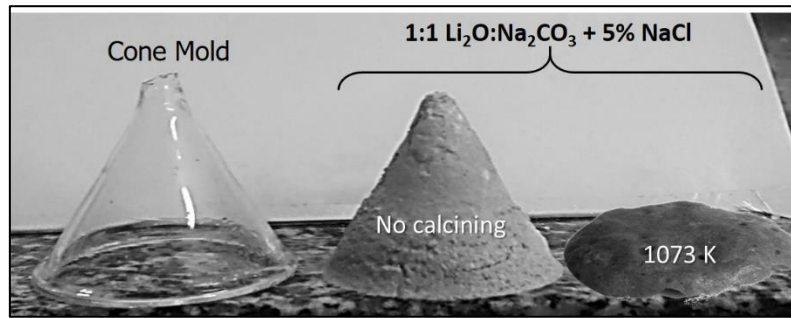
The main difference between  $\alpha$  and  $\beta$  polymorphs is that in alpha-spodumene, Al and Si are octahedrally coordinated, and as a result of the pyrometallurgical treatment, the structure suffers a reduction in packing density, where Si and Al become tetrahedrally coordinated [2].

During the successive phase transformation of  $\alpha$ - $\gamma$ - $\beta$ , a relaxation of the structure occurs, with a volume reduction up to 15% of the initial volume. Consequently, the distance between successive lithium ions varies between 2 Å and 7 Å, resulting in layers of tetrahedra that form sheets along the three crystallographic directions in the beta-spodumene crystals, justifying the irregular morphology of the material (Fig. 2b) [11].

Effect of reaction temperature.

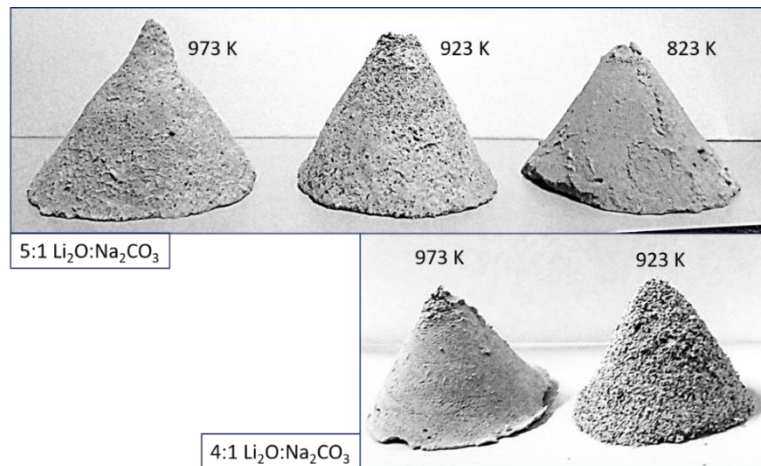
From Fig. 3, analyzing the pyrometric cones calcined, the surface vitrification (fusibility of the material) was observed, independent of the molar composition of  $\text{Li}_2\text{O}:\text{Na}_2\text{CO}_3:\text{NaCl}$ , in the temperature range between 1023-1073 K. Through the chemical incorporation of lithium into the glass, the conversion rate for  $\text{Li}_2\text{CO}_3$  was reduced, as a consequence of the excess of liquid phases formed during the calcination at high temperatures [12].

Figure 3. Mixing cones with a 1:1  $\text{Li}_2\text{O}:\text{Na}_2\text{CO}_3$  molar ratio and 5% NaCl.



The addition of more beta-spodumene (5:1  $\text{Li}_2\text{O}:\text{Na}_2\text{CO}_3$  molar ratio) significantly reduced the visual effect of the pyroplastic deformation. Indirectly, the increase in  $\text{SiO}_2$  provided an increase in the viscosity of the system from the rate of dissolution. The visual result, observed in Fig. 4, was the densification of the material and the increase in the porosity of the cones (923 K), obtained by eliminating  $\text{CO}_2$  as a result of the partial decomposition of the carbonate and the higher conversion rate [13, 14].

Figure 4. Cone profiles with 5:1 and 4:1 molar ratios of  $\text{Li}_2\text{O}:\text{Na}_2\text{CO}_3$  and 5% NaCl.



Data from Tab. 2 show that in the calcination, beta-spodumene behaved as a material with refractory properties. The addition of  $\text{Na}_2\text{CO}_3$  minimized this condition to an intermediate character between a fused flux and refractory material.

Evidence of the material melting at 1023 K was verified. At this temperature, the liquid phase was sufficiently present to deform the cone, characterized by the enlargement of its base ( $\Delta\% > 10\%$ ), except for molar ratios of  $\text{Li}_2\text{O}:\text{Na}_2\text{CO}_3 < 3:1$ , in which the liquid and solid coexisted in thermodynamic equilibrium at the intervals of the calcination conditions used.

Table 2. Dimensional variation data of cones after calcination.

Cone molar composition Li <sub>2</sub> O:Na <sub>2</sub> CO <sub>3</sub>	T <sub>max</sub> (K)	Δdb* (%)
1:0	673	+0,3
	873	+0,2
	1073	+0,2
5:1	673	+1,5
	873	+1,4
	1073	+1,8
4:1	673	+2,3
	823	+2,6
	650	+2,9
	1023	+4,5
3:1	823	+4,0
	923	+3,8
	1023	+15,2
1:1	823	+14,4
	1023	+22,0
	1073	+30,3

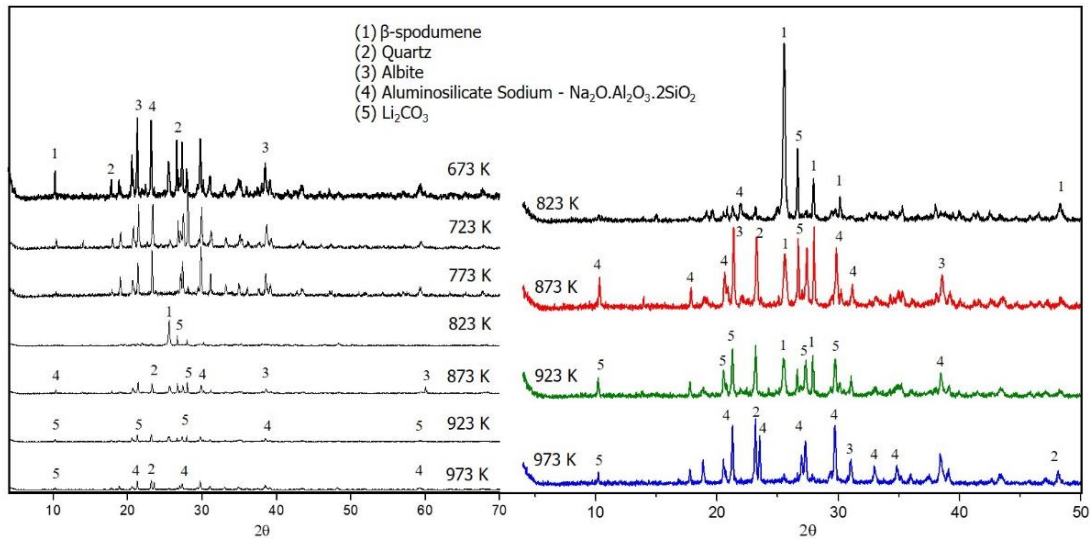
\*Δdb = variation in the diameter of the base.

According to the diffractograms of Fig. 5, the working temperature of 923 K produced characteristic peaks of Li<sub>2</sub>CO<sub>3</sub>, confirming a higher conversion rate for this temperature with the 4:1 Li<sub>2</sub>O:Na<sub>2</sub>CO<sub>3</sub> molar ratio.

The use of excessive temperatures in the calcination promotes collateral reactions forming lithium compounds with poor solubilization. When the Li<sub>2</sub>O:Na<sub>2</sub>CO<sub>3</sub> system is calcined in the range of 823-923 K, the available sodium aluminosilicate is practically converted, and the displaced lithium is obtained in the Li<sub>2</sub>CO<sub>3</sub> form [15].

In contrast, at 973 K, the presence of carbonates (Na<sub>2</sub>CO<sub>3</sub>, Li<sub>2</sub>CO<sub>3</sub>, or both) and their interaction with the available sodium aluminosilicate resulted in complex compounds of Na-Li aluminosilicates, and these dissolved only in an acid medium for the conversion and recovery of the corresponding salt of lithium, although contaminated with sodium in the form of sodium sulfate [15].

Figure 5. XRD of the calcined 4:1  $\text{Li}_2\text{O}:\text{Na}_2\text{CO}_3$  molar ratio.



Effect of reaction duration.

The duration of the calcination reaction of the  $\text{Li}_2\text{O}:\text{Na}_2\text{CO}_3:\text{NaCl}$  system was studied for 823 K, 873 K, and 923 K for 30 to 300 min. The results are shown in Fig. 6 and reveal that the extent of conversion increased with the reaction temperature and time, achieving a conversion of 71% for 120 min at 923 K. It can be observed that for the reaction temperatures of 823 and 873 K, the conversion efficiency remained nearly constant after 150 min of calcination.

Figure 6. Effect of the time and calcination temperature of the 4:1  $\text{Li}_2\text{O}:\text{Na}_2\text{CO}_3$  system on the conversion to  $\text{Li}_2\text{CO}_3$ .

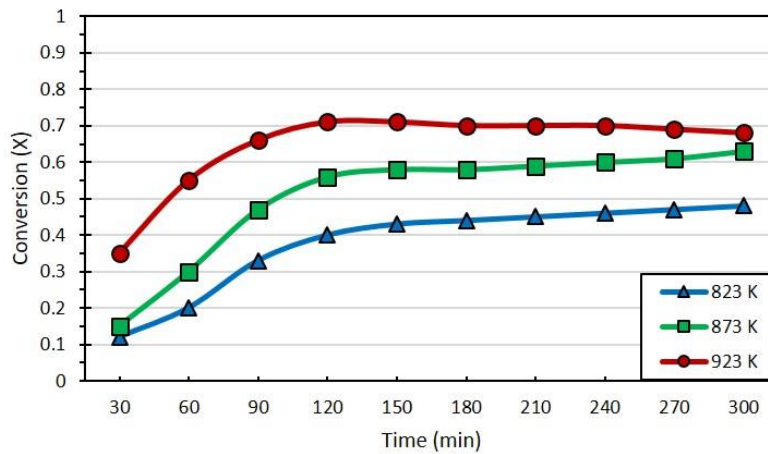
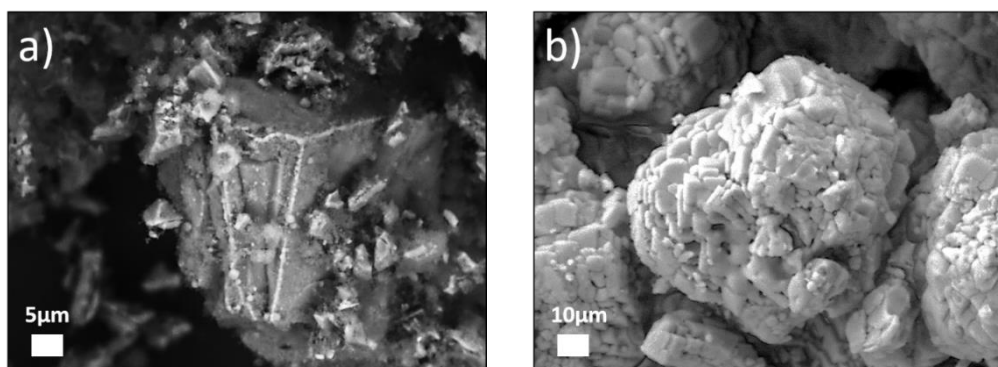


Fig. 7a shows sample micrographs for the calcination at 823 K for 120 min, where small incrustated particles were observed on an aggregate of beta-spodumene crystals. This indicates that a chemosynthetic attack occurred at preferential sites on the surface of beta-spodumene.

Fig. 7b shows the product of the calcination at 923 K after 120 min with a conversion of 71% and with a higher amount of  $\text{Li}_2\text{CO}_3$  incrustated.

Figure 7. SEM micrographs of the calcination products: a)  $X = 0.5$ , time = 120 min, and temperature = 823 K and b)  $X = 0.7$ , time = 120 min, and temperature = 923 K.



The reaction process, involving the calcination between beta-spodumene,  $\text{Na}_2\text{CO}_3$  and  $\text{NaCl}$ , therefore, comprises three distinct steps: (i) the decomposition of sodium carbonate at temperatures above 673 K, with the formation of sodium oxide and the release of carbon dioxide; (ii) the "relaxation" of the beta-spodumene phase (more reactive) and the chemoselective exchange between  $\text{Li}^+$  and  $\text{Na}^+$  (reduced spatial volume); (iii) the solid-solid reaction that occurs through the contact between beta-spodumene and sodium oxide, with the formation of lithium aluminate, sodium silicate and lithium carbonate.

Through the diffractograms and micrographs presented, steps (ii) and (iii) occurred nearly simultaneously in the treatment whose temperature reached 923 K.

Fig. 8 shows the conversion rates for calcinations with different  $\text{Li}_2\text{O}:\text{Na}_2\text{CO}_3$  molar ratios and different heating rates (5 and  $50^\circ\text{C}/\text{min}$ ) at a temperature of 923 K.

It was observed that for the molar ratios of 1:1 and 2:1  $\text{Li}_2\text{O}:\text{Na}_2\text{CO}_3$ , there was basically no exchange reaction, a phenomenon evidenced by the low lithium extraction and conversion to  $\text{Li}_2\text{CO}_3$ . The most interesting results were obtained for the 3:1 and 4:1 molar ratios at a heating rate of  $5^\circ\text{C}/\text{min}$ , with lithium recoveries of approximately 71% and 58%, respectively.

The low conversions of the blends with 1:1 and 2:1 molar ratio ratios of  $\text{Li}_2\text{O}:\text{Na}_2\text{CO}_3$  can be explained by a stoichiometric imbalance, i.e., the absence of  $\text{Na}_2\text{O}$  in the last reaction step, which occurs during the chemoselective exchange process, required for transformation of the lithium aluminate into sodium aluminate, according to Eq. (3).

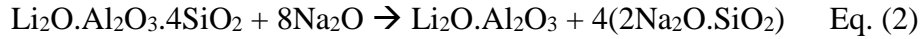
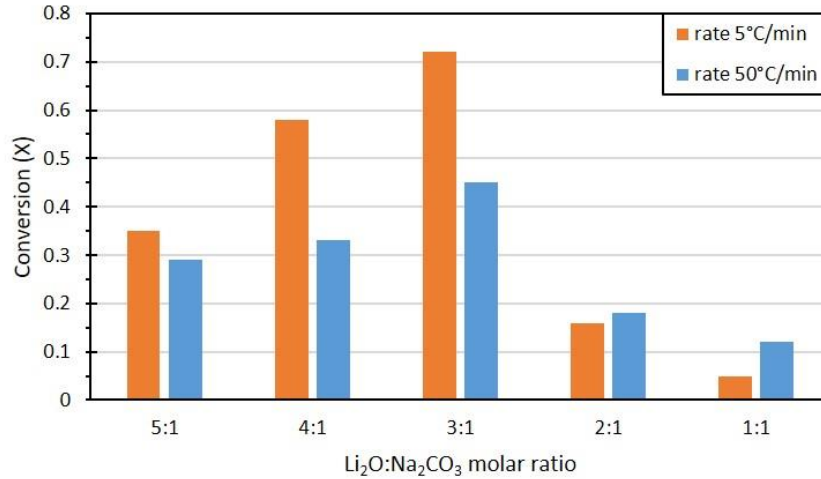


Figure 8. Conversion and heating rate for different molar ratios ( $\text{Li}_2\text{O}:\text{Na}_2\text{CO}_3$ ) at 923 K.



Based on the results of the calcination tests, it was found that the best molar ratio ( $\text{Li}_2\text{O}:\text{Na}_2\text{CO}_3$ ) is 3:1, in which it gave a conversion to  $\text{Li}_2\text{CO}_3$  in a 71% yield. It is expected that the processing of the beta-spodumene concentrate with  $\text{Na}_2\text{CO}_3$  and  $\text{NaCl}$  for the production of lithium carbonate will provide advantages, especially in the substitution of high-cost inputs, such as sulfuric acid, with carbonate and sodium chloride ( $\text{Na}_2\text{CO}_3$  and  $\text{NaCl}$ ) at accessible price.

#### Kinetic treatment of experimental data

The experimental data of the mineral decomposition during the calcination were analyzed with the software "Modelado" <sup>[16]</sup>, developed for the kinetic modeling of transformation reactions and solid decomposition <sup>[17]</sup>.

For each of the models, the main objective of the software is to solve the function in Eq. 4:

$$\Phi_m = \text{Min}_{b_m} \left\{ \sum_{j=1}^{N_{ex}} (X_{m,n} - X_{ex,n})^2 \right\} \quad \text{Eq. (4)}$$

where  $\Phi_m$  is the objective function attached to the m-th model, whose minimum must be estimated by the selection of  $b_m$ ;  $b_m = (b_1, b_2, b_3, \dots)$ ;  $T$  is the vector of the coefficients attached to the m-th model;  $X_{m, n}$  is the conversion that predicts the m-th model in the n-th experiment; and  $X_{ex, j}$  is the mean conversion percentage of the n-th experiment.

Since the data of the experimental system were correlated by the different models, based on the smaller variance associated with each model, the software presented a list of the most probable models. The second discrimination of the models was performed by estimating the kinetic coefficients linked to each of the most likely models.

Kinetic models were estimated using the experimental data obtained at different temperatures (Fig. 6), selecting as the most probable models those that had a regression error, associated with each temperature level, lower than 10%. In addition, the assumptions of each  $\text{Li}_2\text{O}:\text{Na}_2\text{CO}_3$  molar ratio and the results obtained from the characterizations of the calcination products (XRD and SEM) were taken into account.

The model of "nucleation and growth of crystals" was better fitted to the experimental data from the beta-spodumene decomposition and reaction with the alkali salts, at different temperatures and reaction times, and the mathematical expression of this model is presented in Eq. 5:

$$\ln(1 - X) = -b_1 \left[ \ln(1 + b_2 t) - \frac{b_2 t}{1 + b_2 t} \right] \quad \text{Eq. (5)}$$

where the coefficients  $b_1$  and  $b_2$  are defined as:

$$b_1 = \frac{\sigma_g N_S^0 \Omega^0 b_{MBrS}}{b_2 \rho d_p} \quad \text{Eq. (6)} \quad b_2 = k_{N_2} N_S^0 \quad \text{Eq. (7)}$$

and the coefficients  $r_s$ ,  $k$  (velocity constant) and  $k_{N_2}$  (conversion rate), are defined as:

$$r_s = k c_A^n \quad k = A_1 e^{-\frac{E_a}{RT}} \quad k_{N_2} = A_2 e^{-\frac{E_n}{RT}} \quad \text{Eq. (8)}$$

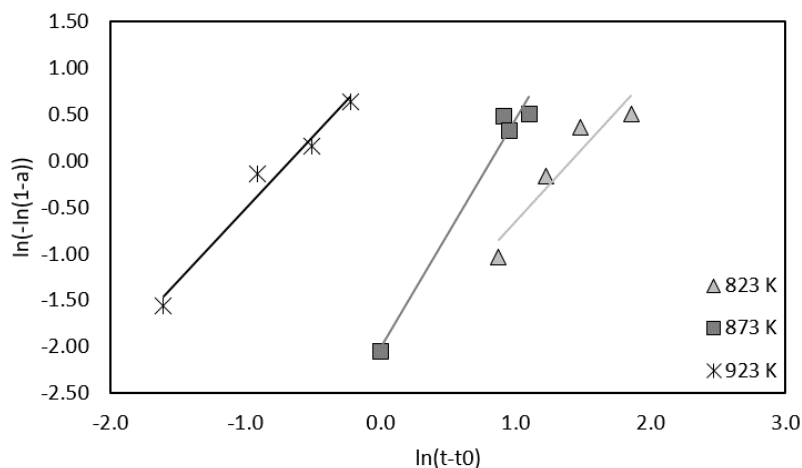
The frequency factor 'A' represents the frequency of collisions between the molecules in the reaction medium. 'Ea' is the apparent activation energy for the nucleation period 'EN', 'R' is the gas constant and 'T' is the absolute temperature. 't' is the total time (nucleation period + crystal growth period), and 'n' is a constant empirical exponent.

The values of the kinetic parameters estimated by the software are shown in Tab. 3 and plotted in Fig. 9. The kinetic constant 'k' is defined as the product of  $b_1$  and  $b_2$  [16].

Table 3. Kinetic parameters for the estimated model.

Temp. (K)	$b_1$	$b_2$	K
823	0.3175	1.95	0.6191
873	0.3560	2.12	0.7547
923	0.4211	3.53	1.4864

Figure 9. Crystallization curves plotted for  $\ln(-\ln(1-a))$  vs.  $\ln(t-t_0)$ .

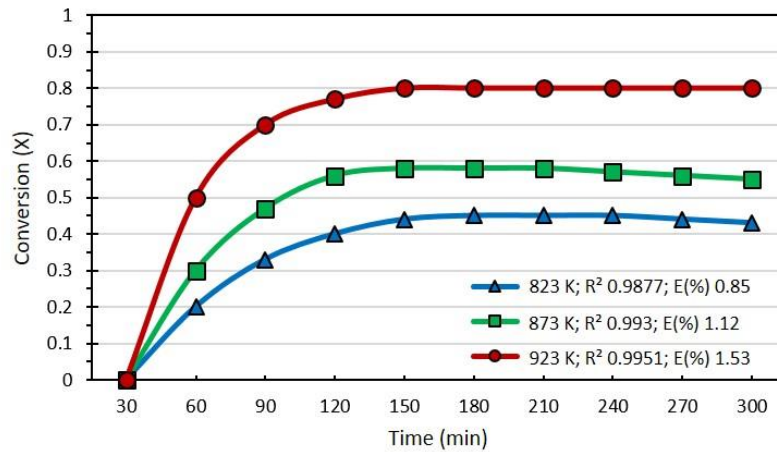


The fitting results of the experimental data (X vs. T, at different temperatures) with the model are shown in Fig. 10. It can be noted that the experimental results and the values predicted by the kinetic model are in excellent agreement, from the coefficients of correlation ( $R^2$ ).

The developed kinetic model proposes a sequential nucleation process in which the reagent particles are constituted by a solid nonporous reagent, with the formation of solids remaining bound to the particle. These hypotheses are consistent with the results obtained by SEM [16].

The model assumes a system in which one of the solid reactants undergoes a thermochemical attack at specific surface locations. The causes of the origin of the preferred sites of interaction may be diverse, such as heterogeneities often present on solid surfaces caused by crystalline defects or impurities in the solid [16].

Figure 10. Correlation between experimental data and the proposed model.



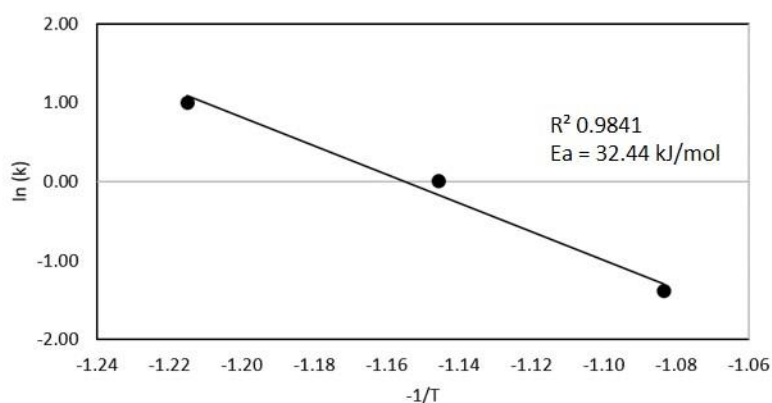
The reaction is initiated at the preferential points susceptible to chemical interaction and then advances, as evidenced by the formation of pores that grew from the surface to the interior of the particle. The results obtained by SEM of the calcination products of  $\text{Li}_2\text{O}:\text{Na}_2\text{CO}_3:\text{NaCl}$  molar mixtures allow us to confirm that the experimental data coincide with the hypotheses raised through the proposed model [8].

Barbosa et al. and Rosales et al. studied the chlorination and fluorination kinetics of beta-spodumene and observed that the reaction with chlorine and fluoride starts at preferential sites on the mineral surface. They suggest that defects present in the crystalline structure of the mineral may explain the formation of these preferential properties [18].

The stage that determines the conversion rate can be represented by the activation energy ( $E_a$ ). A diffusion-controlled process is characterized by being slightly temperature dependent ( $E_a < 12.5$  kJ/mol), while the chemically controlled process is strongly temperature dependent ( $E_a > 42$  kJ/mol) [18]. Therefore, the diffusion coefficients and the conversion rate depend linearly and exponentially on the temperature, respectively.

The kinetic coefficient of the reaction rate was calculated using the set of relations of Eq. (8). The value of  $E_a$  for the decomposition reaction was calculated from the graph of  $\ln k$  vs.  $1/T$  (Fig. 11).

Figure 11. Arrhenius parameter for the decomposition of beta-spodumene by calcination with alkaline salts.



The slope of the line in Fig. 11 allows estimating the apparent activation energy for the thermal decomposition of beta-spodumene, equal to  $E_a = 32.4$  kJ/mol. This value suggests that the conversion process is controlled by (i) the formation of the reaction interface through diffusional control, and (ii) the chemical reaction by means of a chemoselective exchange.

## Conclusions

The data obtained show that the conversion rate in  $\text{Li}_2\text{CO}_3$  increased with the addition of beta-spodumene and decreased with the increase in the calcination rate and decrease in the solid-solid molar ratio of beta-spodumene and  $\text{Na}_2\text{CO}_3$ .

The maximum conversion was 71%, which was obtained with a thermal cycle of 120 min at 923 K and with a calcination rate of  $5^\circ\text{C}/\text{min}$ . The SEM characterization of the products suggests that beta-spodumene undergoes an irregular localized attack at preferential sites on the particle (defects), where the reaction develops.

The kinetic model based on the "nucleation and growth of crystals" was well fitted to the experimental results of mineral decomposition in a reaction medium with alkali salts. The activation energy was 32.4 kJ/mol over the temperature range of 823-923 K. This value suggests that the thermal decomposition process is controlled by two stages: reaction (diffusion) and chemical reaction (chemoselective exchange).

## Acknowledgments

This study was financed in part by the Coordenação de Aperfeiçoamento de Pessoal de Nível Superior - Brazil (CAPES) - finance code 001. The authors would like to thank Companhia Brasileira de Lítio - Brazil (CBL), for the beta-spodumene samples and the Instituto de Tecnología Química - Spain (ITQ), for the characterization of the materials.

## References

- [1] WILLS, B. A., & FINCH, J.; **Wills' mineral processing technology: an introduction to the practical aspects of ore treatment and mineral recovery**. Butterworth-Heinemann. 2015.
- [2] CHEN, Y., TIAN, Q., CHEN, B., SHI, X., & LIAO, T.; Preparation of lithium carbonate from spodumene by a sodium carbonate autoclave process. **Hydrometallurgy**, 109.1-2 (2011), p. 43-46.
- [3] BARBOSA, L. I., GONZÁLEZ, J. A., & del CARMEN RUIZ, M.; Extraction of lithium from  $\beta$ -spodumene using chlorination roasting with calcium chloride. **Thermochim. Acta**, 605 (2015), p. 63-67.
- [4] SALAKJANI, N. K., SINGH, P., & NIKOLOSKI, A. N.; Mineralogical transformations of spodumene concentrate from Greenbushes, Western Australia. Part 1: Conventional heating. **M. Engin.**, 98 (2016), p. 71-79.
- [5] GRUBER, P. W., MEDINA, P. A., KEOLEIAN, G. A., KESLER, S. E., EVERSON, M. P., & WALLINGTON, T. J.; Global lithium availability: A constraint for electric vehicles?. **J. Ind. Ecol.**, 15.5 (2011), p. 760-775.
- [6] KUMAR, M., MANKHAND, T. R., MURTHY, D. S. R., MUKHOPADHYAY, R., & PRASAD, P. M.; Refining of a low-grade molybdenite concentrate. **Hydrometallurgy**, 86.1-2 (2007), p. 56-62.
- [7] WANG, F., WU, X., LI, C., ZHU, Y., FU, L., WU, Y., & LIU, X.; Nanostructured positive electrode materials for post-lithium ion batteries. **Energy Environ. Sci.**, 9.12 (2016), p. 3570-3611.
- [8] BARBOSA, L. I., VALENTE, G., OROSCO, R. P., & GONZALEZ, J. A.; Lithium extraction from  $\beta$ -spodumene through chlorination with chlorine gas. **Miner. Eng.**, 56 (2014), p. 29-34.

- [9] ROSALES, G. D., DEL CARMEN RUIZ, M., & RODRIGUEZ, M. H.; Alkaline metal fluoride synthesis as a subproduct of  $\beta$ -spodumene leaching. **Hydrometallurgy**, 139 (2013), p. 73-78.
- [10] **NBR ISO 528:2014** (p. 8-10), São Paulo: ABNT. 2014.
- [11] HATCH, R. A.; **Am. Mineral.**, 28 (1943), p. 472-495.
- [12] GREEN, D. J.; **Transformation toughening of ceramics**, CRC press. 2018.
- [13] BARBA, A., BELTRÁN, V., FELÍU, C., GARCIA, J., GINÉS, F., SÁNCHEZ, E., SANZ, F.; **Materias primas para la fabricación de soportes de baldosas cerámicas** (2ª ed.), Castellón: Instituto de Tecnología Cerámica. 2002.
- [14] REN, M., & DU, J.; Structural origin of the thermal and diffusion behaviors of lithium aluminosilicate crystal polymorphs and glasses. **J. Am. Ceram. Soc.**, 99.8 (2016), p. 2823-2833.
- [15] MOREIRA, G. C., GONÇALVES, C. C., FRANÇA, S. C. A., & BRAGA, P. F. A.; Uma nova rota tecnológica para a produção de hidróxido de lítio a partir de minério de espodumênio. **Holos**, 6 (2017), p. 162-169.
- [16] ROSALES, G. D., RUIZ, M. C., & RODRIGUEZ, M. H.; Study of the extraction kinetics of lithium by leaching  $\beta$ -spodumene with hydrofluoric acid. **Minerals**, 6.4 (2016), p. 98-109.
- [17] KHAWAM, A., & FLANAGAN, D. R.; Solid-state kinetic models: basics and mathematical fundamentals. **J. Phys. Chem. B.**, 110.35 (2016), p. 17315-17328.
- [18] KHATER, G. A., & MORSI, M. M.; Glass-ceramics based on spodumene–enstatite system from natural raw materials. **Thermochim. Acta**, 519.1-2 (2011), p. 6-11.

## Chapter 6. Template-free MFI-type zeolite synthesis in the lithium extraction route from beta-spodumene samples

---

Leonardo L. dos Santos<sup>1</sup>; Antonio C. Lara<sup>2</sup>; Rubens M. do Nascimento<sup>1</sup>; Sibeles B. C. Pergher<sup>3</sup>

<sup>1</sup> Department of Materials Science and Engineering, Federal University of Rio Grande do Norte, Natal 59078-97, Brazil.

<sup>2</sup> Department of Chemistry, Instituto de Tecnología Química, Valencia 46022, Spain.

<sup>3</sup> Department of Chemistry, Laboratório de Peneiras Moleculares, Federal University of Rio Grande do Norte, Natal 59078-97, Brazil.

**Abstract:** The lithium extracted from lithium pegmatites is associated with sulfates, magnesium and other elements as impurities, which makes recovering lithium as a salt through the use of organic solvents and actinide bases difficult and results in the abundant formation of residues rich in Si and Al. The viability of the process depends on the yield and recovery of lithium in addition to transformation of the residue into a byproduct of commercial interest. In this paper, we describe a continuous, cyclic, environmentally friendly, solvent-free organic process for the extraction of lithium as  $\text{Li}_2\text{CO}_3$  with yields of more than 80% and simultaneous production of MFI-type zeolite with SAR = 30, named LPM-18, which has promising physicochemical properties for application in refining processes or use as a catalytic support. Due to the absence of an organic template, we can classify this synthesis as having the potential to reduce environmental impacts and production costs.

**Keywords:** MFI-type zeolite. Template-free. Beta-spodumene. Lithium extraction. Environmentally-friendly

### Introduction

Lithium is important in the pharmaceutical (psychoactive drugs for the treatment of mental disorders), ceramic and metallurgy sectors. Global demand of lithium carbonate equivalent (LCE) in 2017 was 230 kt with a predicted composite annual growth rate (CAGR) of 7-9% through 2025 <sup>[1, 2]</sup>.

Currently, there are two viable sources for lithium extraction: a) brines (66%) with inconsistent high levels of soluble impurities (Mg, Ca, B, and  $\text{SO}_4^{2-}$ ) and b) pegmatites (28%), which include approximately 150 cataloged varieties and subclasses of ores containing lithium. South America possesses more than half of the world's resources and reserves of lithium, and 22% of lithium comes from the mineral spodumene [3].

Spodumene is a double lithium aluminum silicate,  $\text{LiAl}(\text{SiO}_3)_2$ , with theoretical and practical  $\text{Li}_2\text{O}$  chemical compositions of 8.04% and 4.0 to 6.5%, respectively. Beta-spodumene is the product recrystallized after thermal decomposition of spodumene between 1073-1273 K and is characterized by excellent chemical stability and reactivity for extracting the metal in salt form [4].

In approximately 55% of the procedures found in the literature on lithium extraction from spodumene, the lithium salt formed is  $\text{Li}_2\text{CO}_3$  in addition to water-soluble Al and Na silicates, usually complex sodium-lithium aluminosilicate. The ratio is 1 ton of  $\text{Li}_2\text{CO}_3$  produced to 10 tons of residue, which according to Oliveira et al. (2017), can be reused as an alternative source of Si and Al for zeolite synthesis [4, 5].

Zeolites are molecular sieves and low-density crystalline tectosilicates with regular microporosity between 0.3-2.0 nm, which depending on the structural topology, have a heterogeneous chemical composition subdivided among 235 structural types [6].

The MFI-type zeolite (Mobil-five) has high thermal and acid stability and is suitable for shape selectivity and activity in catalytic cracking reactions for the production of light olefins with the retention of undesirable products, such as methane in the fluid catalytic cracking process [7].

ZSM-5 is an aluminosilicate zeolite belonging to the pentasil family of zeolites. The standard synthesis is performed with aqueous gels containing sources of the structural elements, a mineralizing agent, a directing agent, and, in some cases, a codirecting agent [7].

Structural templates have at least two functions in the synthesis: in addition to defining the specific topology, in which factors such as charge density, shape and volume of the molecule are determinants, they also act to moderate the pH of the synthesis gel. Usually, nitrogenous organic compounds such as n-butylamine and tetra-propyl ammonium cation are used [8].

To replace these organic nitrogen compounds, which have a high cost and toxicity, some authors have evaluated the use of coprecipitators [9].

In this paper, we propose an organic template-free procedure for lithium extraction from beta-spodumene with the simultaneous formation of MFI-type zeolite (H-form) as an easily recoverable crystalline byproduct.

## Experimental

Lithium extraction and zeolite synthesis.

The beta-spodumene was supplied by Companhia Brasileira de Lithium (CBL) with the chemical composition shown in Tab. 1 and a Si/Al molar ratio = 2.6. Carbonate, sodium chloride and hydroxide, ammonium bicarbonate and hydrochloric acid were of analytical quality and used without further purification.

Table 1. Chemical analysis of the beta-spodumene sample (wt%).

Component	SiO <sub>2</sub>	Al <sub>2</sub> O <sub>3</sub>	Li <sub>2</sub> O	Fe <sub>2</sub> O <sub>3</sub>	K <sub>2</sub> O	Others
Content (%)	68.97	22.31	6.43	0.92	0.42	< 0.40

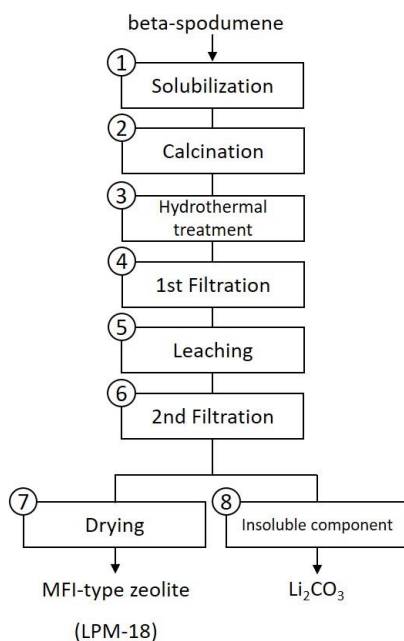
The synthesis procedure is shown in Fig. 1, and the methodology was patent-based [10]. Initially, 6.5 g of beta-spodumene was leached with 4 mol.L<sup>-1</sup> HCl solution under stirring at 343 K. The solution was filtered, and the liquor returned to reflux (Fig. 1, step 1). The dry powder was calcined with variable quantities of Na<sub>2</sub>CO<sub>3</sub> and NaCl, according to the following study on the Na<sub>2</sub>O content, under the following conditions: first cycle, between 823 K and 873 K for 20 min; second cycle, between 873 K and 923 K for 30 min with thermal cycling for less than 48 h (step 2).

The effects of the Na<sub>2</sub>O and H<sub>2</sub>O concentrations on the reaction medium were studied through a series of experiments using xNa<sub>2</sub>O:SiO<sub>2</sub>:30H<sub>2</sub>O and 0.19Na<sub>2</sub>O:SiO<sub>2</sub>:xH<sub>2</sub>O molar ratios, respectively. Two mother liquors were prepared with low and high contents of Na<sub>2</sub>O and supplemented by step 3 treatment conducted at 443 K, 453 K and 463 K in the range of 6-96 h.

The calcination product was soluble in the presence of a strong mineralizing agent, sodium hydroxide (98% NaOH), and the gel that formed was aged and discharged in autoclaves for greenhouse crystallization and MFI-type zeolite nucleation (steps 3-4). The lithium carbonate solution was recovered in step 5 after the addition of NH<sub>4</sub>HCO<sub>3</sub>. Finally, the solution was again filtered and centrifuged for recovery of the solid that was rich in ammonium-form zeolite crystals (NH<sub>4</sub>-MFI), thermally treated for volatilization

of  $\text{NH}_3$  (steps 6-7), and converted into the acid/protonated form (H-MFI) by ion exchange and calcination processes, respectively. Finally, the supernatant was heated to precipitate  $\text{Li}_2\text{CO}_3$  (step 8).

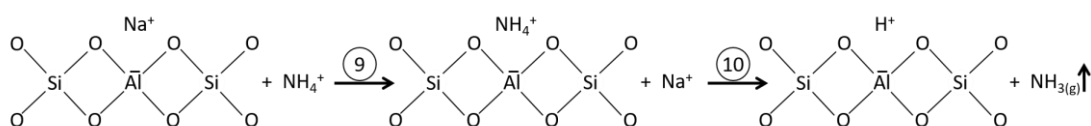
Figure 1. Procedure for extracting lithium from beta-spodumene and forming template-free MFI-type zeolite.



H-form conversion of the MFI-type zeolite.

The MFI-type zeolite from the procedure in Fig. 1 was obtained in sodium form (Na-LPM-18) and was converted to the proton form (H-LPM-18) by an ion exchange procedure through successive solubilization of the sample with a  $1.0 \text{ mol.L}^{-1} \text{ NH}_4\text{Cl}$  (1:100, g:ml) solution in a reflux system at 353 K for 2 h (Fig. 2, step 9) and subsequent thermal decomposition by heating the powder in a muffle furnace at 673 K for 3 h in an inert atmosphere (flow rate  $100 \text{ mL.min}^{-1}$ ) and a heating rate of  $274 \text{ K.min}^{-1}$  (step 10).

Figure 2. Ion exchange and thermal decomposition schemes of the H-form zeolite.



## Characterization.

To determine the content of different elements in the analyzed materials, atomic emission spectrometry (AES) was used. A sample amount (approximately 30 mg) was dissolved in an acidic medium, generally a mixture of hydrochloric and hydrofluoric acid. Measurements were made on a Varian 715/ES device.

The morphology of the samples was characterized by field-emission scanning electron microscopy (SEM). Powder XRD patterns of the dried solid products were recorded by a PANalytical X'pert diffractometer with CuK $\alpha$  radiation.

The relative crystallinity was determined from the peak areas between  $2\theta = 5^\circ$ - $50^\circ$ . The relative crystallinity degree (RCD) of the MFI-type zeolites was calculated by the ASTM D5758/2015 method by comparing the areas of the peaks between  $2\theta = 7^\circ$ - $9^\circ$  and  $22^\circ$ - $25^\circ$  [11]. A sample of MFI-type zeolite (ZSM-5, Si/Al molar ratio is 13) synthesized by the IZA method was used as the standard.

The textural properties were determined by the N<sub>2</sub> static adsorption and desorption technique using a TriStar 3000 instrument (Micromeritics). The specific area was calculated by the BET method. For the calculation of the volume of micropores and mesopores, the t-plot and BJH methods were used.

Initially, the sample was subjected to vacuum pretreatment at 673 K to clean the surface of the solid of any type of impurities. After the evacuation treatment, the solid was weighed in a sample holder and cooled to 77 K; then, nitrogen gas was introduced, and the volume of gas adsorbed was recorded against the pressure variation.

The determination of the acidity of the materials obtained was performed by the basic thermodesorption method (n-butylamine) to quantify the density and strength of the acid sites. Based on the amount in mols of n-butylamine desorbed per gram of material, the density of the acid sites can be quantified, and the desorption temperature range correlates with the acid strength of the sites.

After adsorption of the base to a fixed bed and continuous flow microreactor, the desorption of n-butylamine was examined in a thermobalance. The TGA/DTG curves of the samples were obtained in the range 323-873 K.

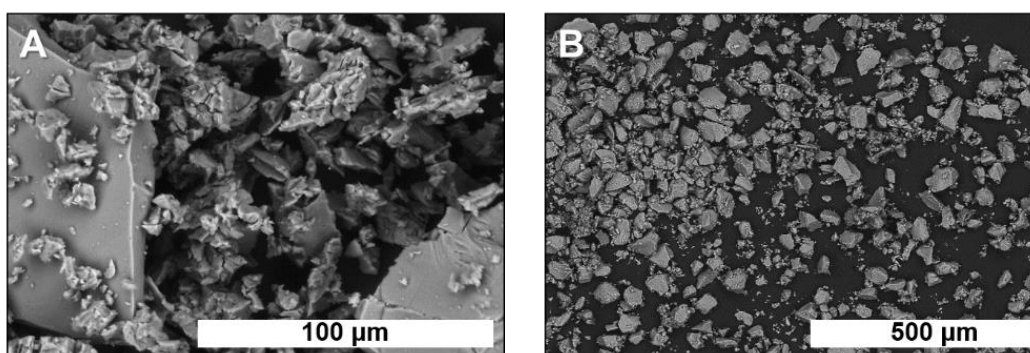
## Results and discussion

Lithium extraction.

The  $\text{SiO}_2/\text{Al}_2\text{O}_3$  molar ratio of dealuminated beta-spodumene was 30.6 (analyzed by microanalysis EDS and XRD). During the process of dealumination through removal (step 1), Al is not replaced by another element. Therefore, there are vacancies in the structure, resulting in a loss in crystallinity and the separation between successive lithium ions increasing from 2 Å to 7 Å, which results in the pairing of layers of tetrahedra on the sides and explains the irregular morphology (Fig. 3b) [4].

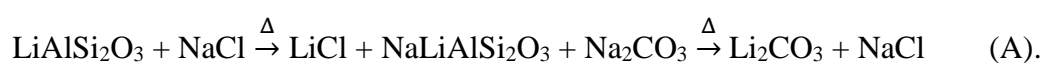
The beta-spodumene dissolution with HCl can be represented by the following reaction:  $\text{LiAlSi}_2\text{O}_{(s)} + 19\text{HCl}_{(aq)} \rightarrow \text{LiCl}_{(aq)} + \text{H}_3\text{AlCl}_{6(aq)} + 2\text{H}_2\text{SiCl}_{6(aq)} + 6\text{H}_2\text{O}$ .

Figure 3. Morphologies of: a) starting b-spod.; b) dealuminated b-spod.

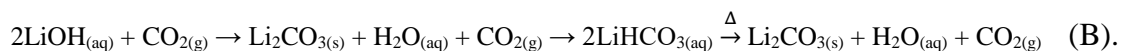


In the calcination step (step 2), a portion of the lithium substituted in the sodium structure forms a complex sodium-lithium aluminosilicate, which is partially recovered as soluble bicarbonate ( $\text{LiHCO}_3$ ) after the addition of  $\text{NH}_4\text{HCO}_3$  and heating of the supernatant to precipitate the corresponding salt  $\text{Li}_2\text{CO}_3$  (steps 3-8).

Fig. 4 shows the influence of the addition of  $\text{Na}_2\text{CO}_3$  and  $\text{NaCl}$  in the calcination stage (step 2) on the stoichiometric recovery of lithium in the extraction process (%  $\text{Li}_2\text{O}$ ) from the solid precipitated from the supernatant (step 8). The presence of  $\text{Li}_2\text{CO}_3$  is associated with excess sodium in the process according to reaction (A) [12]:

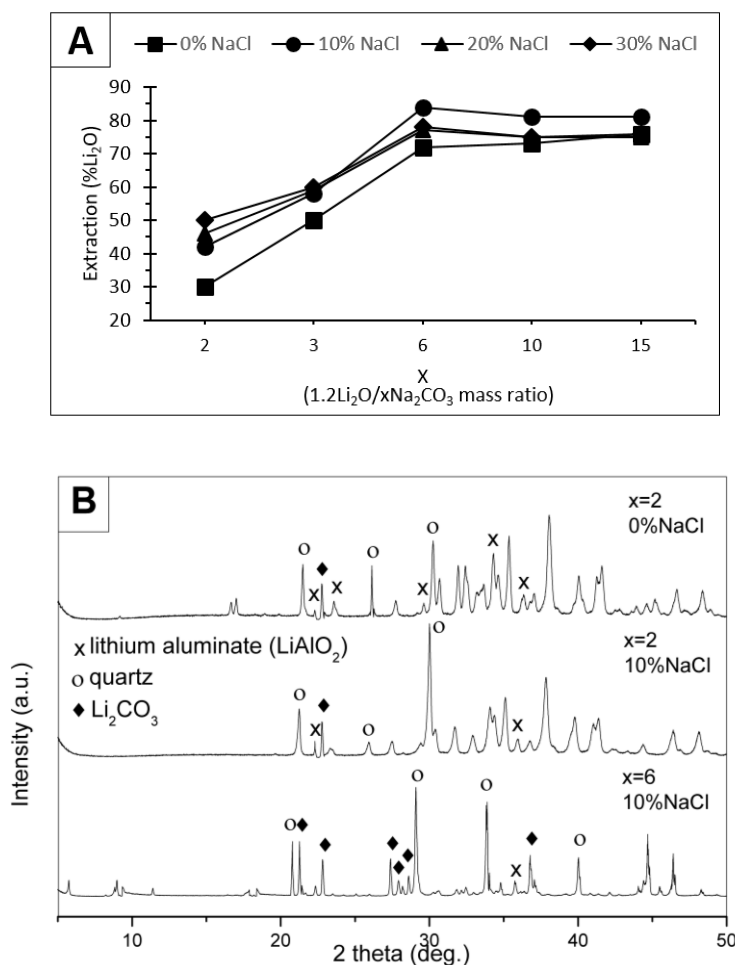


The energetically stable character of the formed lithium complex, which is associated with the steric hindrance principle, restricts the access of  $\text{CO}_3^{2-}$  species to the interstitial sites occupied by the remaining lithium in the beta-spodumene structure, preventing further substitution and forming lithium aluminum oxide ( $\text{LiAlO}_2$ ), which, unlike lithium hydroxide, is a precursor species in the conversion reaction to a more soluble bicarbonate, as shown in reaction (B) [13]:



Atomic absorption data showed that the addition of 10% NaCl to the global weight of the initial 1.2:6  $\text{Li}_2\text{O}:\text{Na}_2\text{CO}_3$  mass ratio resulted in the recovery of 84% lithium from the supernatant.

Figure 4. Influence of 1.2:X  $\text{Li}_2\text{O}:\text{Na}_2\text{CO}_3$  mass ratio and percentage of NaCl on the  $\text{Li}_2\text{O}$  extraction rate: a) extraction % and b) XRD solid precipitate.

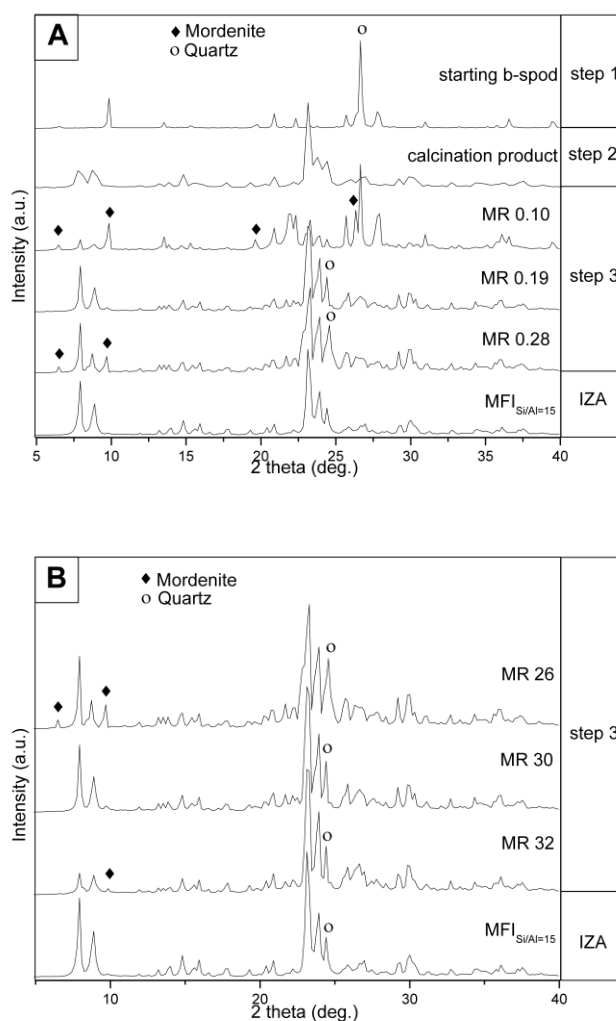


Effects of Na<sub>2</sub>O and H<sub>2</sub>O contents and kinetic study on the crystallization of MFI-type zeolite.

The additions of water and a mineralizing agent allowed the gel of the complex sodium-lithium aluminosilicate in step 3 to dissolve and transform into a liquid phase, providing a greater quantity of tetrahedral units (AlO<sub>4</sub>)<sup>-5</sup> and (SiO<sub>4</sub>)<sup>-4</sup> for the formation of secondary building units (SBUs) 5-1, which are characteristic of the pentasil group and required for the nucleation and crystallization of MFI topology zeolites. These zeolites are particularly sensitive to the concentration of Na<sup>+</sup> and OH<sup>-</sup> [6].

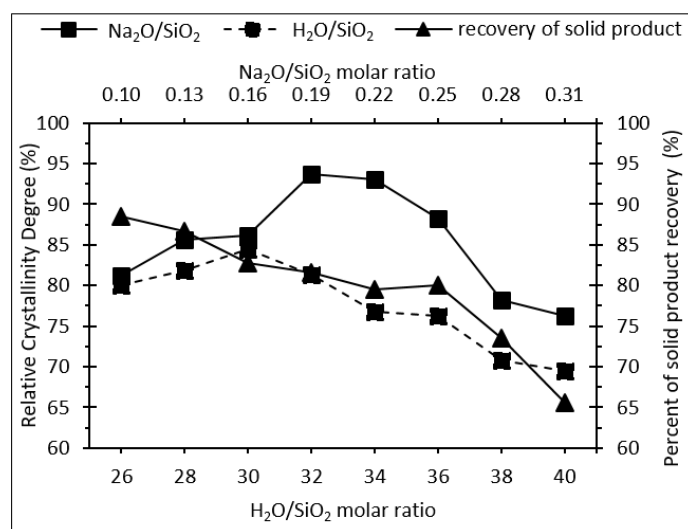
The XRD standard patterns and the Relative Crystallinity Degree (RCD) of the products are shown in Figs. 5 and 6, respectively. The obtained samples were designated MR-n, where n = Na<sub>2</sub>O/SiO<sub>2</sub> molar ratio (Fig. 5a) or n = H<sub>2</sub>O/SiO<sub>2</sub> molar ratio (Fig. 5b).

Figure 5. XRD patterns of MFI zeolites obtained with different molar ratios: (a) Na<sub>2</sub>O/SiO<sub>2</sub> and (b) H<sub>2</sub>O/SiO<sub>2</sub>.



At first, for a low Na<sub>2</sub>O content (MR 0.10), the characteristic peaks of MFI-type zeolite were not identified in relation to the IZA standard (Fig. 5a), showing that the available alkalinity and Na<sup>+</sup> ions were insufficient for the dissolution of amorphous silica in the gel and the subsequent transformation of the gel into crystalline zeolite MFI during hydrothermal treatment, resulting in a high percentage of amorphous solid recovered of approximately 88% (Fig. 6).

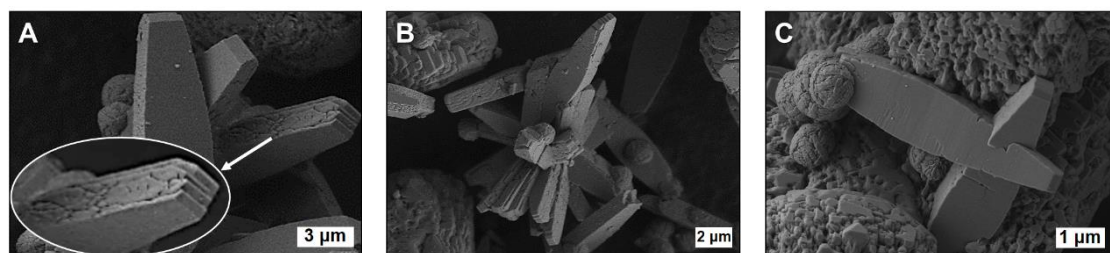
Figure 6. Influence of Na<sub>2</sub>O/SiO<sub>2</sub> and H<sub>2</sub>O/SiO<sub>2</sub> molar ratios on the crystallinity and percentage of solid product recovery.



The presence of the mordenite and quartz phases as impurities was observed when the H<sub>2</sub>O/SiO<sub>2</sub> molar ratio was 26 (MR 26, Fig. 5b).

In Fig. 7a, the presence of grooves on the surface of the crystal is related to excess alkalinity due to the low water content in the reaction medium, indicating that a) rapid crystallization occurred with the increasing viscosity of the medium, compromising the depolymerization of the silicate network and the homogeneity of the system; and b) a shorter distance between the species in solution contributed to nucleation and crystallization of the MFI-type zeolite with an RCD approximately equal to 80% (Fig. 6) [14].

Figure 7. SEM images of MFI-type zeolite samples with H<sub>2</sub>O/SiO<sub>2</sub> molar ratios of a) 26, b) 30 and c) 32.



With an increase in the Na<sub>2</sub>O concentration in solution (MR 0.19), the solubility of amorphous material increased, indicating that the concentration of silicates and aluminate ions required to form SBUs 5-1 was sufficient for nucleation (RCD 88.5%). To obtain sufficient species in solution, an adequate amount of water is required. As seen in Figs. 5a and 6, the crystallinity increased (RCD ~ 85%) due to the increase in water content (MR 30) and maintained a uniform crystal morphology free of undesirable phases (Fig. 7b).

Excess addition of NaOH (MR 0.28) caused an increase in alkalinity and the Na<sup>+</sup>/SiO<sub>2</sub> molar ratio, which was confirmed by the presence of undesired phases of mordenite and quartz due to the dissolution of SiO<sub>4</sub><sup>4-</sup> to balance the excess sodium ions in the reaction system because the amount of Na<sup>+</sup> was higher than that needed to balance the negative charge of the MFI-type zeolite structure. Due to the excess of water (MR 32), there was a natural reduction in the alkalinity of the system, which was responsible for the decrease in the crystallinity of the material (Figs. 5b and 7c).

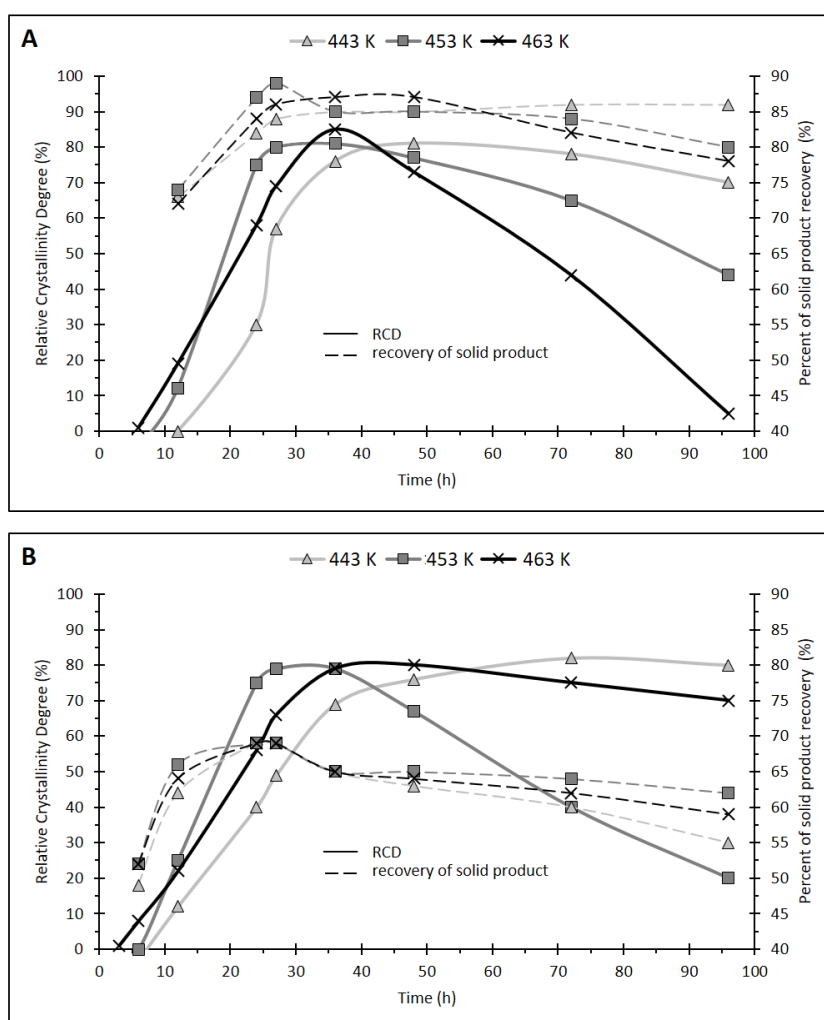
The factors governing the crystallization tendency of these materials can be explained by comparing the stability of the aluminosilicate complex obtained after calcination of the species and the alkalinity of the reaction system: when the aluminosilicate is exposed to high alkalinity conditions, it becomes more soluble, resulting in a reduction in the rate of transformation into crystalline solid product and the formation of mordenite (more metastable than MFI-type zeolite), which causes a lower percentage of recovered solid product [7, 14].

In contrast, when aluminosilicate is exposed to low alkalinity conditions, it is less soluble and crystallization occurs more rapidly, leading to amorphous phase formation with a high percentage of amorphous solid product. In this case, the aluminosilicate did not have enough time to form a crystalline phase characteristic of an MFI-type zeolite [14].

These results show the strong influence of Na<sub>2</sub>O content on the crystallinity and morphology of an MFI-type zeolite. These characteristics were complemented by data obtained from relating the time and temperature of crystallization to the Na<sub>2</sub>O content. Thus, the ideal mother liquors have a molar ratio of low Na<sub>2</sub>O (4Na<sub>2</sub>O:Al<sub>2</sub>O<sub>3</sub>:30SiO<sub>2</sub>:850H<sub>2</sub>O) and high (8Na<sub>2</sub>O:Al<sub>2</sub>O<sub>3</sub>:30SiO<sub>2</sub>:850H<sub>2</sub>O).

Figs. 8 and 9 show the dependence of the relative crystallinity and yield of the solid product and XRD standards on the time and temperature of crystallization.

Figure 8. Relative crystallinity degree and solid yield of MFI-type zeolite depending on the added amount of Na<sub>2</sub>O: a) low and b) high.



According to the curves in Fig. 8, the crystallization processes can be divided into three stages: induction, transition and crystal growth.

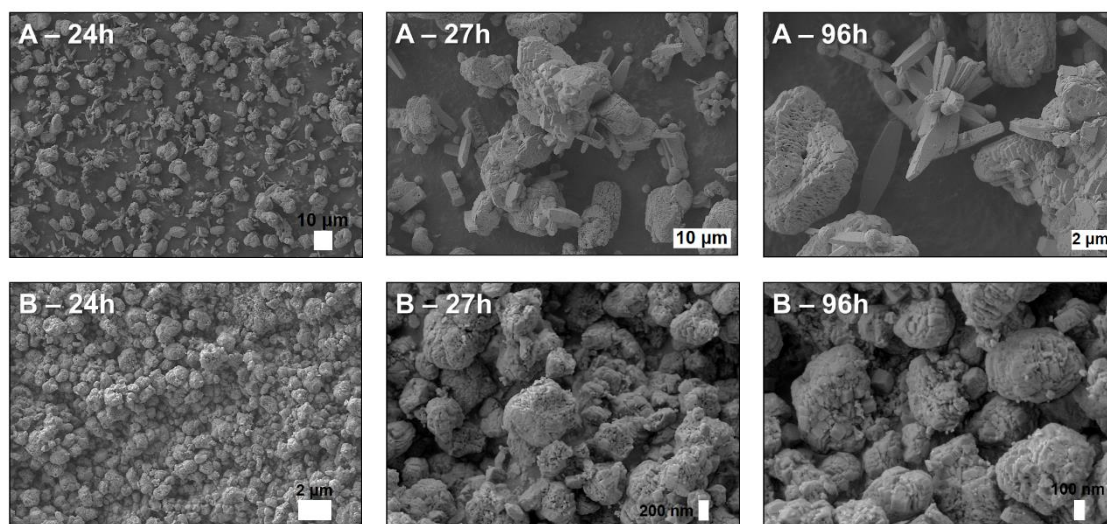
During the induction stage, the nucleation process is the rate-determining step. A longer period for induction was observed at a temperature of 443 K, which was limited

by the temperature increment and independent of the  $\text{Na}_2\text{O}$  content.

The induction period for high  $\text{Na}_2\text{O}$  content was shorter ( $< 6$  h) than that for low  $\text{Na}_2\text{O}$  content ( $\sim 12$  h). These values show that the dissolution of the aluminosilicate for gel formation was proportional to the temperature increase, and the Si and Al species could easily form the basic structural units to form an MFI-type zeolite, which was confirmed by the presence of characteristic peaks  $2\theta = 7^\circ\text{-}9^\circ, 22^\circ\text{-}25^\circ$  (Fig. 8a), after the period of induction (change in the slope of the curve).

The crystallization process started after 27 h at 453 K and after 36 h at 463 K and 443 K (Fig. 8b) and was characterized by the formation of thermodynamically more stable phases, mordenite and quartz, with morphological differences in the solid products formed by particles agglomerating throughout the entire period of crystallization for high  $\text{Na}_2\text{O}$  content (Fig. 9).

Figure 9. SEM images of the solid products depending on the time of crystallization at 453 K for a) low  $\text{Na}_2\text{O}$  and b) high  $\text{Na}_2\text{O}$ .



After the crystallization began, a reduction in the percentage of solid recovered was observed, showing that the formation of the amorphous precipitates initially occurred through the condensation reaction, dissolved species, and direct transformation of these precipitates into crystalline zeolite in a template-free route. This means that the agglomerated precipitates act as chemical or structural precursors for zeolite formation during the lithium extraction process <sup>[14]</sup>.

The relative crystallinity of the solid product decreased dramatically in the range of 36 h to 48 h with Na<sub>2</sub>O, which was probably caused by the decomposition of the MFI-type zeolite because its stability range was shorter in the template-free system than that in systems containing structures, and the solid product transformed into more stable phases, i.e., mordenite and quartz.

From the crystallization curves, it was possible to calculate the activation energy for the nucleation stage by considering the partial curves at the point of greater crystallinity for the nucleation rate dependence on the temperature according to Eqs. (C) and (D) <sup>[15]</sup>:

$$\ln\left(\frac{1}{t_i}\right) = \ln A_i - \frac{E_i}{RT} \quad (C) \qquad k = Ae^{-E_i/RT} \quad (D)$$

where 't<sub>i</sub>' is the induction time, 'k' is a constant for velocity, 'A' is the frequency factor or pre-exponential factor, 'E<sub>i</sub>' is the apparent activation energy for the nucleation period, 'R' is the gas constant and 'T' is the absolute temperature.

The frequency factor 'A' represents the frequency of collisions between the molecules in the reaction medium. The factor 'exp(-E<sub>i</sub>/RT)' represents the fraction of molecular collisions that have energy equal to or greater than the activation energy. By adjusting the crystallization curves by the Avrami-Erofeev Eq. (D), the crystal growth rate and the activation energy can be calculated by the Avrami-Kholmogorov Eq. (E) <sup>[16]</sup>:

$$a = 1 - e^{-k(t-t_i)^n} \quad (E)$$

where 'a' is the degree of crystallinity, 't' is the total time (nucleation period + crystal growth period), and 'n' is a constant empirical exponent.

The apparent activation energy 'E<sub>i</sub>' was calculated from ln k vs. 1.T<sup>-1</sup> with the activation energy parameters and pre-exponential factor (Fig. 10, Tab. 2).

For situations of slow or moderate crystallization, Mintova and Valtchev describe the transition period as an intermediate of nucleation and crystallization, and chose an arbitrary point corresponding to 15% of the crystallinity to be the upper limit of the transition period for crystallization curves obtained at different temperatures <sup>[17]</sup>.

Thus, the crystallization rate corresponds to the steep slope in the crystallization curve (Fig. 10a), and the inflection points are determined by the rearrangement of the first derivative of Eq. (D) in terms of 'n', 'k' and 'a' (Eq. E) and are plotted as a function of 'ln(-ln(1-a))' vs. 'ln(t)' (Fig. 10b).

Figure 10. Crystallization curves (a) and plot of  $\ln(-\ln(1-a))$  vs.  $\ln(t)$  for the isothermal experiments (b) for MFI zeolite with  $\text{Na}_2\text{O}/\text{SiO}_2$  molar ratios 0.13, 0.19 and 0.26.

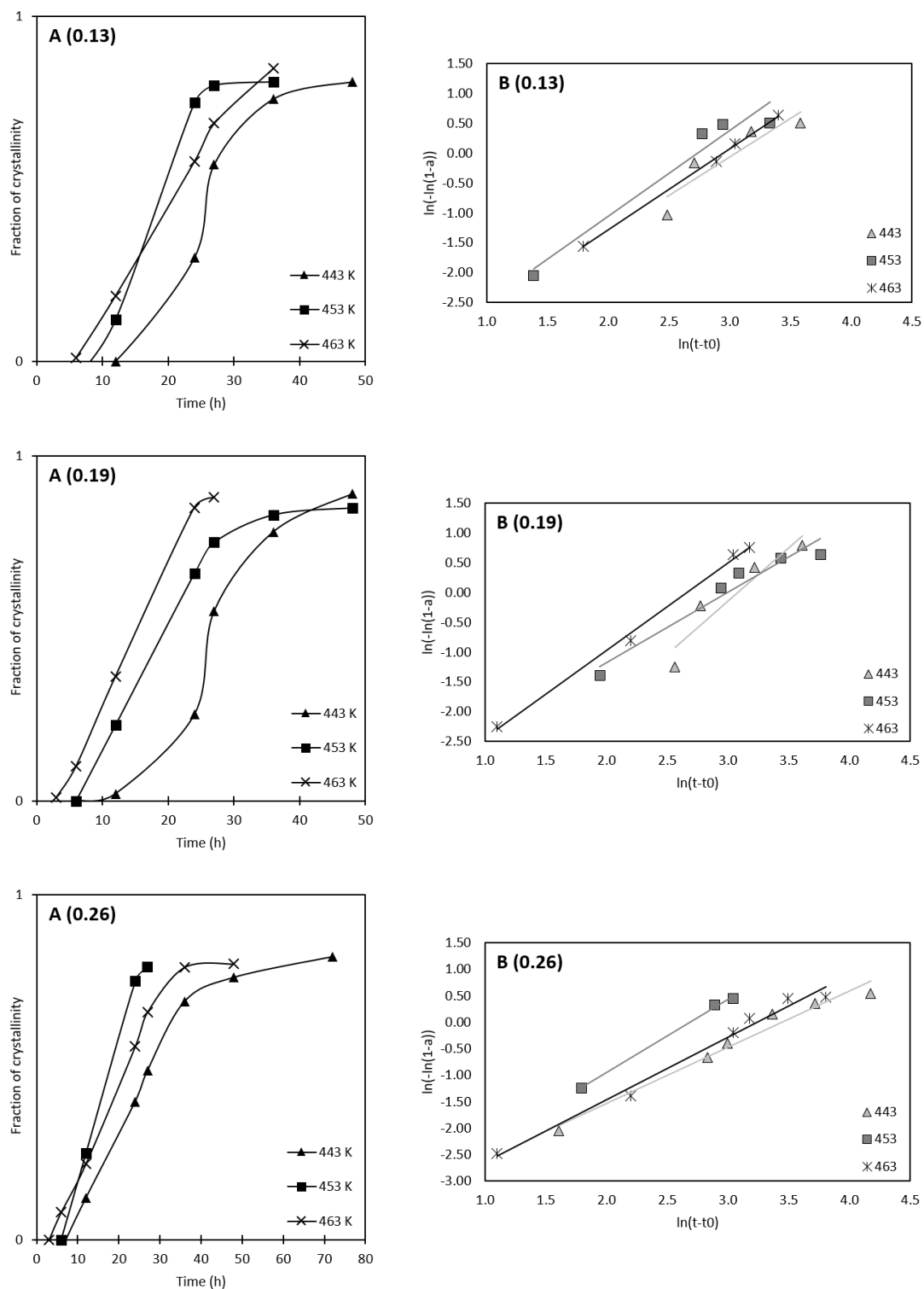


Table 2. Modified parameters for MFI-type zeolite at different crystallization temperatures and Na<sub>2</sub>O/SiO<sub>2</sub> molar ratios. Induction period ( $t_o$ ); nucleation rate ( $V_i$ ).

Na <sub>2</sub> O/SiO <sub>2</sub> molar ratio	T (K)	$t_o$ (h)	$V_i$ (h <sup>-1</sup> )	$\ln k$	$n$	$R$	-1/T	$\ln (V_i)$
0.13	443	12	0.083	-3.976	1.294	0.827	-2.26	-2.48
	453	8	0.125	-3.930	1.930	0.948	-2.21	-2.08
	463	6	0.167	-4.008	1.360	0.998	-2.16	-1.79
0.19	443	11	0.091	-3.976	1.294	0.817	-2.26	-2.40
	453	5	0.200	-3.534	1.179	0.942	-2.21	-1.61
	463	3	0.333	-3.921	1.473	0.996	-2.16	-1.10
0.26	443	7	0.143	-3.976	1.294	0.817	-2.26	-1.95
	453	6	0.167	-3.712	1.380	0.998	-2.21	-1.79
	463	3	0.333	-3.818	1.179	0.985	-2.16	-1.10

As shown in Tab. 2, for a low Na<sub>2</sub>O content, there is a long period of induction ( $t_o$ ). However, the crystallization rate ( $V_i$ ) slightly increased with an increase in Na<sub>2</sub>O at 443 K and 453 K, showing that in the absence of an organic template, it is difficult to obtain pentasil groups for an MFI-type zeolite with an increase in the reaction temperature.

The dependence of the crystallization temperature becomes most significant for a Na<sub>2</sub>O/SiO<sub>2</sub> molar ratio of 0.26, as shown in the 4th column ( $V_i$ ) of Tab. 2. This means that an increase in Na<sub>2</sub>O was favored over an increase in temperature.

The pre-exponential frequency factor ' $A_i$ ' can be obtained from the velocity constant ' $k$ ' (Fig. 11, Tab. 3).

Figure 11. Arrhenius plots for the calculation of the activation energy (E) for a) nucleation and b) the crystal growth process.

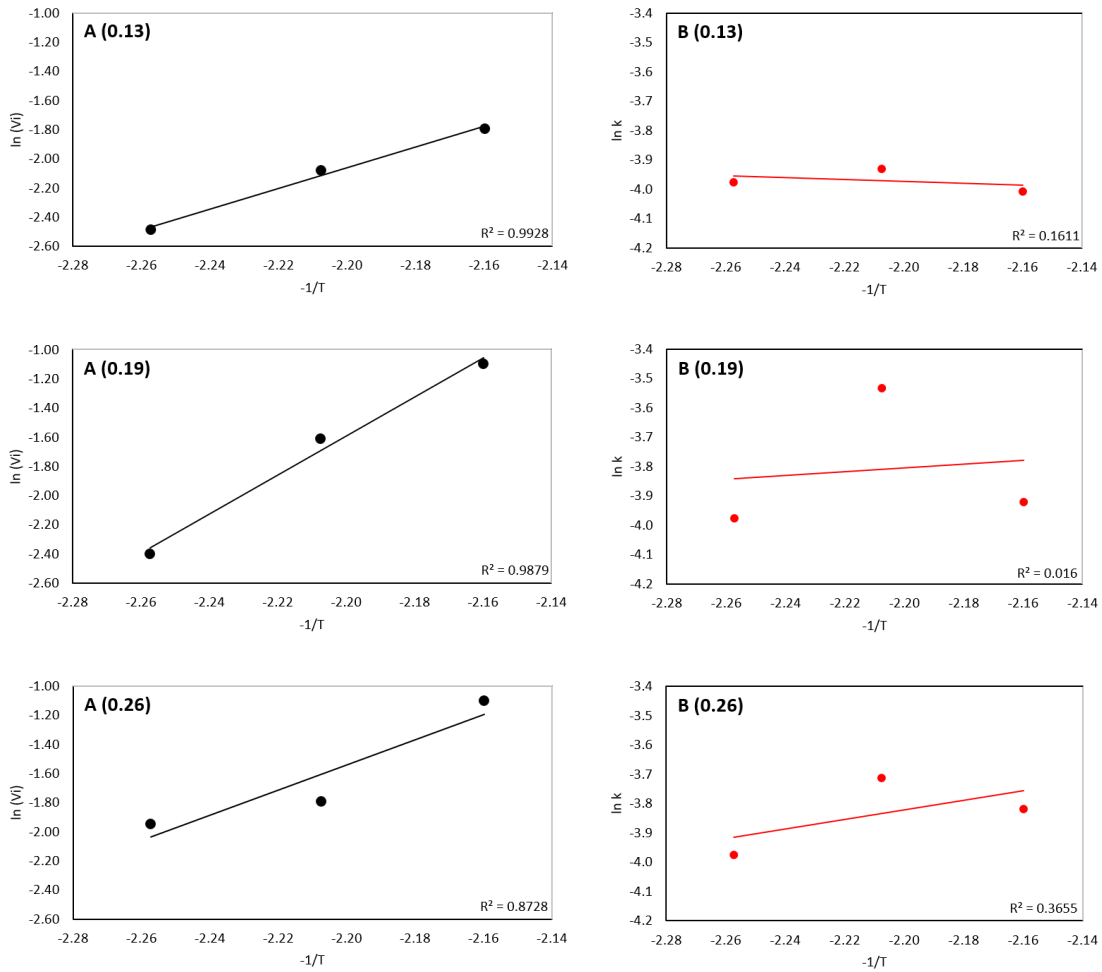


Table 3. Activation energy (E) and pre-exponential factor (A) for nucleation (n) and crystal growth (cg) in MFI-type zeolite crystallization.

Na <sub>2</sub> O/SiO <sub>2</sub> molar ratio	E <sub>n</sub> (kJ/mol)	ln A <sub>n</sub>	E <sub>cg</sub> (kJ/mol)	ln A <sub>cg</sub>	∑E (kJ/mol)	∑ln A
0.13	59.165	13.596	-2.710	-4.691	56.455	8.905
0.19	110.942	27.763	5.200	-2.429	116.142	25.334
0.26	71.894	17.483	13.658	-0.208	85.552	17.275

Tab. 3 shows that the activation energy for the nucleation stage (E<sub>n</sub>) is higher with a Na<sub>2</sub>O/SiO<sub>2</sub> molar ratio of 0.19, which can be attributed to the higher frequency of interactions between reactive species during this stage, as indicated by the higher number of pre-exponential factors, 'A<sub>n</sub>'.

In all cases, there was higher energetic consumption in the induction phase for the materials formed than that during the growth period of the crystals. According to Watson et al., the apparent activation energy for a template-free MFI-type zeolite is approximately 70 kJ/mol. This value corresponds to processes with controlled crystal growth that involve units of  $(\text{AlO}_4)^{-5}$  and  $(\text{SiO}_4)^{-4}$  next to the growth surfaces by means of condensation polymerization and elimination of water between pairs of OH groups [18].

The energy values involved during the nucleation and crystal growth stages differ little in relation to the literature, and according to Kim et al., the values are 113.6 kJ/mol and 80.8 kJ/mol, respectively, in regard to MFI-type zeolite with SAR = 33, which is similar to the LPM-18 obtained in this study (0.19Na<sub>2</sub>O:0.034Al<sub>2</sub>O<sub>3</sub>:SiO<sub>2</sub>:30H<sub>2</sub>O molar ratio) [15]. The discrepancy can be explained by the chemical composition of the starting material used (beta-spodumene) and the different synthesis conditions.

Adsorption and desorption of N<sub>2</sub> on LPM-18.

It was possible to calculate the relative crystallinity of the samples and the average size of the crystallites from the diffractograms of the samples obtained after hydrothermal treatment for 24 h, 27 h and 96 h, as shown in Tab. 4.

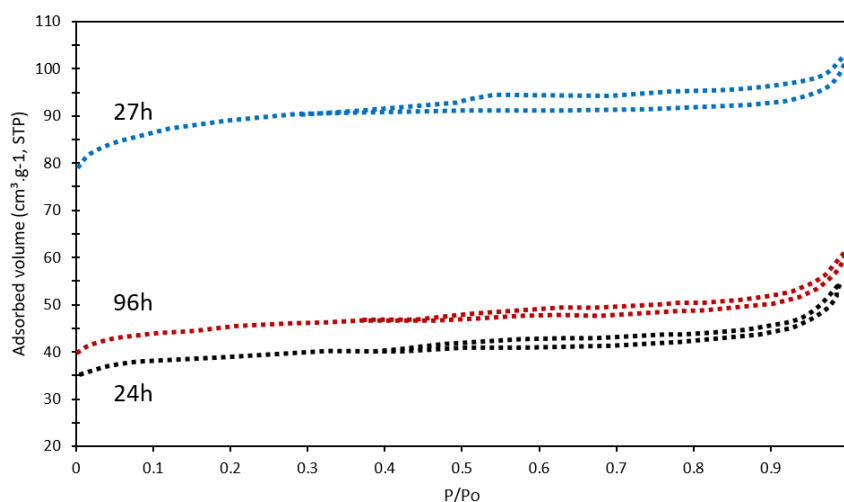
The highest crystallinity sample, which was normalized to 100% crystallinity, was for 27 h of treatment. From the XRD data and using the Scherrer equation, the mean size of the crystalline domains of the synthesized materials was calculated. The average crystallite size remains approximately 184 Å, which is slightly larger than 188.1 Å for the sample synthesized for 27 h. It is possible that the larger crystallites were due to the absence of a codirecting structure; therefore, they help reduce their mean size [19].

Table 4: Physicochemical properties of the synthesized samples with 0.19Na<sub>2</sub>O:0.034Al<sub>2</sub>O<sub>3</sub>:SiO<sub>2</sub>:30H<sub>2</sub>O molar ratio.

Crystallization time	Relative crystallinity	BET surface area	Crystallite size	V <sub>mic</sub>	V <sub>mes</sub>
h	%	m <sup>2</sup> .g <sup>-1</sup>	Å	cm <sup>3</sup> .g <sup>-1</sup>	cm <sup>3</sup> .g <sup>-1</sup>
24	46.1	126.0	180.5	0.034	0.024
27	100.0	306.3	188.1	0.126	0.026
96	66.9	148.2	183.6	0.055	0.033

The texture properties of the samples were analyzed by adsorption/desorption isotherms of N<sub>2</sub> at 77 K, as shown in Fig. 12. According to the IUPAC classification for porous solid materials, the N<sub>2</sub> adsorption and desorption isotherms of the analyzed materials were classified as a combination of type I isotherms, which are characteristic of microporous adsorbents, and type IV isotherms, which are characteristic of mesoporous solids with the presence of a hysteresis loop [20].

Figure 12. N<sub>2</sub> adsorption isotherms of the LPM-18 support synthesized in 24 h, 27 h, and 96 h.



All samples presented hysteresis for values of relative pressure above 0.35, which can be attributed to the presence of mesopores in the structures and was confirmed by the pore volume values in Tab. 4 [21].

The adsorption isotherms, specific area (BET method), micropore volume (t-plot method) and mesopore volume (BJH method) were calculated and are shown in Tab. 4. All samples had a specific area greater than 120 m<sup>2</sup>.g<sup>-1</sup>. The longer the crystallization time was, the greater the specific surface area of the zeolite was, which also increased with increasing SAR value in the synthesis [22].

This effect can be observed by comparing the specific surface areas of the samples synthesized at 96 h and 27 h, which were 148.2 and 306.3 m<sup>2</sup>.g<sup>-1</sup>, respectively. In addition, the sample with the highest specific surface area was also the sample with the highest relative crystallinity, indicating that the specific surface is both larger and more crystalline than that of the other samples [23].

The other samples presented lower specific areas due to lower crystallinity and possibly the presence of amorphous material. The presence of mesopores was characterized by the hysteresis loop in the adsorption isotherms. As evidenced by the volume of the mesopores, and the larger the volume of mesopores was, the larger the external area was [21].

The previous calcination of the samples to their protonated form inhibits sodium atoms from blocking the pores from molecules of  $N_2$ , which could result in less adsorption and consequently a smaller specific area of the sodium form of the sample. However, confirmation of this hypothesis would require elementary chemical analysis [21].

Measurement of the acidity of LPM-18 (Na-form vs H-form).

Fig. 13 shows the TGA/DTG curves of the Na-LPM-18, H-LPM-18 and commercial ZSM-5 (SAR = 26) samples obtained in the temperature range between 323-873 K. The TGA/DTG curves were used to calculate the acidic properties of the zeolite active sites (Tab. 5).

Figure 13. TGA/DTG curves of n-butylamine desorption from LPM-18 and commercial ZSM-5.

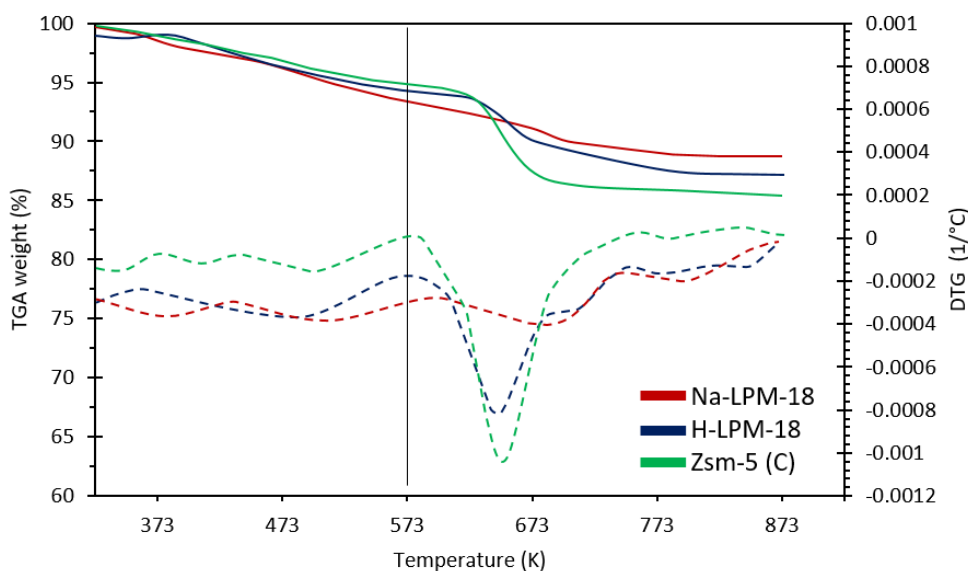


Table 5. Acidity properties of n-butylamine desorption on LPM-18 (T. range 323-873 K).

Samples	Desorption	Concentration of acid sites (mmol.g <sup>-1</sup> )		
	$\Delta m$ (%)	< 573 K	> 573 K	Totals
H-ZSM-5 (C)	15.4	0.44	1.11	1.55
Na-LPM-18	11.2	0.77	0.64	1.41
H-LPM-18	13.1	0.56	0.87	1.43

The acidic strength of the materials was classified as medium (< 573 K) and strong (> 573 K). The concentration of total acid sites was proportional to the desorption of n-butylamine and defined as the total density of the acid sites. The LPM-18 showed similar behavior to H-ZSM-5 (C) compared to the protonated form for the concentration of total acid sites. The H-ZSM-5 (C) presented superior and relevant concentrations of strong acid sites, which were possibly proportional to the Brönsted proton acidity.

The TGA/DTG curves of the materials in their protonated form showed similar profiles for the mass loss steps. For H-LPM-18, although the total concentration of acidic sites did not match the commercial concentration, a concentration of relevant and close strong commercial acid sites was presented. According to Kim et al. (2010), the concentration of total acid sites in MFI-ZSM-5-type zeolites is inversely proportional to the SAR [24].

Thus, the concentration of total H-ZSM-5 (C) acid sites is higher because it has SAR = 26 compared to SAR = 18 for zeolite LPM-18. This means that the lower the SAR is, the greater the number of aluminum ions in the crystalline lattice is; consequently, the greater the number of compensation cations bound to the aluminum ions is and the greater the possibility of Brönsted acid sites is since the compensation cations can be replaced isomorphically by H<sup>+</sup> protons through ion exchange.

The total acid concentration index for H-LPM-18 was equivalent to that reported by Engtrakul et al. (2016) for H-ZSM-5 (SAR = 30) in the temperature range 423-723 K with an acidity of 1.35 mmol g<sup>-1</sup> [25].

## Conclusions

Experimental studies with dealuminated beta-spodumene showed that it is possible to extract almost 85% Li if the concentrate is processed under synthetic conditions, i.e., beta-spodumene concentrated with Na<sub>2</sub>CO<sub>3</sub> and NaCl at 923 K in a

thermal cycle with a duration of less than 48 h, sodium hydrothermal treatment in a reaction mixture with 0.11Na<sub>2</sub>O:0.034 Al<sub>2</sub>O<sub>3</sub>:SiO<sub>2</sub>:30H<sub>2</sub>O molar ratio and leaching with NH<sub>4</sub>HCO<sub>3</sub> at 313 K for 60 min.

The decrease in the molar ratio of Na<sub>2</sub>O/SiO<sub>2</sub> from 0.19 to 0.10 had practically no influence on lithium extraction, while a decrease in temperature from 463 K to 443 K during hydrothermal treatment resulted in a 15% reduction in the relative crystallinity of LPM-18.

By evaluating the total acidity of the H-LPM-18 material by thermodesorption (n-butylamine), the density and strength of the acid sites could be determined and correlated with the results obtained with the SAR, as reported in the literature.

The results obtained in this work show that the LPM-18 zeolite obtained via a template-free lithium extraction route is promising for application in refining processes or as a catalytic support since its synthesis reduces the environmental impacts and costs of production.

## Acknowledgments

This study was financed in part by the Coordenação de Aperfeiçoamento de Pessoal de Nível Superior - Brazil (CAPES) - finance code 001. The authors would like to thank Companhia Brasileira de Lítio - Brazil (CBL), for the beta-spodumene samples and the Instituto de Tecnología Química - Spain (ITQ), for the characterization of the materials.

## References

- [1] MARTIN, G., RENTSCH, L., HOECK, M., & BERTAU, M.; Lithium market research—global supply, future demand and price development. **Energy Storage Materials**, 6 (2017), p. 171-179.
- [2] RONGGUO, C., JUAN, G., LIWEN, Y., HUY, D., LIEDTKE, M.; **Supply and demand of lithium and gallium**, Hannover: BGR. 2016.
- [3] TAYLOR, R. G.; **Geology of tin deposits** (Vol. 11), Elsevier. 2014.
- [4] KUANG, G., LIU, Y., LI, H., XING, S., LI, F., & GUO, H.; Extraction of lithium from β-spodumene using sodium sulfate solution. **Hydrometallurgy**, 177 (2018), p. 49-56.
- [5] OLIVEIRA, M. S. M., NASCIMENTO, R. M., PERGHER, S. B. C.; **Síntese do**

- material zeolítico LPM-12 de tipologia EDI a partir do resíduo silicoaluminoso gerado na extração do lítio do espodumênio.** BR Patent No 10,2017,016757,7. 2017.
- [6] QIN, Z., CYCHOSZ, K. A., MELINTE, G., EL SIBLANI, H., GILSON, J. P., THOMMES, M., FERNANDEZ, C., MINTOVA, S., ERSEN, O., & VALTCHEV, V.; Opening the cages of faujasite-type zeolite. **J. Am. Chem. Soc.**, 139.48 (2017), p. 17273-17276.
- [7] GHRIB, Y., FRINI-SRASRA, N., SRASRA, E., MARTÍNEZ-TRIGUERO, J., & CORMA, A.; Synthesis of cocrystallized USY/ZSM-5 zeolites from kaolin and its use as fluid catalytic cracking catalysts. **Catal. Sci. Technol.**, 8.3 (2018), p. 716-725.
- [8] SANG, S., CHANG, F., LIU, Z., HE, C., HE, Y., & XU, L.; Difference of ZSM-5 zeolites synthesized with various templates. **Catalysis Today**, 93 (2004), p. 729-734.
- [9] AKAH, A.; Application of rare earths in fluid catalytic cracking: A review. **J. Rare Earths**, 35.10 (2017), p. 941-956.
- [10] SANTOS, L. L., NASCIMENTO, R. M., PERGHER, S. B. C.; **Processo para obtenção dos materiais LPM-18 e LPM-19, com topologias zeolíticas MFI e LTT, respectivamente, como subproduto da extração do lítio a partir do beta-espodumênio.** BR Patent No 10,2018,016339,6. 2018.
- [11] **ASTM D 5758-01** (p. 1-4). In: Annual Book of ASTM Standards. 2015.
- [12] BARBOSA, L. I., VALENTE, G., OROSCO, R. P., & GONZALEZ, J. A.; Lithium extraction from  $\beta$ -spodumene through chlorination with chlorine gas. **Minerals Engineering**, 56 (2014), p. 29-34.
- [13] ROSALES, G. D., DEL CARMEN RUIZ, M., & RODRIGUEZ, M. H.; Alkaline metal fluoride synthesis as a subproduct of  $\beta$ -spodumene leaching. **Hydrometallurgy**, 139 (2013), p. 73-78.
- [14] KANG, N. Y., SONG, B. S., LEE, C. W., CHOI, W. C., YOON, K. B., & PARK, Y. K.; The effect of Na<sub>2</sub>SO<sub>4</sub> salt on the synthesis of ZSM-5 by template free crystallization method. **Micropor. Mesopor. Mat.**, 118.1-3 (2009), p. 361-372.
- [15] KIM, S. D., NOH, S. H., SEONG, K. H., & KIM, W. J.; Compositional and kinetic study on the rapid crystallization of ZSM-5 in the absence of organic template under stirring. **Micropor. Mesopor. Mat.**, 72.1-3 (2004), p. 185-192.

- [16] GUALTIERI, A., NORBY, P., ARTIOLI, G., & HANSON, J.; Kinetics of formation of zeolite Na-A [LTA] from natural kaolinites. **Phys. Chem. Miner.**, 24.3 (1997), p. 191-199.
- [17] MAJANO, G., DELMOTTE, L., VALTCHEV, V., & MINTOVA, S.; Al-rich zeolite beta by seeding in the absence of organic template. **Chemistry of Materials**, 21.18 (2009), p. 4184-4191.
- [18] WATSON, J. N., ITON, L. E., KEIR, R. I., THOMAS, J. C., DOWLING, T. L., & WHITE, J. W.; TPA-silicalite crystallization from homogeneous solution: kinetics and mechanism of nucleation and growth. **J. Phys. Chem B.**, 101.48 (1997), p. 10094-10104.
- [19] FERNANDEZ, S. C., LAU, L. Y., & NOGUEIRA, L. **Processo de preparação de zeólita sintética com estrutura tipo ZSM-5**. BR Patent No 8606367-7. 1986.
- [20] CHAE, H. K., SIBERIO-PEREZ, D. Y., KIM, J., GO, Y., EDDAOUDI, M., MATZGER, A. J., O'KEEFFE, M., & YAGHI, O. M.; A route to high surface area, porosity and inclusion of large molecules in crystals. **Nature**, 427.6974 (2004), p. 523-527.
- [21] YU, Q., MENG, X., LIU, J., LI, C., & CUI, Q.; A fast organic template-free, ZSM-11 seed-assisted synthesis of ZSM-5 with good performance in methanol-to-olefin. **Micropor. Mesopor. Mat.**, 181 (2013), p. 192-200.
- [22] WU, G., WU, W., WANG, X., ZAN, W., WANG, W., & LI, C.; Nanosized ZSM-5 zeolites: Seed-induced synthesis and the relation between the physicochemical properties and the catalytic performance in the alkylation of naphthalene. **Micropor. Mesopor. Mat.**, 180 (2013), p. 187-195.
- [23] MOHAMED, M. M., ZIDAN, F. I., & THABET, M.; Synthesis of ZSM-5 zeolite from rice husk ash: Characterization and implications for photocatalytic degradation catalysts. **Micropor. Mesopor. Mat.**, 108.1-3 (2008), p. 193-203.
- [24] KIM, Y. T., JUNG, K. D., & PARK, E. D.; Gas-phase dehydration of glycerol over ZSM-5 catalysts. **Micropor. Mesopor. Mat.**, 131.1-3 (2010), p. 28-36.
- [25] ENGTRAKUL, C., MUKARAKATE, C., STARACE, A. K., MAGRINI, K. A., ROGERS, A. K., & YUNG, M. M.; Effect of ZSM-5 acidity on aromatic product selectivity during upgrading of pine pyrolysis vapors. **Catalysis Today**, 269 (2016), p. 175-181.

## Chapter 7. Channel and cage-type zeolites obtained in lithium extraction route

---

Leonardo L. dos Santos<sup>1</sup>; Rubens M. do Nascimento<sup>1</sup>; Sibebe B. C. Pergher<sup>2</sup>

<sup>1</sup> Department of Materials Science and Engineering, Federal University of Rio Grande do Norte, Natal 59078-97, Brazil.

<sup>2</sup> Department of Chemistry, Laboratório de Peneiras Moleculares, Federal University of Rio Grande do Norte, Natal 59078-97, Brazil.

**Abstract:** The production of  $\text{Li}_2\text{CO}_3$  involves acid route extraction, resolubilization, and carbonate recrystallization, as well as the abundant formation of Si- and Al-rich residues, which are generally associated with sulfates and organic compounds. The viability of the process depends on the recovered lithium yield and minimized formation of residues, or viability can depend on obtaining a byproduct of commercial value, for example, zeolites, through optimization in the extraction process. In this study, the characteristics and properties of the zeolites obtained as byproducts in the lithium extraction process were evaluated, correlating their topologies with the suggested extraction method. The route used to recover lithium from  $\text{Li}_2\text{CO}_3$  production consisted of the hydrothermal treatment of beta-spodumene (2.98% Li) in contact with sodium salts, as well as solubilization, precipitation with ammonium ion bicarbonate, filtration, and purification of the solution for recovery of zeolites as byproducts of the process. The recovered lithium yield was 80% in  $\text{Al}(\text{OH})_3$  solubilization at 363 K/6 h and FAU topology zeolites were obtained: LPM16-X (SAR = 2.1) or LPM16-Y (SAR = 4.5), and the recovered lithium yield was 70% in solubilization with silica aerosil at 423 K/48 h to obtain a zeolite with MOR topology: LPM17 (SAR = 13.6). Considering the structural differences of the zeolites formed (channel- and cage-type), the adsorption activities were explored to clarify the relationships between structure, kinetics and adsorption capacity. The cage-type zeolite LPM16-Y presented promising performance as a potential adsorbent of  $\text{CH}_4$  and  $\text{CO}_2$ .

**Keywords:** Li-extraction. Byproduct. Zeolite. Cage-type. Channel-type. Kinetic. Adsorption.

## Introduction

The processing of lithium-containing aluminosilicates is based on the decomposition of lithium minerals during heating or solubilization with chemical additives, accompanied by acid leaching and hydrothermal treatment of the products obtained, usually  $\text{Li}_2\text{CO}_3$  [1, 2].

Several routes are described in the literature for extraction and recovery of lithium from beta-spodumene, but in no case is there a byproduct with characteristics and properties of zeolite [3-6]. Typically, aluminosilicate residue, rich in Si and Al, is obtained, as is any remaining lithium in the form of an exchangeable ion, which is treated postextraction for the synthesis of zeolites [7, 8].

Zeolites are potential adsorbents because of the ability of their microporous structures to adsorb molecules at relatively low pressures extensively used in industries as adsorbents for gas separation of  $\text{CH}_4$ ,  $\text{NH}_3$ ,  $\text{H}_2\text{S}$ ,  $\text{N}_2$ ,  $\text{O}_2$  and  $\text{CO}_2$  [9-11].

It is important to note that for different structural frameworks, there are distinct adsorption characteristics. Although many studies have been carried out involving microporous zeolites, e.g., FAU topology zeolites, the relationship between structure, adsorptive characteristics and physicochemical properties still needs to be better clarified, especially in the adsorption of gases at room temperature or at slightly higher temperatures [12].

The adsorption of gases in different adsorbents and the comparison of the adsorption properties are of great importance in the understanding of the adsorption process, especially in the areas of gas separation and purification and adsorbent gas storage. Factors such as SAR (Si/Al ratio) and crystallinity may affect gas adsorption characteristics as well as pore size and volume properties, surface area and unit cell parameters, while adsorbates may also affect these characteristics [10].

The kinetic diameter of the adsorbents determines the accessibility and type of diffusion occurring within the pore, while the formal charge and polarity determine the interaction force between the adsorbate and the zeolite [13]. Thus, it is important to understand how different structures (channel and cage-type zeolites) respond to different types of adsorbents.

In this study, the properties of the zeolites obtained as a byproduct in a lithium extraction route were evaluated in an attempt to relate the synthesis parameters to the pore network system, pore size and volume, surface area, composition (Si, Al, and Na) and gas

adsorption characteristics.

To understand the differences between the zeolites obtained, characterizations were made to determine their physicochemical structures and properties. Using methane (CH<sub>4</sub>) and carbon dioxide (CO<sub>2</sub>) as adsorbents, gas adsorption measurements were performed to determine the adsorption capacity and isotherms, as well as the rate of consumption.

## Experimental

Raw materials.

Beta-spodumene was supplied by Companhia Brasileira de Lítio (CBL), with chemical composition shown in Table 1, with a Si/Al molar ratio = 2.6. Carbonate and sodium hydroxide, aluminum hydroxide, silica aerosil and ammonium bicarbonate were of analytical quality without any further purification.

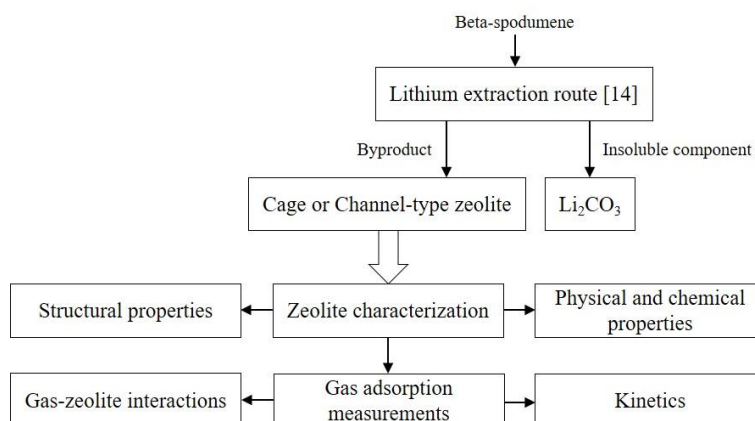
Table 1. Chemical analysis of the beta-spodumene sample (wt%).

Component	SiO <sub>2</sub>	Al <sub>2</sub> O <sub>3</sub>	Li <sub>2</sub> O	Fe <sub>2</sub> O <sub>3</sub>	K <sub>2</sub> O	Others
Content (%)	68.97	22.31	6.43	0.92	0.42	< 0.40

Procedures.

The experimental procedures in this study evaluated the lithium extraction route zeolites, and zeolite characterization and gas adsorption measurements with CH<sub>4</sub> and CO<sub>2</sub> were performed. The synthesis methodologies were based on the literature [14]. Fig. 1 shows the flowchart adopted for the study.

Figure 1. Flowchart of the experimental procedures used in the study.



Obtaining cage-type zeolites in the lithium extraction route.

Initially, 1.0 g of beta-spodumene was dissolved in 50 mL of 0.75 mol.L<sup>-1</sup> NaOH solution and refluxed. The mixture was poured into a system formed by 3.0 g Al(OH)<sub>3</sub> + 1.0 g Na<sub>2</sub>CO<sub>3</sub> dissolved in 50 mL of 2.0 mol.L<sup>-1</sup> NaOH solution. Finally, the new mixture was autoclaved in static mode at 90°C for 6 h. It was then solubilized with NH<sub>4</sub>HCO<sub>3</sub> in sufficient quantity to maintain the pH > 10.

At filtration, the cloudy solution was separated from the supernatant (saturated with Li<sub>2</sub>CO<sub>3</sub>, approximately 80% Li) and oven dried at 60°C overnight. The recovered material is substantially formed by crystals characteristic of NaX zeolite (SAR = 2.1), designated LPM16-X, or NaY (SAR = 4.5), designated LPM16-Y when 1.8 g of Al(OH)<sub>3</sub> was used.

Obtaining channel-type zeolite in the lithium extraction route.

Initially, 1.0 g beta-spodumene was dissolved in 50 mL of 1.2 mol.L<sup>-1</sup> NaOH solution and refluxed. In that mixture, 21.4 g of silica aerosil and the autoclaved gel (static mode) were added at 150°C for 48 h. The cloudy solution obtained in the filtration was separated from the supernatant (saturated with Li<sub>2</sub>CO<sub>3</sub>, approximately 70% Li) and subjected to oven drying at 60°C overnight. The recovered material (LPM17) is substantially formed by crystals characteristic of Na-MOR zeolite (SAR = 13.6).

Characterizations.

In the description of the structural properties of the zeolites, the XRD (PANalytical CUBIX, X'Celerator), SEM (*JEOL, JSM 6300* model with *Link-Isis*) and FT-IR (*Nicolet 710 FT-IR* Spectrometer) characterization methods were used to facilitate the understanding of the adsorption and gas-zeolite interaction characteristics. The intensities of the selected diffraction peaks of a particular sample were compared to the intensity of the same peak of a commercial standard sample for calculation of relative crystallinity <sup>[15]</sup>.

To determine the physicochemical properties of microporous solids, the specific surface area, micropore volume, mesopore and macropore volume, pore size, and distribution for each zeolite were determined from N<sub>2</sub> adsorption data (Micromeritics, Model TriStar 3000) and the BET equation. The surface area (BET method) and the average pore diameters for the zeolite samples (BJH adsorption) were calculated by the ASAP 2020 physisorption analyzer's built-in software.

Each zeolite was subjected to vacuum pretreatment at a temperature of 673 K/2 h for removal of water and other sorbed materials in the pore or channel. Subsequently, each solid was weighed in a sample tube, cooled to 77 K (liquid nitrogen temperature), with the nitrogen gas introduced at low pressure (gradually increasing to 1 bar) and the volume of gas adsorbed at equilibrium ( $\text{cm}^3 \cdot \text{g}^{-1}$ ) recorded against the partial pressure of the adsorbate ( $P/P_0$ ).

To determine the characteristics of the adsorption of gas in the zeolites, two types of adsorbates were used, methane ( $\text{CH}_4$ ) and carbon dioxide ( $\text{CO}_2$ ), for analysis through capacity measurements (gravimetric method using thermal gravimetric analyzer – PerkinElmer, TGA), rate and isotherms of gas adsorption (298 K), and gas-solid interactions <sup>[16]</sup>.

The amount of adsorbed gas was measured by the difference between the initial weight (solid adsorbent) and the final weight (adsorbent + adsorbed gas) and expressed as the mol of the adsorbed gas per gram of solid adsorbent ( $\text{mmol} \cdot \text{g}^{-1}$ ).

To evaluate the potential use of the zeolites obtained, they were compared with commercially available synthetic zeolites: NaX (Aldrich Chemical), NaY and mordenite (Zeolyst International).

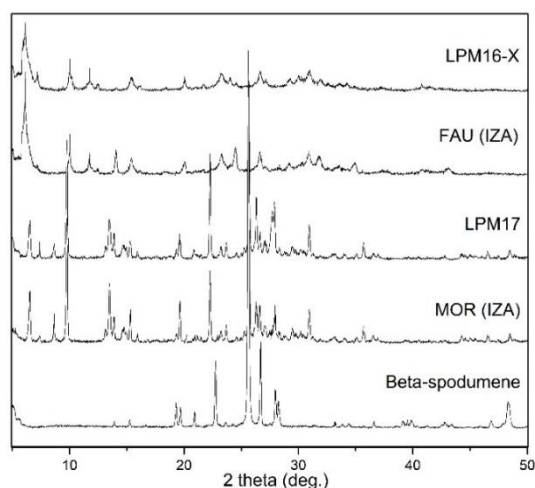
## **Results and discussion**

Structure determination.

To verify the type of structural framework for each material obtained as a byproduct in the lithium extraction route, the XRD pattern of each sample was compared to simulated standards <sup>[17]</sup>.

The diffraction patterns of the LPM16-X and LPM16-Y materials are similar to the faujasite topology, with NaX (SAR = 2.4) and NaY (SAR = 5.0) zeolite crystallites, and the patterns are similar to the mordenite topology with NaMOR (SAR = 18) zeolite crystallites for the LPM-17 material.

Figure 2. XRD patterns of the byproducts of the lithium extraction route.

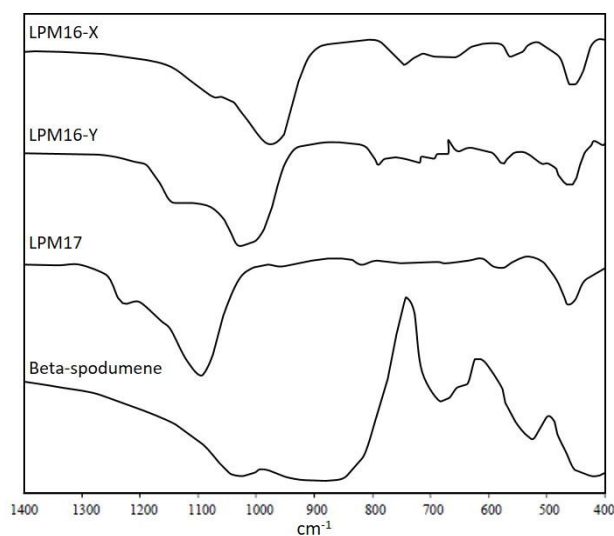


The positions of the zeolite peaks of the faujasite group are in good agreement with those reported in the IZA. Zeolites X and Y differ in chemical composition, SAR and physical-chemical properties <sup>[18]</sup>.

The samples exhibited isostructural behavior, and LPM16-X is shown in Fig. 2. The intensities indicate that the crystalline phase formation for the zeolite byproduct LPM17 was equivalent to the mordenite zeolite (IZA).

Fig. 3 shows the IR spectra of the zeolite byproducts in the 1400-400  $\text{cm}^{-1}$  region. In this region, two classes of characteristic vibrations are detected in zeolites: (i) internal, which are insensitive to structural variations and (ii) vibrations related to external connections between tetrahedra that are sensitive to the structural framework <sup>[19]</sup>.

Figure 3. FT-IR spectra of the byproducts of the lithium extraction route.



The vibrations of the bands can be assigned according to Tab. 2.

Table 2. Different structural groups from the FT-IR study of the materials.

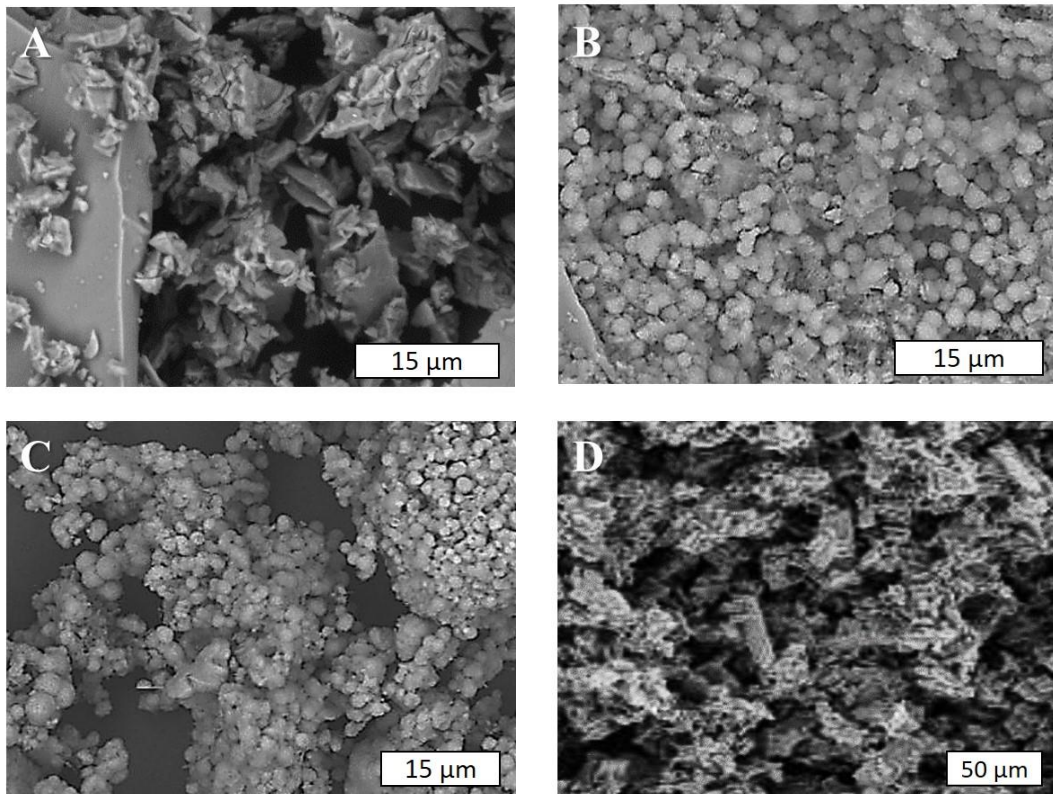
Wavenumber (cm <sup>-1</sup> )	Denotation
950-1250	T-O elongation involving movement associated with oxygen atoms, or as asymmetric elongation $\leftarrow\text{OT}\rightarrow\leftarrow\text{O}$ .
650-820	Symmetric stretching vibrations of bridge bonds – $\nu_s$ Si-O-Si and $\nu_s$ Si-O-Al.
562	Symmetric stretching vibrations of bridge bonds – $\nu_s$ Si-O-Si and bending vibrations – $\delta$ O-Si-O.
420-500	Bending vibrations – $\delta$ O-Si-O, occurring in “antiphase”, and $\delta$ O-Al-O.

The stretching band 950-1250 cm<sup>-1</sup> is SAR sensitive and is shifted to a lower frequency with increasing Al content <sup>[19]</sup>. This is shown in Fig. 3, where the highest wavenumber elongation modes are assigned to SAR = 13.6 (1097 cm<sup>-1</sup>) and SAR = 4.5 (1035 cm<sup>-1</sup>) LPM16-Y and LPM16-X of SAR = 2.1 (982 cm<sup>-1</sup>). However, the presence of a double ring is observed in the region of 540-585 cm<sup>-1</sup>, independent of SAR.

Other bands associated with the topology of the structure and attributed to the external binding modes appeared near 1050-1150 cm<sup>-1</sup> in the asymmetric stretching region.

The XRD patterns, FT-IR spectra, and morphology of the obtained materials (Fig. 4) allowed for division into two groups: (i) byproducts having an internal pore system of interconnected cavities, cage-type zeolites - LPM16-X and LPM16-Y, and (ii) byproducts providing a channel-type zeolite (LPM17) two-dimensional channel system.

Figure 4. SEM images: a) beta-spodumene; b) LPM16-X; c) LPM16-Y; and d) LPM17.



Physicochemical properties.

The experimental isotherm obtained for channel-type zeolite (LPM17), shown in Fig. 5, follows the type I isotherm. A slight slope at the end of the isotherm signifies the presence of mesoporous or external area <sup>[20]</sup>.

Adsorption isotherms for cage-type zeolites showed a rapid increase in the adsorbed amount followed by a long and near-flat region at higher pressures. However, the volume of the adsorbed phase is limited by the volume of the microporosity in which adsorption occurs <sup>[21]</sup>.

Adsorption isotherm data, the area of micropores, volume and mean pore diameter were determined and are shown in Tab. 3.

Figure 5. N<sub>2</sub> adsorption isotherms of the cage- and channel-type zeolites.

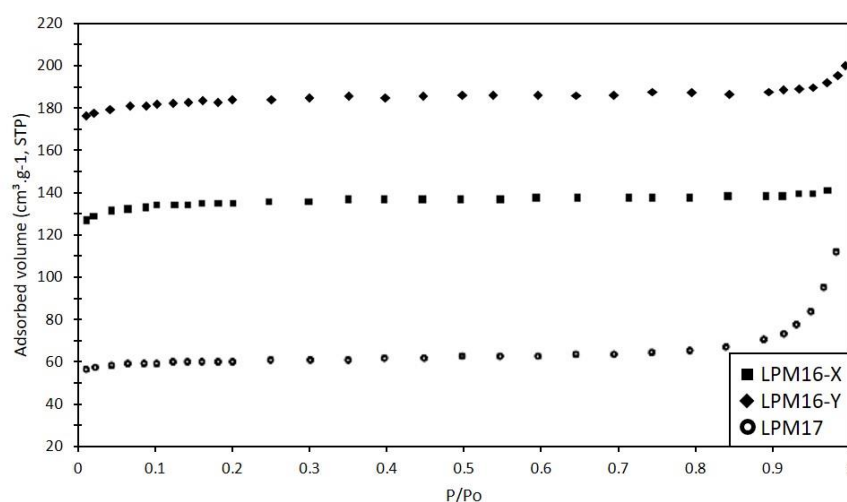


Table 3. The physical properties of the cage- and channel-type zeolites calculated from XRD data and N<sub>2</sub> adsorption data.

Materials	RC* (%)	Surface area (m <sup>2</sup> .g <sup>-1</sup> )		Pore volume (cm <sup>3</sup> .g <sup>-1</sup> )		APD** (nm)
		BET	Micropore	Micropore	Meso/Macro	
LPM16-X	79	552.4	539.5	0.20	0.022	1.48
LPM16-Y	83	833.1	808.6	0.29	0.026	1.58
LPM17	100	505.1	452.9	0.17	0.070	2.96

\*RC = Relative crystallinity; \*\*APD = Average pore diameter.

The calculated area consists of micropore area and outer surface area that provide space for adsorption of gas molecules, confirming a larger surface area for cage-type zeolites, consistent with data provided by Zeolyst International for FAU 760-885 m<sup>2</sup>.g<sup>-1</sup>.

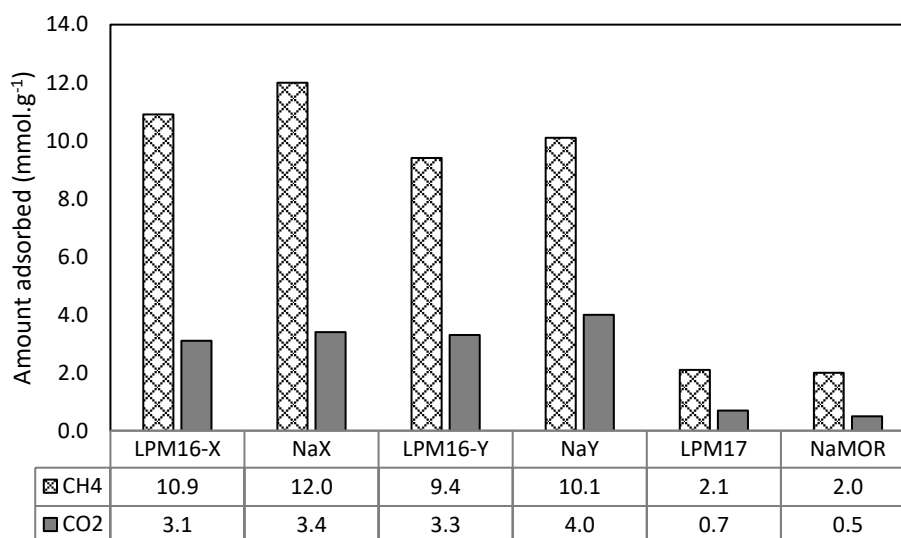
The difference is justified by the complexity of access to the surface area due to the pore blockage that leads to the low amount of nitrogen adsorbed to channel-type zeolite. The one-dimensional network of pores (MOR) finds more locks inside the pores than open three-dimensional structural structures, as in the case of faujasites, with the advantage in terms of surface area and pore volume because they provide more space for adsorbents to accumulate and absorb within the cage structure <sup>[21]</sup>.

These structures also showed a relatively smaller mean pore diameter than for channel-type zeolites, justified by the ability of faujasites to retain their microporosity. The large pore diameter is due to the presence of meso- and macropores that also contribute to the total pore volume. The average pore accounted for the sizes of micropores and meso-macropores <sup>[22]</sup>.

Gas adsorption capacity (CH<sub>4</sub> and CO<sub>2</sub>).

The adsorption capacity of the cage- and channel-type zeolites are shown in Fig. 6. The amount of adsorbates adsorbed is higher for LPM16-X > LPM16-Y > LPM17 (CH<sub>4</sub>) and LPM16-Y > LPM16-X > LPM17 (CO<sub>2</sub>).

Figure 6. CH<sub>4</sub> and CO<sub>2</sub> adsorption capacity on the cage- and channel-type zeolites (323 K, 1 bar).



The cage-type zeolite structures showed higher adsorption capacity than that of channel-type zeolite, and there are no factors that justify the adsorption capacity between adsorbates, with adsorption of CH<sub>4</sub> relatively higher than CO<sub>2</sub>. This behavior can be explained by examining the structural and physicochemical properties of the adsorbents.

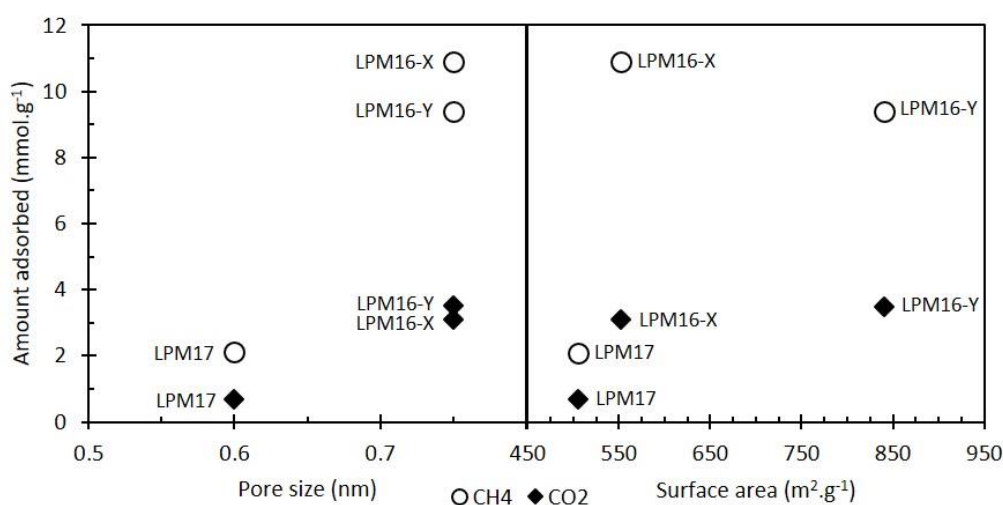
Cage-type structures demonstrate better performance than channel-type structures. This capacity may be associated with the presence of superalloys and sodalite cages that encapsulate adsorbents within the structure. However, the pore network that connects the channels and cages can affect the diffusivity of adsorbates. Any deposition within the channel can affect the diffusivity and adsorption of gas molecules <sup>[23]</sup>.

The adsorption in the parallel channel (mordenite) is considered faster than in the zig-zag channel; however, once the channel is blocked, the adsorbate finds it difficult to diffuse along the available channels <sup>[24]</sup>.

At 323 K and 1 bar, cage-type structures perform better at adsorptive capacity than channel-type structures do. In this case, more gas molecules can enter the cage, which results in high adsorptive capacity. These results agree with Garcia-Perez (2007) that cage-type structures act as storage containers for polyatomic molecules, according to pore size [25].

Fig. 7 relates the effects of pore size and surface area of the zeolites with the adsorption capacity of CH<sub>4</sub> and CO<sub>2</sub>.

Figure 7. The amount of CH<sub>4</sub> and CO<sub>2</sub> adsorbed on different zeolites as a function of pore size and surface area.



The kinetic diameters of CH<sub>4</sub> and CO<sub>2</sub> are 0.38 nm and 0.33 nm, respectively. The presence of smaller pore sizes (e.g., 0.26 x 0.57 nm for mordenite) affects the diffusivity and consequently the adsorption capacity of the adsorbates. Therefore, the molecules are expected to enter the porous network through preferential channels. The accessibility is restricted if the pore blockage occurs due to the collapse of the structure, justifying low adsorption values for several types of zeolites [26].

The faujasite structures (LPM16-X and LPM16-Y) have a higher adsorption capacity than that of channel-type zeolite (LPM17). Since the pore and cage sizes in the faujasite structure are larger than the gas molecules (0.74 nm and 1.30 nm, respectively), the problem of pore blockade is not significant. Even though the gas molecules are adsorbed into the pore opening, other gas molecules can still diffuse through the aperture and adsorb on the inner side of the cage [26].

In addition, zeolite structures are inherently flexible and readily alter symmetry or suffer distortions in response to temperature gradients or adsorbed species. The Si and O atoms that form the structure of the zeolite are thermally moving, which allows a slightly larger molecule to pass through the opening of the pores <sup>[13]</sup>.

Theoretically, high values of surface area and pore volume lead to high adsorption capacity. Although the surface area ( $833 \text{ m}^2 \cdot \text{g}^{-1}$ ) and pore volume ( $0.29 \text{ cm}^3 \cdot \text{g}^{-1}$ ) of faujasite LPM16-Y are clearly demonstrated to provide high adsorption capacity, the adsorption of mordenite LPM17 with relatively high surface area ( $505 \text{ m}^2 \cdot \text{g}^{-1}$ ) and pore volume ( $0.17 \text{ cm}^3 \cdot \text{g}^{-1}$ ) does not obey the theoretical sequence. This relationship between surface area and adsorption capacity for cage-type zeolites can be justified by the confinement effect of the structures of these zeolites <sup>[13]</sup>.

However, Derouane et al. (2000) show that confinement effects are not evident in  $\text{CO}_2$  adsorption, although surface area values for cage-type zeolites are higher than for channel-type zeolites. This difference can be attributed to the properties of the adsorbates, such as the strong interaction between the active site (adsorption site) and the permanent quadrupole moment of  $\text{CO}_2$  (pore block), interrupting the continuation of diffusion <sup>[27]</sup>.

In general, the porosity of the zeolites does not directly influence the adsorption characteristics of the gas; however, a large surface area is preferable because the formation of the internal area in a limited volume gives rise to a large number of small pores that allow adsorption to take place <sup>[13]</sup>.

In contrast, the presence of large wells allows more molecules to be confined within the cages, thereby increasing the amount adsorbed. However, there are other factors that also influence the adsorption of  $\text{CH}_4$  and  $\text{CO}_2$ : the pore wall aperture and structure, the interaction between the surface atoms and the diffusion molecules, and the way the channels are connected <sup>[26]</sup>.

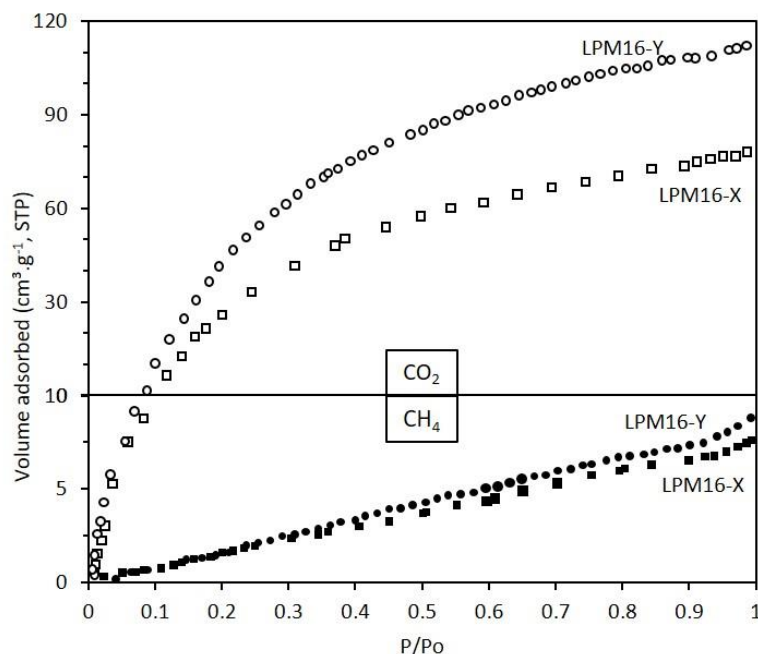
#### Adsorption Isotherms.

Fig. 8 shows the adsorption isotherms of  $\text{CH}_4$  and  $\text{CO}_2$ .

Unlike the  $\text{N}_2$  adsorption isotherm, the shape of the curves is now dependent on the type of adsorbents. The adsorption isotherms show a linear increase in the adsorption of  $\text{CH}_4$  and an abrupt increase in the adsorption of  $\text{CO}_2$  on different pressure bands, with greater adsorption of  $\text{CO}_2$  at 298 K and isotherms in the adsorption of  $\text{CH}_4$  far from saturation <sup>[28]</sup>.

The isothermal adsorption curves of Fig. 8 show that CO<sub>2</sub> has a higher affinity for adsorption than CH<sub>4</sub>, although the kinetic diameters of CH<sub>4</sub> (0.38 nm) and CO<sub>2</sub> (0.33 nm) are comparable and small enough to pass through the pore opening zeolites.

Figure 8. CH<sub>4</sub> and CO<sub>2</sub> adsorption isotherms for cage-type zeolites at 298 K.



The adsorption isotherms show that CO<sub>2</sub> adsorbs at least 10 times more than CH<sub>4</sub>. These results suggest that apolar molecules (CH<sub>4</sub>) have low adsorption affinity to cage-type zeolites and that the interaction between the permanent quadrupole moment of the CO<sub>2</sub> molecule and the electric field created by the cation is probably the reason for the greater adsorption of CO<sub>2</sub> [28, 29].

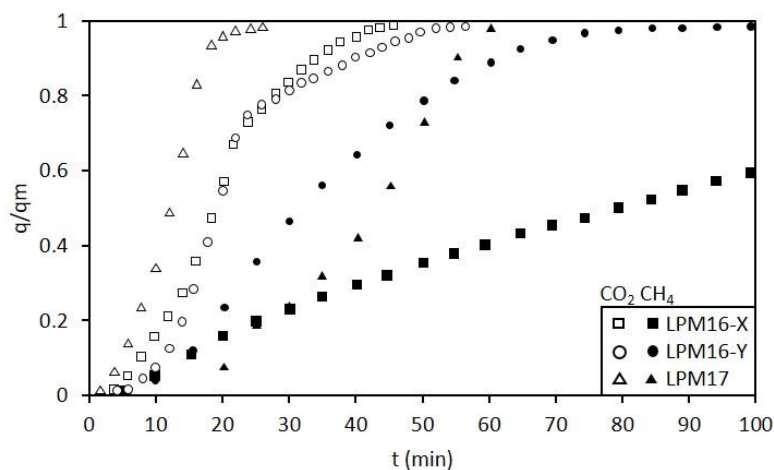
#### Adsorption kinetics.

Fig. 9 shows the adsorption curves of CH<sub>4</sub> and CO<sub>2</sub> in the cage- and channel-type zeolites, where adsorbates exhibit different adsorption behaviors as a function of time.

In the adsorption of CH<sub>4</sub> in cage-type zeolites (LPM16-X and LPM16-Y), a gradual increase with an almost linear relationship is observed. According to Fang et al. (2018), the adsorption of CH<sub>4</sub> on zeolites is best described by the relationship between the pore opening of the zeolite and the molecular size of the adsorbates. Thus, the interaction between CH<sub>4</sub> and the internal structure of the zeolite is focused more on the confinement effect than on the presence of acid sites [30].

In contrast, CO<sub>2</sub> adsorption presented a pattern described by convex curves for both groups of zeolites. At first, the rate of adsorption is relatively slow, and in the sequence, it reaches a high rate until it reaches a point where the adsorption increases slowly [28].

Figure 9. CH<sub>4</sub> and CO<sub>2</sub> fractional uptake curves of the cage- and channel-type zeolites at 323 K and 1 bar.



This factor corresponds to the adsorption at the strongest sites promoted by the quadrupole moment of CO<sub>2</sub>, followed later by the adsorption in the outermost structure [28]. For this reason, fractional adsorption curves ( $q/q_m$ ) were used, which aided in the indication that the adsorption characteristics were influenced by the structural framework and properties of the adsorbates.

The initial rate and equilibrium time data on the adsorption of CH<sub>4</sub> and CO<sub>2</sub> determined from the experimental data are summarized in Tab. 4 and plotted in Figs. 10 and 11 to observe how the molecules act towards the zeolites with different structural frameworks and physical-chemical properties, which are crucial in determining the efficiency of the adsorption process.

In the initial adsorption stage, shown in Fig. 10, the rate for LPM16-X and LPM16-Y is higher than for LPM17 for both gases. Again, for the cage-type zeolite group, LPM16-Y adsorbs faster than LPM16-X.

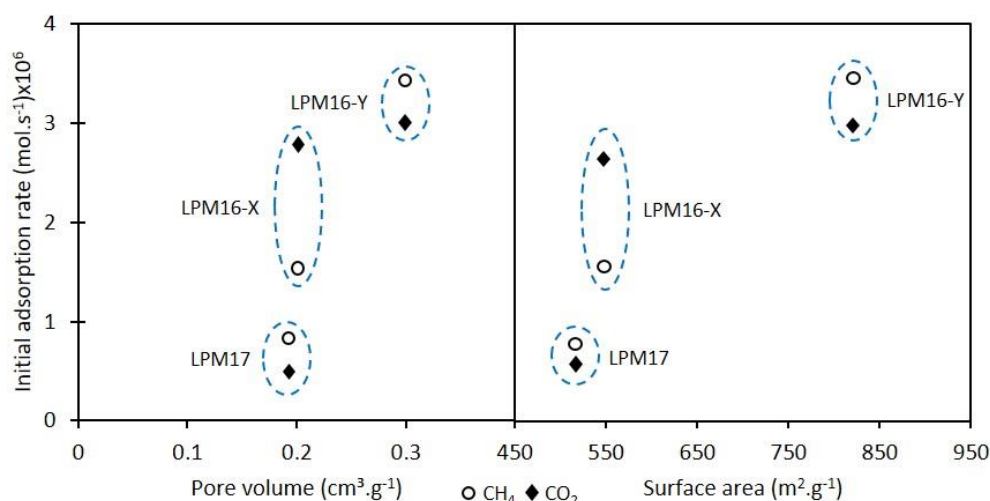
Since surface area and crystallinity do little to support this difference, the presence of preferential adsorption sites on the zeolitic surface is best applied because, in addition to the cationic sites, any defects may act as preferential sites for adsorption. In addition, the slower adsorption of CH<sub>4</sub> (tetrahedral) compared to CO<sub>2</sub> (linear) may be due to the molecular structural orientation [28].

Table 4. Initial adsorption rate, equilibrium time and adsorption capacity of CH<sub>4</sub> and CO<sub>2</sub> on the cage- and channel-type zeolites.

Materials	IAR* (mol.sec <sup>-1</sup> )x10 <sup>6</sup>		ET** (min)		AC*** (mmol.g <sup>-1</sup> )	
	CH <sub>4</sub>	CO <sub>2</sub>	CH <sub>4</sub>	CO <sub>2</sub>	CH <sub>4</sub>	CO <sub>2</sub>
LPM16-X	1.4	2.8	250	67	10.9	3.1
LPM16-Y	3.5	3.0	65	58	9.4	3.3
LPM17	0.9	0.4	10	13	2.1	0.7

\*IAR = Initial Adsorption Rate; \*\*ET = Equilibrium Time; \*\*\*AC = Adsorption Capacity.

Figure 10. The effects of pore volume and surface area on the initial adsorption rate (CH<sub>4</sub> and CO<sub>2</sub>) of the cage- and channel-type zeolites.



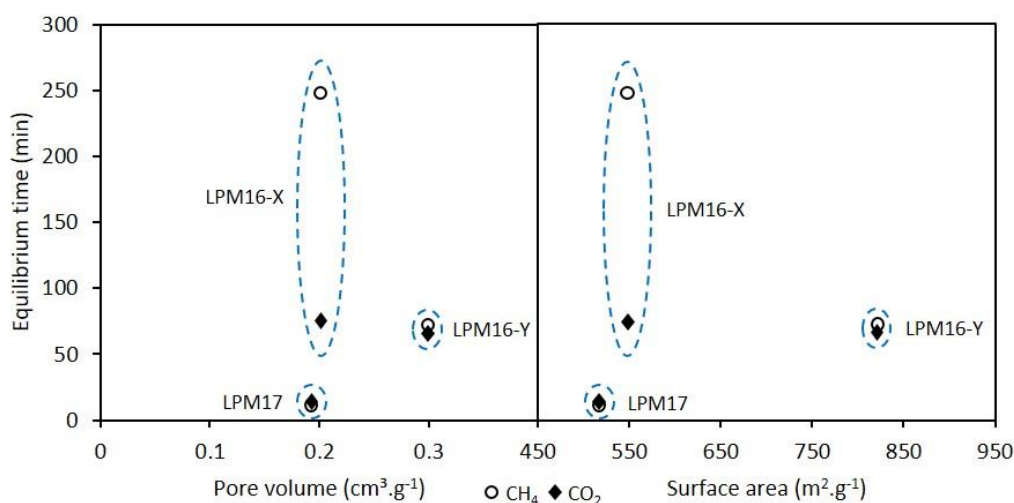
The results show that the high adsorption rate does not result in high adsorption capacity because there are factors that significantly affect the adsorption characteristics on the cage- and channel-type zeolites.

When the size of an adsorbate molecule is close to the size of the micropore, the penetration of the molecules into the micropore is restricted, and the rate of transport may have a significant effect on the overall adsorption rate. A high diffusion resistance and a long distance can affect the rate of gas adsorption.

In the case of apolar molecules (CH<sub>4</sub>), the surface area and pore volume may influence the initial zeolite adsorption rates. Generally, a higher surface area and volume of pores lead to a high adsorption rate. This is especially true for cage-type zeolites because the adsorbates can easily diffuse into the inside of the cage and adsorb on the surface of the zeolite [31].

According to the equilibrium time data, shown in Fig. 11, CO<sub>2</sub> adsorption took less time to reach equilibrium than CH<sub>4</sub> adsorption did, corroborating the fact that there are some interactions between sodium cations and CO<sub>2</sub> molecules. By adopting the faujasite structures as an example, a lower SAR indicates the presence of more sodium (Na) as a charge balancing cation [28].

Figure 11. The effects of pore volume and surface area on equilibrium time (CH<sub>4</sub> and CO<sub>2</sub>) of the cage- and channel-type zeolites.



The results showed that as the surface area and the volume of the pores increases, CO<sub>2</sub> takes longer to reach equilibrium. It is assumed that for larger surface area and higher pore volume, the adsorbates "jump" from one site to another before being adsorbed to the surface. However, opposite relationships are observed in that the time required to reach equilibrium increases as the surface area decreases [28].

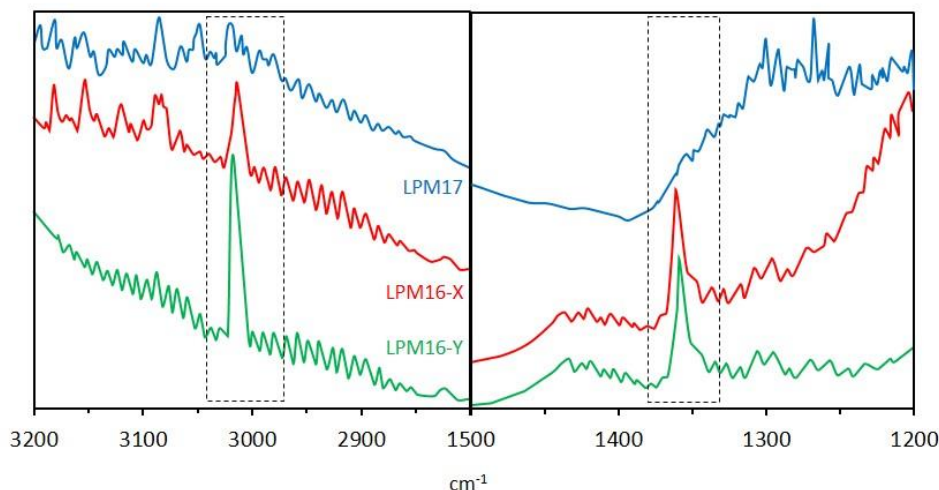
The adsorption process is affected by the presence of defects in the materials formed from the lithium extraction process. A higher pore size indicates the presence of defects in the zeolites from the processing, which results in a longer adsorption equilibrium time for zeolites with a larger average pore diameter [28].

In the case of channel-type zeolites, equilibrium was reached in less than 50 minutes. According to Roque-Malherbe (2018), diffusion and adsorption in zeolites depend very much on the pore network system and structure of the adsorbates. The large interactions between the molecules and the zeolite network also result in strongly adsorbed molecules within the channels [23].

Adsorbate-adsorbent interaction.

The FT-IR spectra of the adsorbed CH<sub>4</sub> molecules are shown in Fig. 12 in the regions between 3200-2800 cm<sup>-1</sup> and 1500-1200 cm<sup>-1</sup>, with an emphasis on the asymmetric band peaks (3040-2970 cm<sup>-1</sup>) and symmetrical peaks (1380-1335 cm<sup>-1</sup>).

Figure 12. FT-IR spectra of CH<sub>4</sub> adsorbed on the cage- and channel-type zeolites at 293 K and 1 bar.



In the gas adsorption process, the number of molecules attracted to a solid surface depends on the experimental conditions (temperature and pressure), the type of gas and the surface properties of the adsorbent. In macroporous materials, the adsorbate-adsorbate interaction is dominant.

However, in microporous materials, the adsorbent-adsorbate interaction is more important. The results of this interaction are indicated in the FT-IR spectra of the asymmetric and symmetric bands of the adsorbates due to the interactions between CH<sub>4</sub> and CO<sub>2</sub> molecules with zeolites through electrostatic forces C-Na, H-O, Si-C, O-Na, O-Si, and C-O [23].

According to Fig. 12, the peak at approximately 3020 cm<sup>-1</sup> is attributed to the asymmetric CH<sub>4</sub> adsorbed band as a result of the free rotation of adsorbed molecules around a single axis normal to the adsorbent surface [32].

In general, the spectra show that peak intensities for cage-type zeolites (LPM16-X and LPM16-Y) are higher and clearer than those for channel-type zeolites (LPM17). The presence of supercages within the faujasite structures (LPM16-X and LPM16-Y) allows greater freedom for the adsorbed molecules to rotate and experience a symmetric field of the zeolite pore walls [23].

The appearance of the symmetric band peak at approximately  $1365\text{ cm}^{-1}$  is attributed to the interaction of locally adsorbed molecules, with the induction of an electric field at the surface. Thus, it can be stated that there is a weak adsorbate-adsorbent interaction for channel-type zeolites. In contrast, the peaks of the asymmetric and symmetric bands are clearer in the FT-IR spectrum for cage-type zeolites because the  $\text{CH}_4$ -zeolite interaction is attributed to the confinement effect <sup>[27]</sup>.

## Conclusions

Two distinct types of zeolite structures obtained in the lithium extraction route were evaluated, offering numerous possibilities for specific applications. The cage-type zeolites (LPM16-X and LPM16-Y) adsorbed more than the channel-type zeolite (LPM17) because the cages provide space for the adsorbate within the structure, suggesting that the structural framework is an important factor in the selection of the type of adsorbent used, especially when high adsorption capacity is required.

The presence of structural defects (from the synthesis methodology) provided a greater number of active sites, as evidenced by the amount of  $\text{CH}_4$  and  $\text{CO}_2$  adsorbed. However, the presence of an amorphous phase was decisive in the low adsorption for LPM17.

In addition, thermodynamic data showed that the properties of the adsorbates (apolar molecule -  $\text{CH}_4$ , permanent quadrupole momentum -  $\text{CO}_2$ ) affected the adsorption characteristics. However, the fractional adsorption curve of  $\text{CH}_4$  showed the effect of the cage-type structure on adsorption, indicating typical properties of a potential adsorbent related to the structure type and pore diameter.

From the results of the kinetics studies, the adsorption of  $\text{CH}_4$  was strongly influenced by the limitation of the data on  $\text{CO}_2$  adsorption, suggesting that the quadrupole moment has a greater influence on the  $\text{CO}_2$  adsorption kinetics related to the structural framework of zeolites. Finally, the study of adsorbate-adsorbent interaction indicated a strong interaction between  $\text{CH}_4$  and the adsorption site (cation) of the zeolites evaluated, with higher intensity for LPM16-Y.

## Acknowledgments

The authors would like to thank CAPES (Coordenação de Aperfeiçoamento de Pessoal de Nível Superior) for the financial support, the CBL for the beta-spodumene samples and the Institute of Chemical Technology (ITQ/Valencia, Spain) for the characterization of the materials.

## References

- [1] SWAIN, B.; Recovery and recycling of lithium: A review. **Sep. Purif. Technol.**, 172 (2017), p. 388-403.
- [2] WIETELMANN, U., BAUER, R. J.; **Ullmann's encyclopedia of industrial chemistry** (p. 33-60), Weinheim: Wiley. 2008.
- [3] GRUBER, P. W., MEDINA, P. A., KEOLEIAN, G. A., KESLER, S. E., EVERSON, M. P., & WALLINGTON, T. J.; Global lithium availability: A constraint for electric vehicles?. **J. Ind. Ecol.**, 15.5 (2011), p. 760-775.
- [4] BIESEKI, L., MELO, V. R. M., V SOBRINHO, E., MELO, D. M. A., & PERGHER, S. B. C.; Extraction of lithium from  $\beta$ -spodumene sample. **Cerâmica**, 59.352 (2013), p. 557-562.
- [5] MESHARAM, P., PANDEY, B. D., & MANKHAND, T. R.; Extraction of lithium from primary and secondary sources by pre-treatment, leaching and separation: A comprehensive review. **Hydrometallurgy**, 150, p. 192-208.
- [6] KUANG, G., LIU, Y., LI, H., XING, S., LI, F., & GUO, H.; Extraction of lithium from  $\beta$ -spodumene using sodium sulfate solution. **Hydrometallurgy**, 177 (2018), p. 49-56.
- [7] OLIVEIRA, M. S. M., NASCIMENTO, R. M., PERGHER, S. B. C.; **Síntese do material zeolítico LPM-11 de tipologia MOR a partir do resíduo silicoaluminoso gerado na extração do lítio do espodumênio**. BR Patent No 10,2017,016712,7. 2017.
- [8] OLIVEIRA, M. S. M., NASCIMENTO, R. M., PERGHER, S. B. C.; **Síntese do material zeolítico LPM-12 de tipologia EDI a partir do resíduo silicoaluminoso gerado na extração do lítio do espodumênio**. BR Patent No 10,2017,016757,7. 2017.

- [9] BACSIK, Z., CHEUNG, O., VASILIEV, P., & HEDIN, N.; Selective separation of CO<sub>2</sub> and CH<sub>4</sub> for biogas upgrading on zeolite NaKA and SAPO-56. **Applied Energy**, 162 (2016), p. 613-621.
- [10] MARTÍN, N., PARIS, C., VENNESTRØM, P. N., THØGERSEN, J. R., MOLINER, M., & CORMA, A.; Cage-based small-pore catalysts for NH<sub>3</sub>-SCR prepared by combining bulky organic structure directing agents with modified zeolites as reagents. **Appl. Catal., B**, 217 (2017), p. 125-136.
- [11] MAGHSOUDI, H., & SOLTANIEH, M.; Simultaneous separation of H<sub>2</sub>S and CO<sub>2</sub> from CH<sub>4</sub> by a high silica CHA-type zeolite membrane. **J. Membr. Sci.**, 470 (2014), p. 159-165.
- [12] LI, H., HAAS-SANTO, K., SCHYGULLA, U., & DITTMAYER, R.; Inorganic microporous membranes for H<sub>2</sub> and CO<sub>2</sub> separation - Review of experimental and modeling progress. **Chem. Eng. Sci.**, 127 (2015), p. 401-417.
- [13] ILIĆ, B., & WETTSTEIN, S. G.; A review of adsorbate and temperature-induced zeolite framework flexibility. **Micropor. Mesopor. Mat.**, 239 (2017), p. 221-234.
- [14] SANTOS, L. L., NASCIMENTO, R. M., PERGHER, S. B. C.; **Processo para obtenção dos materiais LPM-15, LPM-16 e LPM-17, com topologias zeolíticas LTA, FAU e MOR, respectivamente, como subproduto da extração do lítio a partir do beta-espodumênio.** BR Patent No 10,2018,016312,4. 2018.
- [15] IYOKI, K., YAMAGUCHI, Y., ENDO, A., YONEZAWA, Y., UMEDA, T., YAMADA, H., YANABA, Y., YOSHIKAWA, T., OHARA, K., YOSHIDA, K., SASAKI, Y., OKUBO, T., & WAKIHARA, T.; Formation of a dense non-crystalline layer on the surface of zeolite Y crystals under high-temperature steaming conditions. **Micropor. Mesopor. Mat.**, 268 (2018), p. 77-83.
- [16] REGE, S. U., & YANG, R. T.; A novel FTIR method for studying mixed gas adsorption at low concentrations: H<sub>2</sub>O and CO<sub>2</sub> on NaX zeolite and  $\gamma$ -alumina. **Chem. Eng. Sci.**, 56.12 (2001), p. 3781-3796.
- [17] MINTOVA, S., & BARRIER, N.; **Verified synthesis of zeolitic materials** (3rd ed.), Elsevier. 2016.
- [18] BRECK, D. W.; **Zeolite Molecular Sieves**, New York: Wiley & Sons. 1974.

- [19] FLANIGEN, E. M., KHATAMI, H.; **Infrared structural studies of zeolite frameworks** (p. 201-299), Washington: American Chemical Society. 1971.
- [20] VAN DONK, S., JANSSEN, A. H., BITTER, J. H., & DE JONG, K. P.; Generation, characterization, and impact of mesopores in zeolite catalysts. **Catalysis Reviews**, 45.2 (2003), p. 297-319.
- [21] AWALA, H., GILSON, J. P., RETOUX, R., BOULLAY, P., GOUPIL, J. M., VALTCHEV, V., & MINTOVA, S.; Template-free nanosized faujasite-type zeolites. **Nature Materials**, 14.4 (2015), p. 447-451.
- [22] CAI, M., PALČIĆ, A., SUBRAMANIAN, V., MOLDOVAN, S., ERSEN, O., VALTCHEV, V., ORDOMSKY, V. V., & KHODAKOV, A. Y.; Direct dimethyl ether synthesis from syngas on copper–zeolite hybrid catalysts with a wide range of zeolite particle sizes. **J. Catalysis**, 338 (2016), p. 227-238.
- [23] ROQUE-MALHERBE, R. M.; **Adsorption and diffusion in nanoporous materials**, CRC press. 2018.
- [24] ZHANG, J., BURKE, N., ZHANG, S., LIU, K., & PERVUKHINA, M.; Thermodynamic analysis of molecular simulations of CO<sub>2</sub> and CH<sub>4</sub> adsorption in FAU zeolites. **Chem. Eng. Sci.**, 113 (2014), p. 54-61.
- [25] GARCÍA-PÉREZ, E., PARRA, J. B., ANIA, C. O., GARCÍA-SÁNCHEZ, A., VAN BATEN, J. M., KRISHNA, R., DUBBELDAM, D., & CALERO, S.; A computational study of CO<sub>2</sub>, N<sub>2</sub>, and CH<sub>4</sub> adsorption in zeolites. **Adsorption**, 13.5-6 (2007), p. 469-476.
- [26] RABIEE, H., ALSADAT, S. M., SOLTANIEH, M., MOUSAVI, S. A., & GHADIMI, A.; Gas permeation and sorption properties of poly (amide-12-b-ethyleneoxide)-(Pebax1074)/SAPO-34 mixed matrix membrane for CO<sub>2</sub>/CH<sub>4</sub> and CO<sub>2</sub>/N<sub>2</sub> separation. **J. Ind. Eng. Chem.**, 27 (2015), p. 223-239.
- [27] DEROUANE, E. G., & CHANG, C. D.; Confinement effects in the adsorption of simple bases by zeolites. **Micropor. Mesopor. Mat.**, 35 (2000), p. 425-433.
- [28] THANG, H. V., GRAJCIAR, L., NACHTIGALL, P., BLUDSKÝ, O., AREÁN, C. O., FRÝDOVÁ, E., & BULANEK, R.; Adsorption of CO<sub>2</sub> in FAU zeolites: Effect of zeolite composition. **Catalysis Today**, 227 (2014), p. 50-56.
- [29] ULLAH, R., SAAD, M. A. H. S., APARICIO, S., & ATILHAN, M.; Adsorption equilibrium studies of CO<sub>2</sub>, CH<sub>4</sub> and N<sub>2</sub> on various modified zeolites at high pressures up to 200 bars. **Micropor. Mesopor. Mat.**, 262 (2018), p. 49-58.

- [30] FANG, H., AWATI, R., BOULFELFEL, S., RAVIKOVITCH, P. I., & SHOLL, D. S.; First-Principles-Derived Force Fields for CH<sub>4</sub> Adsorption and Diffusion in Siliceous Zeolites. **J. Phys. Chem. C**. 2018. DOI: 10.1021/acs.jpcc.8b03267.
- [31] TAN, Y. H., DAVIS, J. A., FUJIKAWA, K., GANESH, N. V., DEMCHENKO, A. V., & STINE, K. J.; Surface area and pore size characteristics of nanoporous gold subjected to thermal, mechanical, or surface modification studied using gas adsorption isotherms, cyclic voltammetry, thermogravimetric analysis, and scanning electron microscopy. **J. Mat. Chem.**, 22.14 (2012), p. 6733-6745.
- [32] THOMMES, M., KANEKO, K., NEIMARK, A. V., OLIVIER, J. P., RODRIGUEZ-REINOSO, F., ROUQUEROL, J., & SING, K. S.; Physisorption of gases, with special reference to the evaluation of surface area and pore size distribution (IUPAC Technical Report). **J. Pure Appl. Chem.**, 87.9-10 (2015), p. 1051-1069.

## Chapter 8. Final considerations

---

The objectives of this thesis have been completed. It was possible to modify a process of extraction of lithium from beta-spodumene, directing to the formation of different zeolites with high purity instead of the formation of residue.

During the course of the thesis, structures, physical-chemical properties, and catalytic behavior were evaluated to identify the degree of stability, selectivity and activity of the zeolites obtained (A, X, Y, Mordenite, ZSM-5, and T). These materials were synthesized in two different lithium extraction routes, optimized from modifications in calcination, hydrothermal treatment, and precipitation, to obtain the corresponding salt,  $\text{Li}_2\text{CO}_3$ , as well as zeolite material as a by-product.

Throughout this process of study, we come to many partial conclusions that, although they were listed at the end of each chapter, are summarized in this section in order to provide an overview of the thesis held.

Summary of main conclusions reached:

1. In the first developed route, LPM-15, LPM-16 and LPM-17 zeolites of LTA, FAU and MOR topologies, respectively, were obtained as a by-product of the lithium extraction process from beta-spodumene in a cyclic route, environmentally friendly, free of organic solvents and calcination, developed from hydrothermal treatment between aqueous sodium hydroxide and sodium carbonate in solution with sodium aluminate (to obtain LPM-15) or aluminum hydroxide (LPM- 16) or aerosol silica (LPM-17), as well as ammonium ion bicarbonate for precipitation of the corresponding salt,  $\text{Li}_2\text{CO}_3$ , recovering up to 85% lithium from the supernatant.
2. In the mechanism described above, the extraction was strongly influenced by the reaction period, with the recovered  $\text{Li}_2\text{CO}_3$  content proportional to the reaction temperature (393 K) in the hydrothermal treatment stage and inversely to the molar ratio  $\text{Li}_2\text{O}:4\text{Na}_2\text{CO}_3$  for 120 min of reaction, and slightly proportional to the molar ratio  $\text{Li}_2\text{O}:4\text{Na}_2\text{CO}_3$ , after reducing the temperature (368 K), with a total duration of 360 min.

3. To obtain by-product with zeolite characteristics of FAU topology (LPM16-X and LPM16-Y), solubilization with  $\text{Al}(\text{OH})_3$  was performed at 363 K for 6 h, promoting recovery of 80% lithium. For MOR topological zeolite (LPM-17), the solubilization with silica aerosil was performed at 423 K for 48 hr in 70% lithium yield.
4. CEC of the LPM-15 zeolite suggests good characteristics for adsorption, is indicated for the treatment of effluents. The theoretical calculations of molecular modeling suggest a structural stabilization around the  $\text{Na}^+/\text{Al}^{3+}$  cation exchange, indicated for processes of water purification, catalytic cracking, and biofuel production, according to geometric data of "accessible pore volume" and "pore opening diameter".
5. Considering the adsorption activities between the zeolite structures obtained, the cage-like structure (LPM16-Y) showed to be a potential adsorbent of  $\text{CH}_4$  and  $\text{CO}_2$ .
6. In the second route, LPM-18 and LPM-19 zeolites of MFI and LTT topologies, respectively, were obtained as a by-product of the lithium extraction process from beta-spodumene, in a cyclic route, free of organic solvents, seeds and templates, developed from the leaching of beta-spodumene in acid solution, calcination with carbonate and sodium chloride, hydrothermal treatment with sodium hydroxide (to obtain LPM-18) and potassium hydroxide (LPM-19), bicarbonate with ammonium ion to precipitate the corresponding salt,  $\text{Li}_2\text{CO}_3$ , recovering up to 84% lithium from the supernatant.
7. In the mechanism described above, the extraction was strongly influenced by calcination parameters:  $T_{\text{max}} = 923 \text{ K}$ , thermal cycle = 120 min, rate  $5^\circ\text{C}\cdot\text{min}^{-1}$ . The molar ratio was  $\text{Li}_2\text{O}:3\text{Na}_2\text{CO}_3$ . The recovery of lithium could be justified by the experimental model of "nucleation and growth of crystals", based on the diffusion stages of the salts in the beta-spodumene structure and the chemoselective exchange between  $\text{Li}^+$  of  $\beta\text{-LiAlSi}_2\text{O}_6$  and  $\text{Na}^+$  of  $\text{Na}_2\text{CO}_3$  and  $\text{NaCl}$ , represented by the theoretical model " $\ln(1-X) = -b_1[\ln(1+b_2t) - b_2t/(1+b_2t)]$ ", used to describe beta-spodumene decomposition.
8. In order to evaluate the total acidity of the zeolites by thermosorption, LPM-18 was promising for application in refining processes and for catalytic support, after correlation between SAR and density/strength of its acid sites.

## Appendix A. Patent application

**Process number:** BR 10/2018/016312/4

**Nature of the patent:** 10 - Patente de Invenção (PI).

**Title of the invention or utility model:** PROCESSO PARA OBTENÇÃO DOS MATERIAIS LPM-15, LPM-16 E LPM-17, COM TOPOLOGIAS ZEOLÍTICAS LTA, FAU E MOR, RESPECTIVAMENTE, COMO SUBPRODUTO DA EXTRAÇÃO DO LÍTIO A PARTIR DO BETA-ESPODUMÊNIO.

**Abstract:** The lithium extracted from litiniferous pegmatitic deposits is associated with sulfates, magnesium and other elements as impurities, making the extraction procedure more expensive with the use of actinide based solvents and the use of lithium salts, as well as the formation of aluminosilicose residue. The viability of an extraction process in the production of lithium chemical compounds will depend mainly on the extracted lithium content and ease of recovery, besides the possibility of recovery of the residue as a by-product. The present invention relates to an environmentally friendly and organic solvent-free process for extracting lithium in the form of salt from beta-spodumene by solubilization and hydrothermal treatment with sodium salts and reduced water content, in addition to precipitation from ammonium ion bicarbonate salt, recovering approximately 85% lithium-rich liquor from the supernatant, with simultaneous inert zeolite materials as resistant and chemically stable by-products up to 973 K, known as LPM- 15, LPM-16 and LPM-17, of LTA (NaA), FAU-X (NaX) and MOR (Na-MOR) topologies, respectively, free of structural lithium and reduced content of undissolved quartz.

**Pages:** 30.

**Depositor, CPF/CNPJ:** Universidade Federal do Rio Grande do Norte, 24365710000183.

**Inventors:** Leonardo Leandro dos Santos.  
Rubens Maribondo do Nascimento.  
Sibele Berenice Castellã Pergher.

**Deposit:** August 09, 2018.

## Appendix B. Patent application

**Process number:** BR 10/2018/016339/6

**Nature of the patent:** 10 - Patente de Invenção (PI).

**Title of the invention or utility model:** PROCESSO PARA OBTENÇÃO DOS MATERIAIS LPM-18 E LPM-19, COM TOPOLOGIAS ZEOLÍTICAS MFI E LTT, RESPECTIVAMENTE, COMO SUBPRODUTO DA EXTRAÇÃO DO LÍTIO A PARTIR DO BETA-ESPODUMÊNIO.

**Abstract:** Lithium compounds obtained from litiniferous pegmatites are usually associated with magnesium, sulfates and other elements as impurities that make the extraction process more expensive with organic solvents and/or actinide based, resulting in an aluminosilicate-based residue. The viability of an extraction process for the production of lithium-based chemical compounds will mainly depend on the extracted lithium content and ease of recovery, as well as the possibility of transformation of the residue into a by-product of commercial interest. The present invention relates to an environmentally friendly, solvent-free, seedless and template process for the extraction of lithium in the form of salt from beta-spodumene by solubilization with neutral alkali metal salts and dissolution of lithium carbonate as a more soluble bicarbonate with ammonium ion bicarbonate salt to obtain liquor rich in approximately 84% of lithium from the supernatant with simultaneous formation of zeolite materials as by-products called LPM- 18 and LPM-19, of MFI and LTT topologies, respectively, resistant and chemically stable at temperatures up to 973 K, recovered with reduced content of undissolved quartz and Si/Al molar ratio between 5 and 200.

**Pages:** 28.

**Depositor, CPF/CNPJ:** Universidade Federal do Rio Grande do Norte, 24365710000183.

**Inventors:** Leonardo Leandro dos Santos.  
Rubens Maribondo do Nascimento.  
Sibele Berenice Castellã Pergher.

**Deposit:** August 09, 2018.